

**SYNTHESIS & CHARACTERIZATION OF MODIFIED  
MESOPOROUS  $\text{LiMn}_{2-x}\text{Co}_x\text{O}_4$  THIN FILMS AS WATER  
OXIDATION ELECTROCATALYSTS**

A THESIS SUBMITTED TO  
THE GRADUATE SCHOOL OF ENGINEERING AND SCIENCE  
OF BILKENT UNIVERSITY  
IN PARTIAL FULFILLMENT OF THE REQUIREMENTS FOR  
THE DEGREE OF  
MASTER OF SCIENCE  
IN  
CHEMISTRY

By

Irmak Karakaya

September, 2019

SYNTHESIS & CHARACTERIZATION OF MODIFIED MESOPOROUS  
LiMn<sub>2-x</sub>Co<sub>x</sub>O<sub>4</sub> THIN FILMS AS WATER OXIDATION ELECTROCATALYSTS

By Irmak Karakaya

September, 2019

We certify that we have read this thesis and that in our opinion it is fully adequate, in scope and in quality, as a thesis for the degree of Master of Science.

---

Ömer Dağ (Advisor)

---

Ayşen Yılmaz

---

Emren Nalbant Esentürk

---

Ferdi Karadaş

---

Burak Ülgüt

Approved for the Graduate School of Engineering and Science:

---

Ezhan Karaşan  
Director of the Graduate School

# ABSTRACT

## SYNTHESIS & CHARACTERIZATION OF MODIFIED MESOPOROUS $\text{LiMn}_{2-x}\text{Co}_x\text{O}_4$ THIN FILMS AS WATER OXIDATION ELECTROCATALYSTS

Irmak Karakaya

M.Sc. in Chemistry

Advisor : Ömer Dağ

September, 2019

The lithiated transition metal oxides (LMO) are important group of materials in energy applications, particularly as water oxidation electrocatalysts. The mesoporous  $\text{LiMn}_{2-x}\text{Co}_x\text{O}_4$  thin film has been synthesized by using molten-salt assisted self assembly (MASA) method with a high surface area. Homogenous ethanol solution of nitrate salts (lithium, manganese(II) and cobalt(II)) and surfactants (CTAB and P123) in the presence of a small amount of  $\text{HNO}_3$  is coated over a glass substrate by spin-coating to form lyotropic liquid crystal (LLC) mesophase that is calcined at elevated temperature to synthesize disordered mesoporous  $\text{LiMn}_{2-x}\text{Co}_x\text{O}_4$  thin film. The mesophases display diffraction line(s) at small angles, indicating an ordered structure. The cobalt amount (x) has been varied from 0 to 2, keeping the same mesoporous and crystal structures.

The films were characterized using XRD, SEM, EDX, TEM,  $\text{N}_2$  adsorption-desorption techniques. The XRD provided that the end products have a spinel structure with very similar unit cell parameters in all compositions. The surface areas of the films vary from 98 to 144  $\text{m}^2/\text{g}$  with increasing cobalt amount in the films. The SEM images showed that the thin films are uniform with a thickness of around 200-500 nm.

The LLC mesophases have been also coated over FTO glass to fabricate electrode for oxygen evolution reaction (OER) and also for electrochemical characterizations. The electrodes prepared from all composition performed as good

electrocatalysts, however the Tafel slope decreased from 124 to 66 mV dec<sup>-1</sup> going from LiMn<sub>2</sub>O<sub>4</sub> to LiMnCoO<sub>4</sub>. The overpotential also dropped from 491 mV to 294 mV at 1 mA cm<sup>-2</sup> in water oxidation reaction. The LiMn<sub>2</sub>O<sub>4</sub> is the worst electrocatalyst tested in this thesis. It has high Tafel slope, which is not desired and also not stable during electrochemical test. The stability improves with increasing cobalt in the films. The LiMnCoO<sub>4</sub> has been reported to be one of the most efficient and stable electrocatalyst even if it is used 120 mA cm<sup>-2</sup> current densities. Therefore, the electrode with this composition has been investigated in detail in an alkali media.

The mesoporous LiMn<sub>2</sub>O<sub>4</sub> thin film is modified by successive ionic layer adsorption and reaction (SILAR) method to improve its activity and stability. This electrode is dipped into a 1 M cobalt (II) solution, then washed several time to ensure a single layer of cobalt species on the surface, the modified electrode is calcined to produce cobalt rich LiMn<sub>2-x</sub>Co<sub>x</sub>O<sub>4</sub> surface. Eventhough, the amount of cobalt in the modified electrode is smaller than 1 %, the modification decreased the Tafel slope from 127 to 80 mV dec<sup>-1</sup>, but the electrode was unstable during water oxidation process in alkali media. A range of LiMn<sub>2-x</sub>Co<sub>x</sub>O<sub>4</sub> (x = 0 to 0.4) compounds were modified by the SILAR method and tested for OER. The mesoporous LiMn<sub>1.6</sub>Co<sub>0.4</sub>O<sub>4</sub> (20 % cobalt and 80 % manganese) was used as the substrate and the SILAR method was employed 5-times, the Tafel slope of this electrode decreased from 64 to 46 mV dec<sup>-1</sup> with an overpotential decrease from 304 to 265 mV at 1mA cm<sup>-2</sup> and 826 to 546 mV at 10 mA cm<sup>-2</sup> by modification and displayed a robust property in water oxidation process.

**Keywords:** Lithium manganese cobalt oxide, Mesoporous thin films, Molten-salt assisted self assembly, Water oxidation electrocatalysts, SILAR method

# ÖZET

## SU OKSİDASYON ELEKTRO-KATALİZÖRÜ MEZOPORLU MODİFİYE $\text{LiMn}_{2-x}\text{Co}_x\text{O}_4$ İNCE FİMLERİN SENTEZİ VE KARAKTERİZASYONU

Irmak Karakaya

Kimya, Yüksek Lisans

Tez Danışmanı : Ömer Dağ

Eylül, 2019

Lityum geçiş metal oksitlerinin (LMO), enerji uygulamalarında büyük bir önemi vardır ve bu malzemelerin, suyun oksidasyon elektro-katalizörü olarak kullanılması da bu uygulamalardan bir tanesidir. Yüksek yüzey alanlarına sahip, mezoporlu  $\text{LiMn}_{2-x}\text{Co}_x\text{O}_4$  ince filmler, eriyik tuz destekli kendiliğinden oluşma (EDKO) metoduyla sentezlenebilir ve malzemeler doğal olarak daha fazla aktif yüzey bulundurur. Lityum, mangan(II), kobalt (II) nitrat tuzları, yüzey aktif maddeler olan CTAB ve P123 ve ek olarak nitrik asit ve etil alkol bulunduran homojen çözeltiler, dönel kaplama yöntemiyle bir substrat üzerine kaplanır ve liyotropik sıvı kristal (LSK) faz elde edilir ve bu faz, düşük açılı X-ışını difraktometresi ile analiz edilebilir. Bu LSK faz, yüksek ısı ile oksitlenir ve mezoporlu  $\text{LiMn}_{2-x}\text{Co}_x\text{O}_4$  ince filmler sentezlenir. Kobalt x miktarı 0'dan 2'ye arttırılsa bile, malzemenin mezopor ve kristal yapısının korunduğu gözlemlenmiştir.

İnce filmler, XRD, SEM, EDX, TEM, Azot adsorpsiyon teknikleri ile incelenmiştir. XRD tekniği, farklı orandaki malzemelerin spinel yapı oluşturduğu ve birim hücre parametrelerinin benzer olduğunu göstermiştir.  $\text{LiMn}_{2-x}\text{Co}_x\text{O}_4$  içindeki kobalt miktarının artmasıyla, malzemenin yüzey alanı 98'den 144  $\text{m}^2 \text{g}^{-1}$ 'a yükselmiştir. Ayrıca SEM tekniği ile de film kalınlıklarının 200 ile 500 nm arasında değiştiği gözlemlenmiştir.

LSK faz yardımıyla elde edilen ince filmler, FTO camlarının üzerine de kaplanmış ve su oksidasyon elektro-katalizörü olarak, elektrokimyasal karakterizasyon deneylerinde kullanılmıştır. Tüm elektrotlar, verimli katalizörler olarak nitelendirilmiştir. Fakat malzeme,  $\text{LiMn}_2\text{O}_4$ 'dan  $\text{LiMnCoO}_4$  oranına götürülünce, Tafel eğrisi de 124'den  $66 \text{ mV dec}^{-1}$ 'e düşmüştür ve bu durum  $1 \text{ mA cm}^{-2}$  akımdaki  $491 \text{ mV}$ 'dan  $294 \text{ mV}$ 'a olan ek potansiyel düşüşü ile kanıtlanmıştır. Aynı zamanda  $\text{LiMnCoO}_4$  oranlı malzeme katalitik verimi ile ve  $120 \text{ mA cm}^{-2}$  akımda bile bozulmayan yapısıyla rapor edilmiştir.

Mezoporlu  $\text{LiMn}_2\text{O}_4$  ince film, ardışık iyonik katman adsorpsiyonu ve reaksiyonu (SILAR) yöntemi ile modifiye edilmiştir. Elektrot, 1M kobalt çözeltilisine batırma yöntemi ile yapılmış ve bunun aracılığıyla yüzeyi  $\text{LiMn}_{2-x}\text{Co}_x\text{O}_4$  kompozisyonu olan malzeme elde edilmiştir. Bu modifiye, Tafel eğrisi değerinin  $127$ 'den  $80 \text{ mV dec}^{-1}$ 'e inmesini sağlamış fakat elektrotların stabil olmadığı gözlenmiştir. 20% kobalt ve 80% mangan içeren  $\text{LiMn}_{2-x}\text{Co}_x\text{O}_4$ , SILAR yöntemi için substrat olarak kullanılmış ve modifiye 5 kereye kadar yapılmıştır. Tafel eğrisi değeri  $64$ 'ten  $46 \text{ mV dec}^{-1}$ 'e düşürülmüş ve ek potansiyel değerleri de  $1 \text{ mA cm}^{-2}$  akımda  $304$ 'ten  $265$ 'e,  $10 \text{ mA cm}^{-2}$ 'de  $826$ 'dan  $546 \text{ mV}$ 'a düşüşlerle ve elektrodun stabil yapısıyla gösterilmiştir.

**Anahtar sözcükler:** Lityum mangan kobalt oksit, Mezoporlu ince filmler, Eriyik tuz destekli kendiliğinden oluşma, Su oksidasyon elektro-katalizörleri, SILAR yöntemi

# Acknowledgement

I would like to thank my advisor Prof. Ömer Dağ for this project. His patience and sharing his broad perspective in science was excellent. I was always proud of being a member of his research group.

I want to thank to my mom and dad, Tenzile & Fehmi Karakaya for their limitless support in my whole life. I specially want to share my appreciation to my beloved brother, Kaan Karakaya for his excellent support and life energy given by him. I also thank to my dearest sister and cat, Mayıs for emotional support on me.

I would like to thank so much to the biggest part of my university life, my sister Işıl Uzunok for her assistance in all lectures and emotional helps in all matters during last 8 years. Her support was non-negligible for me. Also, I want to thank to Dağ Group members Assel Amirzhanova, Gülbahar Saat, Muammer Yaman, Fadime Balcı, Nesibe Akmanşen, Guvanch Gurbanduryev, Ezgi Yılmaz and department members Merve Yence, Selin Ezgi Dönmez, Kerem Emre Ercan and Elif Pınar Alsaç for their friendship and supports.

Additionally, I want to share my appreciations to my professors, Ferdi Karadaş, Burak Ülgüt, to share their knowledge and their helps.

I would like to thank to my dear friends Ezgi Yıldırım, Sinem Annakkaya for their friendship. I always felt their best wishes that were always with me.

I specially thank to Mete Batuhan Durukan for his emotional support and beneficial discussions about electrochemistry.

*“ When I look back*

*I see the landscapes  
That I have walked through  
But it is different*

*All the great trees are gone  
It seems there are  
Remnants of them*

*But it is the afterglow  
Inside of you*

*Of all those you met  
Who meant something in your life “*

*Olav Rex, 1977*

# Contents

Chapter 1 .....	1
Introduction.....	1
1.1    Mesoporous Materials .....	1
1.1.1    Synthesis of Mesoporous Metal Oxides by Hard Templating Method..	2
1.1.2    Synthesis of Mesoporous Metal Oxides by Soft Templating Method ...	3
1.1.3    Molten Salt Assisted Self Assembly (MASA).....	4
1.1.4    Lyotropic Liquid Crystalline Mesophases (LLC) .....	6
1.1.5    Successive Ionic Layer Adsorption and Reaction (SILAR) .....	8
1.1.6    Application Fields of Mesoporous Metal Oxides .....	9
1.2    Water Oxidation Electrocatalysts .....	11
1.2.1    Mesoporous Metal Oxides as Water Oxidation Electrocatalysts.....	11
1.2.2    Mesoporous Lithiated Metal Oxides as Water Oxidation Electrocatalysts. ....	14
1.3    Electrochemical Background of Water Oxidation Reaction Electrocatalysts.....	15
1.3.1    Cyclic Voltammetry .....	15
1.3.2    Surface Concentration of Active Redox Species .....	16
1.3.3    Capacitance .....	17
1.3.4    Tafel Equation and Tafel Slope.....	17
1.3.5    Origin of the Overpotential in Water Oxidation Reaction.....	18
Chapter 2 .....	20
Experimental Section.....	20
2.1    Synthesis of Mesoporous Materials .....	20
2.1.1    Preparation of Solutions of Salts and Surfactants .....	20
2.1.2. Preparation of Lyotropic Liquid Crystalline (LLC) Films .....	22

2.1.2	Synthesis of Mesoporous $\text{LiMn}_{2-x}\text{Co}_x\text{O}_4$ Films.....	23
2.1.3	Preparation of $\text{LiMn}_{2-x}\text{Co}_x\text{O}_4$ Working Electrodes on FTO Glasses....	24
2.1.4	Preparation of $\text{LiMn}_{2-x}\text{Co}_x\text{O}_4$ Working Electrodes on Graphite Substrate.....	25
2.1.5	Preparation of Modified Electrodes by Dipping into 1 M $\text{Co}^{+2}$ Solution.....	26
2.2	Instrumentation.....	27
2.2.1	X-ray Diffraction (XRD) Measurements .....	27
2.2.2	Attenuated Total Reflection Fourier-Transform Infrared (ATR-FTIR) Spectroscopy .....	27
2.2.3	$\text{N}_2$ (77.4 K) Adsorption-Desorption Isotherms .....	27
2.2.4	Scanned Electron Microscope (SEM) – Energy Dispersive X-ray Spectroscopy (EDX).....	28
2.2.5	X-ray Photoelectron Spectroscopy (XPS).....	28
2.3	Electrochemical Measurements and Analysis .....	28
2.3.1	Cyclic Voltammetry (CV).....	29
2.3.1.1	Data Analysis of Surface Concentration of Active Redox Species.....	29
2.3.1.2	Calculation of Capacitance of the Electrodes .....	31
2.3.2	Chronoamperometry (CA) .....	32
2.3.2.1	Tafel Slope Analysis .....	32
2.3.3	Chronopotentiometry (CP).....	33
2.3.3.1	Overpotential reporting by CP experiment.....	34
Chapter 3	.....	35
	Results & Discussion.....	35
3.1	Characterization of Liquid Crystalline Mesophases of Lithium, Two Transition Metal Salts (Mn(II) and Co(II)) and Two Surfactants System .....	35

3.1.1	Liquid Mesophase Formation and Characterization .....	35
3.1.2	Liquid Crystalline Mesophase Stability .....	37
3.2	Characterization of Mesoporous $\text{LiMn}_2\text{O}_4$ and $\text{LiMn}_{2-x}\text{Co}_x\text{O}_4$ Thin Films.....	38
3.2.1	Characterization of Mesoporous $\text{LiMn}_2\text{O}_4$ .....	38
3.2.2	Characterization of Mesoporous $\text{LiMn}_{2-x}\text{Co}_x\text{O}_4$ .....	41
3.3	Electrochemical Measurements of Mesoporous $\text{LiMn}_{2-x}\text{Co}_x\text{O}_4$ Thin Films as Water Oxidation Electrocatalysts.....	46
3.3.1	Electrochemical Characterization and Efficiency in Water Oxidation of $\text{LiMn}_{2-x}\text{Co}_x\text{O}_4$ Films.....	46
3.3.2	Advanced Electrochemical Measurements on $\text{LiMnCoO}_4$ Working Electrode .....	55
3.3.3	Coating $\text{LiMnCoO}_4$ on Graphite Substrate and OER Efficiency .....	57
3.4	Modification of Electrodes by Dipping into Cobalt Nitrate Solution & Formation of Active Thin Layer on Electrode Surface .....	60
3.4.1	Characterization of Modified Electrodes by Dipping into Cobalt Solution.....	60
3.4.2	Water Oxidation Efficiency and Stability of Modified $\text{LiMn}_2\text{O}_4$ Electrodes by Dipping into Cobalt Solution.....	66
3.5	Stability of $\text{LiMn}_{2-x}\text{Co}_x\text{O}_4$ Electrodes for Modification.....	69
3.5.1	$\text{LiMn}_2\text{O}_4$ (Mn100-Co0) WE by Increasing Annealing Temperature ...	69
3.5.2	$\text{LiMn}_2\text{O}_4$ WE by Adding 5% to 25% Cobalt(II) Salt in the Initial Preparation Solution .....	72
3.6	Modified Mn80-Co20 and Mn85-Co15 WEs and Efficiency in Water Oxidation.....	77
3.6.1	Modification of Mn80-Co20 with Dipping Process and Increase in OER Efficiency.....	77

3.6.2 Mn85-Mn15 with Dipping Process and Increasing Stability after OER.....	80
3.7 Summary .....	83
Chapter 4.....	84
Conclusion .....	84
Future Recommendations.....	86
Bibliography.....	89

# List of Figures

<b>Figure 1.1.</b> Schematic representation of hard templating method. ....	2
<b>Figure 1.2.</b> Schematic representation of soft templating method.....	3
<b>Figure 1.3.</b> Schematic representation of the MASA method. ....	5
<b>Figure 1.4.</b> Schematic representation of LLC by two surfactants and transition metal salts.....	8
<b>Figure 1.5.</b> Schematic representation of SILAR method .....	9
<b>Figure 1.6.</b> Typical cyclic voltammogram of a transition metal oxide working electrode. ....	15
<b>Figure 2.1.</b> Schematic representation of the preparation procedure of the salts-surfactants solutions. ....	21
<b>Figure 2.2.</b> Schematic representation of the preparation of the LLC mesophases by spin coating and drop-cast coating methods. ....	22
<b>Figure 2.3.</b> Synthesis of LMOs on microscope slides by drop-cast and spin coating methods. ....	23
<b>Figure 2.4. (a)</b> Schematic representation of the preparation of WEs over FTO substrates <b>(b)</b> Photos of the WEs with various percentages of manganese and cobalt (Mn%-Co%) in $\text{LiMn}_{2-x}\text{Co}_x\text{O}_4$ calcined at 300 °C for 1h. ....	25
<b>Figure 2.5.</b> Schematic representation and setup of dip-coating of graphite substrate. ....	25
<b>Figure 2.6.</b> Schematic representation of modification of electrodes by dipping into 1M $\text{Co}^{+2}$ solution.....	26
<b>Figure 2.7.</b> Electrochemical setup illustration for three electrode system. ....	29

<b>Figure 2.8. (a)</b> Determination the potential range of redox couple as between 0.35 V and 0.65V <b>(b)</b> Set of CV curves recorded by increasing scan rate from 2 mV s <sup>-1</sup> to 20 mV s <sup>-1</sup> with intervals of 2 mV s <sup>-1</sup> .....	30
<b>Figure 2.9. (a)</b> CV curves with a series of scan rates (2 to 20 mV s <sup>-1</sup> ) <b>(b)</b> Plot of current densities of peaks (maxima) vs scan rate to obtain the slope.....	30
<b>Figure 2.10.</b> CV curve in a potential range (between -0.05 and 0.45 V) of a redox couple with the scan rate of 20 mV s <sup>-1</sup> .....	31
<b>Figure 2.11.</b> Determination of OER starting and starting potential of CA experiment. ....	32
<b>Figure 2.12.</b> Plot of log <i>i</i> vs overpotential extracted by CA experiment and linear fitting.....	33
<b>Figure 3.1.</b> Small angle XRD patterns of LLCs of 20Li-40(Mn%-Co%)-1CTAB-1P123 with increasing cobalt ratio from top to bottom, prepared by spin coating at 2000 rpm for 10 s. ....	36
<b>Figure 3.2.</b> High angle XRD patterns of LLCs 20Li-40(Mn%-Co%)-1CTAB-1P123 <b>(a)</b> As prepared LLCs at 2000rpm for 10 s <b>(b)</b> Aged LLCs with various times <b>(*)</b> <i>Co(NO<sub>3</sub>)<sub>2</sub>(H<sub>2</sub>O)<sub>6</sub></i> .....	37
<b>Figure 3.3.</b> XRD patterns of mesoporous LiMn <sub>2</sub> O <sub>4</sub> (Mn100-Co0) by calcination at different temperatures 300 °C to 650 °C - <b>(*)</b> <i>Mn<sub>2</sub>O<sub>3</sub></i> .....	39
<b>Figure 3.4.</b> SEM images of LiMn <sub>2</sub> O <sub>4</sub> (Mn100-Co0)) calcined at <b>a)</b> 300°C 1h <b>b)</b> 400°C 1h (by annealing) <b>(c)</b> 500°C 1h (by annealing).....	40
<b>Figure 3.5.</b> XRD patterns of LiMn <sub>2-x</sub> Co <sub>x</sub> O <sub>4</sub> (Mn%-Co%) at 300°C for 1 hour 2000rpm 10s and PDF cards of LiMn <sub>2</sub> O <sub>4</sub> -00-054-0252 and LiCoO <sub>2</sub> -00-044-0145.....	41

**Figure 3.6.** SEM images of  $\text{LiMn}_{2-x}\text{Co}_x\text{O}_4$  at  $300^\circ\text{C}$  (a) Mn100-Co0 (b) Mn75-Co25 (c) Mn50-Co50 (d) Mn25-Co75 (e) Mn0-Co100 ..... 43

**Figure 3.7.** EDX spectra of  $\text{LiMn}_{2-x}\text{Co}_x\text{O}_4$  (Mn%-Co%) at  $300^\circ\text{C}$  for 1h..... 44

**Figure 3.8.** Cyclic voltammograms of  $\text{LiMn}_{2-x}\text{Co}_x\text{O}_4$  (Mn%-Co%) (calcined at  $300^\circ\text{C}$  for 1h) electrode with a scan rate of  $50\text{ mV s}^{-1}$  ..... 46

**Figure 3.9.** CVs of the electrodes with scan rates of 2 to  $20\text{ mV s}^{-1}$  in the range of Mn and Co ions redox potentials; the composition of the electrodes are (a)Mn100-Co0-(Mn) (b)Mn0-Co100-(Co) (c-1)Mn75-Co25-(Mn) (c-2)Mn75-Co25-(Co) (d-1) Mn50-Co50-(Mn) (d-2)Mn50-Co50-(Co) (e-1) Mn25-Co75-(Mn) (e-2)Mn25-Co75-(Co) ..... 48

**Figure 3.10.** Current densities of oxidation peaks of Mn and Co with changing scan rates (a)Mn100-Co0-(Mn) (b)Mn0-Co100-(Co) (c-1)Mn75-Co25-(Mn) (c-2)Mn75-Co25-(Co) (d-1) Mn50-Co50-(Mn) (d-2)Mn50-Co50-(Co) (e-1) Mn25-Co75-(Mn) (e-2)Mn25-Co75-(Co) ..... 49

**Figure 3.11.** Tafel plots and equations of  $\text{LiMn}_{2-x}\text{Co}_x\text{O}_4$  (Mn%-Co%). ..... 51

**Figure 3.12.** Chronopotentiometry results of the  $\text{LiMn}_{2-x}\text{Co}_x\text{O}_4$  (Mn%-Co%) electrode at current density  $1\text{ mA cm}^{-2}$  for 3 hours..... 53

**Figure 3.13.** Cyclic Voltammograms of  $\text{LiMn}_{2-x}\text{Co}_x\text{O}_4$  (Mn%-Co%) before (1<sup>st</sup> CV) after (CV after CP at  $1\text{ mA cm}^{-2}$ ) (a)Mn100-Co0 (b)Mn75-Co25 (c)Mn50-Co50 (d) Mn25-Co75 (e)Mn0-Co100..... 54

**Figure 3.14.** Chronopotentiometry results of  $\text{LiMnCoO}_4$  WE at  $1\text{ mA cm}^{-2}$  for 18hrs (black line) and at 10 to  $120\text{ mA cm}^{-2}$  for 30 mins at each (colored lines) potentials. .... 56

<b>Figure 3.15.</b> (a) Current density vs overpotential and linear fit (b) First CV and CV after CP at $120 \text{ mA cm}^{-2}$ of $\text{LiMnCoO}_4$ WE.....	57
<b>Figure 3.16.</b> Cyclic voltammograms of Mn50-Co50 on FTO and graphite substrates .....	58
<b>Figure 3.17.</b> Chronopotentiometry results at $10 \text{ mA cm}^{-2}$ to $60 \text{ mA cm}^{-2}$ with the increments of $10 \text{ mA cm}^{-2}$ for 30 mins (a) $\text{LiMnCoO}_4$ on FTO (b) $\text{LiMnCoO}_4$ on graphite.....	59
<b>Figure 3.18.</b> Schematic representation of dipping method in 1 M cobalt solution of $\text{LiMn}_2\text{O}_4$ substrates; (a) coating of thin layer of cobalt oxide (b) diffusion of cobalt to form $\text{LiMn}_{2-x}\text{Co}_x\text{O}_4$ on WE surface.....	60
<b>Figure 3.19.</b> XRD patterns of $\text{LiMn}_2\text{O}_4$ and $\text{LiMn}_2\text{O}_4$ modified by dipping into cobalt solution (a) $10\text{-}80^\circ$ (b) $30\text{-}50^\circ$ - (*) $\text{Mn}_3\text{O}_4$ .....	61
<b>Figure 3.20.</b> XPS Mn ( $2\text{P}_{3/2}$ ) spectra of Mn75-Co25, $\text{LiMn}_2\text{O}_4$ (Mn100-Co0) and modified WEs.....	62
<b>Figure 3.21.</b> XPS Mn ( $2\text{P}_{3/2}$ ) spectra of $\text{Mn}_3\text{O}_4$ , $\text{Mn}_2\text{O}_3$ , $\text{LiMn}_2\text{O}_4$ (Mn100-Co0) and modified with 5-times dipping.....	63
<b>Figure 3.22.</b> SEM images of $\text{LiMn}_2\text{O}_4$ modified electrodes by dipping method (a) $\text{LiMn}_2\text{O}_4$ without dipping (b) 1-time dipping (c) 3-times dipping (d) 5-times dipping (e) 7-times dipping.....	64
<b>Figure 3.23.</b> Atomic percentage of Mn and Co in the modified materials (a) EDX spectra of the dipped $\text{LiMn}_2\text{O}_4$ . (b) Table of manganese to cobalt ratio as atomic percentages. (c) Plot of Mn/Co ratio vs dipping times into 1 M $\text{Co}(\text{NO}_3)_2$ solution.	65
<b>Figure 3.24.</b> CV curves of $\text{LiMn}_2\text{O}_4$ and modified forms by dipping into 1 M $\text{Co}(\text{NO}_3)_2$ solution. ....	66

<b>Figure 3.25.</b> Tafel slope analysis of modified $\text{LiMn}_2\text{O}_4$ electrodes.....	67
<b>Figure 3.26.</b> Cyclic voltammograms of the modified $\text{LiMn}_2\text{O}_4$ WEs (a) 1 <sup>st</sup> CV curve (b) CV curves after CP at $1\text{ mA cm}^{-2}$ for 6 hrs. ....	68
<b>Figure 3.27.</b> CVs of $\text{LiMn}_2\text{O}_4$ electrodes, calcined at 300, 400 and 500 °C. ....	70
<b>Figure 3.28.</b> CVs of $\text{LiMn}_2\text{O}_4$ at different temperatures (a) 1 <sup>st</sup> curve, (b) CV after CP at $1\text{ mA cm}^{-2}$ , and (c) CV after CP $10\text{ mA cm}^{-2}$ .....	71
<b>Figure 3.29.</b> Thin films of Mn%-Co% on microscope slides .....	72
<b>Figure 3.30.</b> SEM images of Mn100-Co0, Mn90-Co10, Mn80-Co20.....	73
<b>Figure 3.31.</b> Cyclic Voltammograms of Mn%-Co%.....	73
<b>Figure 3.32.</b> CVs of Mn%-Co% WEs and modified WEs (a) 1 <sup>st</sup> CV curves, (b) CV curves after CP at $1\text{ mA cm}^{-2}$ for 12 hrs, and (c) CV curves after CP at $10\text{ mA cm}^{-2}$ for 6 hrs.....	75
<b>Figure 3.33.</b> CV curves of Mn80-Co20 WE and modified WEs. ....	77
<b>Figure 3.34.</b> CVs of Mn80-Co20 WEs and modified WEs (a) 1 <sup>st</sup> CV curves, (b) CV curves after CP at $1\text{ mA cm}^{-2}$ for 12 hrs, and (c) CV curves after CP at $10\text{ mA cm}^{-2}$ for 6 hrs.....	79
<b>Figure 3.35.</b> CVs of Mn85-Co15 WEs and modified WEs (a) 1 <sup>st</sup> CV curves, (b) CV curves after CP at $1\text{ mA cm}^{-2}$ for 12 hrs, and (c) CV curves after CP at $10\text{ mA cm}^{-2}$ for 6hrs.....	82
<b>Figure 4.1.</b> CV curves of modified $\text{LiMn}_2\text{O}_4$ WEs by modification with annealing at 300, 400 and 500 °C.....	86
<b>Figure 4.2.</b> CVs of modified Mn100-Co0 by annealing at 300, 400 and 500 °C (a) 1 <sup>st</sup> CV curves, (b) CV curves after CP at $1\text{ mA cm}^{-2}$ for 12 hrs.....	88

# List of Tables

<b>Table 2.1.</b> Mol ratios of chemicals in the solutions and notation of the solutions by mole percentages of Mn(II) and Co(II) salts.....	21
<b>Table 2.2.</b> Quantities of LiNO <sub>3</sub> , [Mn(H <sub>2</sub> O) <sub>4</sub> ](NO <sub>3</sub> ) <sub>2</sub> , [Co(H <sub>2</sub> O) <sub>6</sub> ](NO <sub>3</sub> ) <sub>2</sub> , CTAB, P123, HNO <sub>3</sub> , and ethanol, used in the solutions. ....	22
<b>Table 3.1.</b> Diffraction angles and d-spacing values of the LLC mesophases of as prepared 20Li-40(Mn%-Co%)-1CTAB-1P123 samples. ....	36
<b>Table 3.2.</b> N <sub>2</sub> adsorption-desorption data of LiMn <sub>2</sub> O <sub>4</sub> at different calcination temperatures. ....	39
<b>Table 3.3.</b> N <sub>2</sub> adsorption-desorption results of LiMn <sub>2-x</sub> Co <sub>x</sub> O <sub>4</sub> according to Mn%-Co% mole percentages at 300 °C. ....	42
<b>Table 3.4.</b> Quantity of Mn and Co (in percent) in the LiMn <sub>2-x</sub> Co <sub>x</sub> O <sub>4</sub> (Mn%-Co%) samples.....	45
<b>Table 3.5.</b> Surface concentration of Co and Mn ion species on electrodes of LiMn <sub>2-x</sub> Co <sub>x</sub> O <sub>4</sub> (Mn%-Co%).....	50
<b>Table 3.6.</b> Specific capacitance values of LiMn <sub>2-x</sub> Co <sub>x</sub> O <sub>4</sub> by CVs in redox potential ranges of manganese and cobalt species with a scan rate of 20 mV s <sup>-1</sup> . ....	51
<b>Table 3.7.</b> Tafel slopes, overpotential ( $\eta$ ) at 1 mA cm <sup>-2</sup> and 10 mA cm <sup>-2</sup> by calculation from the Tafel equations of the LiMn <sub>2-x</sub> Co <sub>x</sub> O <sub>4</sub> (Mn%-Co%) electrodes. ....	52
<b>Table 3.8.</b> Tafel slopes and overpotential at 1 mA cm <sup>-2</sup> for 6 hrs CP of the modified electrodes.....	68
<b>Table 3.9.</b> Tafel slopes and overpotential results at 1 and 10 mA cm <sup>-2</sup> of the LiMn <sub>2</sub> O <sub>4</sub> WE, calcined at 3 different temperatures. ....	70

<b>Table 3.10.</b> Tafel slopes and overpotential results of Mn%-Co% WEs at 1 and 10 mA cm <sup>-2</sup> .....	74
<b>Table 3.11.</b> Tafel Slopes and overpotential results of Mn80-Co20 and modified forms WEs at 1 mA cm <sup>-2</sup> and 10 mA cm <sup>-2</sup> .....	78
<b>Table 3.12.</b> Tafel slopes and overpotential results of Mn85-Co15 and modified WEs at 1 and 10 mA cm <sup>-2</sup> current densities.....	80
<b>Table 3.13.</b> General table of the mesoporous metal oxide and lithiated metal oxides with Tafel slope and overpotential values at 1 mA cm <sup>-2</sup> and 10 mA cm <sup>-2</sup> .....	83
<b>Table 4.1.</b> Tafel slopes and overpotential values at 1 mA cm <sup>-2</sup> of the modified LiMn <sub>2</sub> O <sub>4</sub> WEs by modification and annealing at 300, 400 and 500 °C. ....	87

# List of Abbreviations

LC	: Liquid Crystal
LLC	: Lyotropic Liquid Crystal
LMO	: Lithium Transition Metal Oxide
EISA	: Evaporation Induced Self Assembly
MASA	: Molten salt Assisted Self Assembly
SILAR	: Successive Ionic Layer Adsorption and Reaction
XRD	: X-ray Diffraction
POM	: Polarized Optical Microscopy
SEM	: Scanning Electron Microscopy
TEM	: Transmission Electron Microscopy
EDX	: Energy Dispersive X-ray Spectroscopy
XPS	: X-ray Photoelectron Spectroscopy
ATR-FTIR	: Attenuated Total Reflection Fourier-Transform Infrared
BET	: Brunauer, Emmett and Teller
JCPDS	: Joint Committee on Powder Diffraction Standards
IUPAC	: International Union of Pure and Applied Chemistry
PDF	: Powder Diffraction File
OER	: Oxygen Evolution Reaction
HER	: Hydrogen Evolution Reaction
WE	: Working Electrode
RE	: Reference Electrode
CE	: Counter Electrode
FTO	: Fluorine doped Tin Oxide
NHE	: Normal Hydrogen Electrode
CV	: Cyclic Voltammetry
CA	: Chronoamperometry
CP	: Chronopotentiometry
C <sub>s</sub>	: Specific Capacitance

# Chapter 1

## Introduction

### 1.1 Mesoporous Materials

Mesoporous materials have been investigated over thirty years due to high demand on new materials with surface area, accordingly more active sites, for energy applications (such as green energy, energy storage, batteries and catalysts).[1]–[3]

However, the early work goes back to 1970s. Chiola *et al.* firstly, obtained mesoporous silica materials by using Stöber method and the work was patented by U.S. Patent Office in 1970s. [4], [5]. Later, Kresge *et. al* reported the synthesis of first mesoporous silica through surfactant templating in 1992. Since then, mesoporous materials have been heavily investigated over the years. Mesoporous materials are defined as materials with pores that have sizes between 2 and 50 nm. By controlling the pore sizes in this region, many properties for absorption of various chemicals have been shown.[6], [7] Also, high surface areas of mesoporous materials induce significant efficiency increases in energy production, conversion and storage applications.[7]–[9]

Until 1990s, the mesoporous materials were synthesized with a broad non-uniform size distribution. Kresge *et al.* discovered the ordered mesoporous silica by liquid crystal templating mechanism and with the following studies, it has been shown that the pore size distribution of mesoporous materials could be controlled.[7], [10] Later, the mesoporous silica has been used as a template to form other mesoporous

materials (known as hard-templating) and also non-siliceous mesoporous materials were obtained by surfactant templating method (known as soft templating) without using of silica. [11]–[13]

By synthesis of materials using both hard and soft templating methods, many new materials have been synthesized as in own mesoporous forms. Also, synthesis as mesoporous metal oxides have been studied extensively due to their new/improved applications that require large surface area.[14]–[16]

### 1.1.1 Synthesis of Mesoporous Metal Oxides by Hard Templating Method

Hard templating methods is an efficient way to synthesize mesoporous metal oxides. Template is a material that has a rigid structure and porosity like silica and carbon etc.[17], [18] The precursor of a desired material is mixed with the hard template, in which the precursor of the target material fills the pores of the template. Calcination of the mixture produce a mesoporous material that is formed by mimicking the shape of the pores of the template. The last step of hard templating method involves aching of the hard template by washing with an acidic (HF) or basic solution to obtain the mesoporous material of the precursor. [18], [19] Schematic representation of synthesis by hard templating is shown in Figure 1.1.

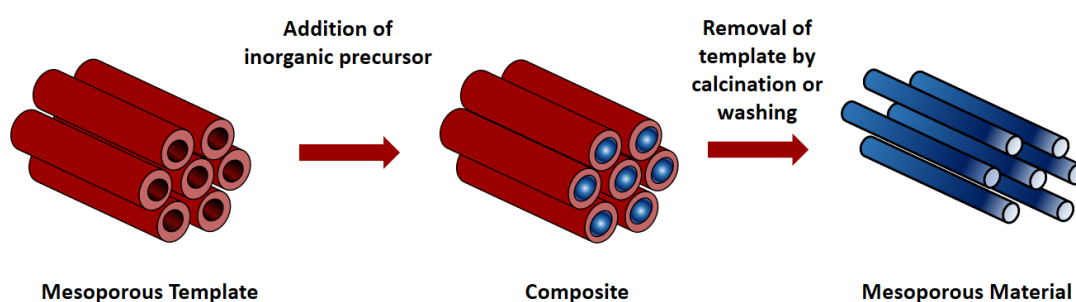


**Figure 1.1.** Schematic representation of hard templating method.

Ryoo *et al.* invented the hard template synthesis method and reported in 1999 by synthesis of a mesoporous carbon with pore size distribution average as 3 nm using cubic mesoporous silica as a template. [20] After the invention, it has been employed for the synthesis of mesoporous forms of different materials. Also, synthesis of

mesoporous transition metal oxides was firstly reported by using hard templating method in 2003. Zhu *et al.* synthesized mesoporous  $\text{Cr}_2\text{O}_4$  with a surface area of  $58 \text{ m}^2/\text{g}$  and an average pore size of 3.4 nm. [21]. Then, many mesoporous transition metal oxides and lithiated transition metal oxides were produced by hard templating method. [22], [23]

### 1.1.2 Synthesis of Mesoporous Metal Oxides by Soft Templating Method

The term ‘soft templating’ is used for surfactant templating in general, but we will focus on liquid crystalline templating method in this section. Many mesoporous materials, including the first examples, have been synthesized by soft template method. The difference between soft and hard templating methods is that the soft templating involves formation of a lyotropic liquid crystal (LLC) mesophase in the assembly process. The LLC phase is formed by the assembly of surfactant molecules. The surfactant molecules have both hydrophobic (tail) and hydrophilic (head) groups. They assemble into micelles (aggregate of 50-100 surfactant molecules) that can pack into LLC mesophase. The term ‘mesophase’ is used to describe LLC phase. The LLC phase consist of micelle surfactant domains that are surrounded by solvent species in the hydrophilic domains of the mesophase. Solvent molecules can also be a molten salt. Similar to the hard templating, the preformed LLC phase is calcined to produce mesoporous materials[24], [25] A schematic representation of LLC templating method is shown in Figure 1.2.

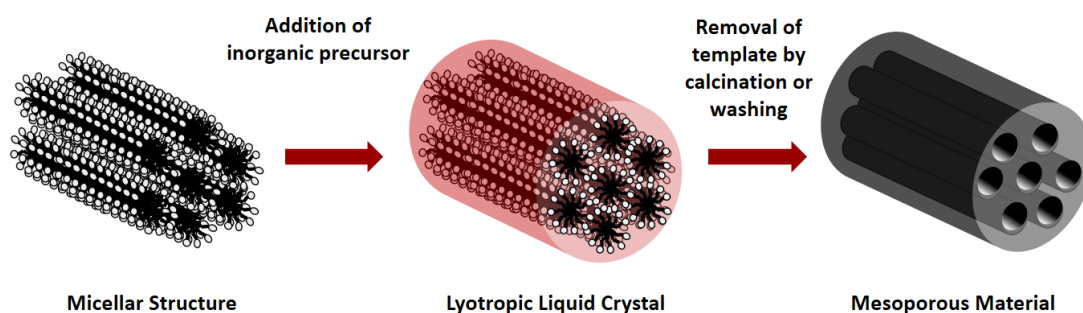


**Figure 1.2.** Schematic representation of soft templating method.

In 1992, Beck *et al.* synthesized mesoporous silica by using various types of quaternary ammonium surfactants as soft template and they investigated effect of the surfactant chain length on average pore sizes of mesoporous silica. [24] Then, mesoporous transition metal oxides, ZrO<sub>2</sub>, TiO<sub>2</sub>, Ta<sub>2</sub>O<sub>5</sub>, WO<sub>3</sub> were synthesized by using soft template with average pore size of 3 to 5 nm by Yang *et al.* late 1990s. [16] In 1999, Brinker *et al.* showed a soft template method by using CTAB as soft template and investigated the formation of an ordered structure with evaporation of solvent or increasing the concentration of surfactant. The method was named as evaporation-induced self-assembly (EISA).[26]

In the EISA process, the precursor of a desired material, surfactant, and solvent are mixed together and the solution are coated with various methods like spray, spin and dip-coating etc. With the evaporation of the volatile compounds, a semi solid mesostructure forms. The precursor species is located among the micellar structures and solidified by hydrolysis and condensation reactions. Note also that the precursors, in EISA method, are usually metal alkoxides that undergo hydrolysis and condensation reaction in aqueous media. In the last step of the process, the template is removed by some chemical or thermal treatments. [26], [27] There are some disadvantages of the EISA method, one is evaporation time is kept long, because fast removal of the template produces a disordered mesostructure or a material in bulk form. [28] Also because of fast solidification of the precursor species, a mesoporous material forms with thick crystalline pore-walls that decrease the surface area of the final product of the process. To form thinner walls, the precursor to surfactant concentration is critical and should be kept low.[29]–[31]

### **1.1.3 Molten Salt Assisted Self Assembly (MASA)**

The soft templating method for the synthesis mesoporous metal oxides have always been a challenge. Because, most transition metals do not have alkoxides and they are in the form of a salt. Most of these salts form stable solutions, instead of undergoing hydrolysis and condensation reactions and therefore difficult to assemble them as oxides or hydroxides in mesostructures. However, the lyotropic liquid crystalline mesophase of the salt and surfactant has a structure that can be converted into mesoporous structure by calcination of the mesophase.

In 2011 Dag *et al.*, discovered a new soft templating method to synthesize mesoporous materials with a high surface area. The method was named as molten-salt assisted self assembly (MASA) process.[32] In the MASA process, two surfactants are used. One of them is a non-ionic surfactant, such as pluronics or oligo (ethylene oxides). These surfactants form lyotropic liquid crystalline mesophases, in which salt species are in the molten phase. The other surfactant is a charged surfactant, such as cetyltrimethylammonium bromide (CTAB).

Usually, the charge surfactant and salt does not form a mesophase. Aim of using charged surfactant is to provide stabilization to the LLC phase at high salt concentrations. The charged head group of CTAB charge balance the salt-surfactant interface. Most significant distinctive property of the MASA method is that the salts are in molten phase among the micelle domains and acts as a non-volatile solvent in the LLC phase. The mixture of the mesophase can be dissolved in another solvent that gives flexibility to the MASA process. Because these solutions can be coated over a substrate and with the evaporation of the volatile solvent one can produce a thin film of the mesophase over the substrate. The mesophase are also flexible for more than one type of salts that two or more different type of salts can be used as a non-volatile solvent in these mesophase. This provides flexibility and also opportunities to produce mesoporous mixed metal oxide thin films. [32]–[34] A schematic representation of the MASA process is shown in Figure 1.3.

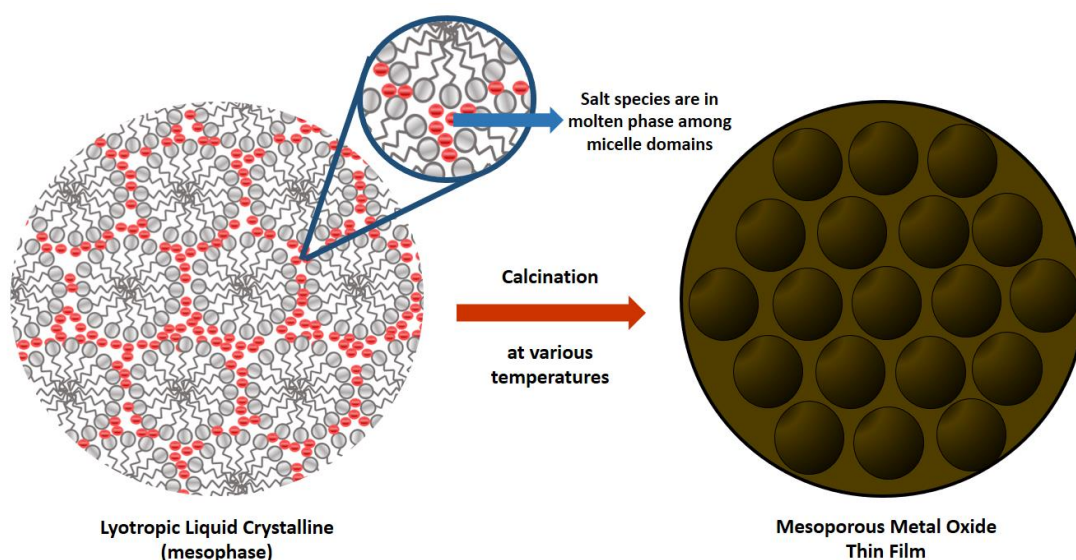


**Figure 1.3.** Schematic representation of the MASA method.

The MASA method was firstly reported by synthesis of mesoporous ZnO and CdO using silica. This study showed the pore size can be simply adjusted by the synthesis temperature. [32]. Later, some titanates, such as CdTiO<sub>3</sub>, Zn<sub>2</sub>TiO<sub>4</sub>, MnTiO<sub>3</sub>, CoTiO<sub>3</sub>, Li<sub>4</sub>Ti<sub>5</sub>O<sub>12</sub>, and lithiated transition metal oxides, such as LiCoO<sub>2</sub>, LiMn<sub>2</sub>O<sub>4</sub>, and mixed LiMn<sub>2-x</sub>Co<sub>x</sub>O<sub>4</sub> have been synthesized as mesoporous thin films with high surface area.[32]–[35]

Liquid crystalline mesophase has great importance in the synthesis of mesoporous materials as soft templates. The micelle domains in the mesophase burn out in the calcination step, leaving pores behind. The pore size can be controlled/adjusted by the size of the surfactants, as a result the size of the micelle domains, and the calcination temperature in the mesopore range (IUPAC definition of pore size in mesoporous materials is 2-50 nm) with a high surface. Therefore, LLC mesophase has a primary importance in the MASA process.

#### **1.1.4 Lyotropic Liquid Crystalline Mesophases (LLC)**

Liquid crystalline (LC) phase is an interface between solid and liquid phases. The LC phase has both ordered structure like solids and fluidity like liquids.[36] There are two types of LC phases. One of them is thermotropic LC and it forms in exact temperature range.[37] The other one is lyotropic liquid crystalline mesophase (LLC).

The LLC mesophases are formed by dissolving of a surfactant in a solvent at extrema high concentrations. The surfactant molecules are aligned depending on type of the solvent to form micellar structures. The micellar structured are formed by aggregation of the surfactant molecules by the hydrophobic attraction and hydrophilic repulsion forces. After evaporation of the excess solvent from the media the micelles assemble together to form denser LLC phase. The structure in the LLC phase could be cubic, hexagonal, lamellar structures. Also, if the LLC is cubic, because of being non-birefringent, they are not observed under polarized optical microscope (POM). The lamellar and hexagonal phase can be observed under POM, because they are birefringent (they have two distinctive refractive index). [38], [39] The LLCs have large unit cells because they are formed by micelles that are relatively larger building blocks compared to any atomic or molecular crystals, therefore they have large d-spacing values and diffract at small angles. To determine their structure, small angle

XRD technique is used and the diffraction data is evaluated using Bragg's law, see Equation 1.1

$$n\lambda = 2d \sin \theta \quad (\text{Equation 1.1})$$

Where  $\theta$  is half of the measured angle ( $^\circ$ ),  $d$  is  $d$ -spacing ( $\text{\AA}$ ),  $\lambda$  is the X-ray wavelength ( $1.5405 \text{\AA}$ ) and  $n$  is an integer, 1.

In early 2000s, Paschalis *et al.*, investigated LLC mesophases of various copolymers and reported all crystal structures like cubic, hexagonal etc. of LLC mesophase. [40], [41]. In 2002, same group reported the temperature dependent behaviors of these LLC mesophases. [42] In 2001, Dag *et al.* discovered a new LLC mesophase, formed by non-ionic surfactant using transition metal complex salts, such as  $[\text{Cd}(\text{H}_2\text{O})_4](\text{NO}_3)_2$ ,  $[\text{Zn}(\text{H}_2\text{O})_6](\text{NO}_3)_2$ ,  $[\text{Ni}(\text{H}_2\text{O})_6](\text{NO}_3)_2$ ,  $[\text{Co}(\text{H}_2\text{O})_6](\text{NO}_3)_2$  and  $[\text{Co}(\text{H}_2\text{O})_6]\text{Cl}_2$ . They have showed the structural behaviors of the new phases by changing salt to surfactant ratio and temperature and also reported cubic and hexagonal LLC mesophases.[39] In 2004, they investigated the effect of anions of the transition metal salts on the structure of the LLC mesophases. Later, they also investigated the LLC mesophase using different types of non-ionic surfactants.[39], [43], [44] In 2008, the role of adding a charged surfactant to the new LLC was demonstrated that addition of a charged surfactant to system improved LLC stability at high salt concentrations.[45] In 2012, they introduced lithium salts in place of transition metal salt also form LLC phases with non-ionic surfactant. They also showed incooperation of the lithium and transition metal salts together further improved the solubility of salt species in the LLC. [46] Figure 1.4 shows a schematic representation of LLC formation by using two surfactants and transition metal salts. All these investigations established a strong background for the fabrication of the  $\text{LiMn}_{2-x}\text{Co}_x\text{O}_4$  thin film electrodes that are investigated in this thesis.

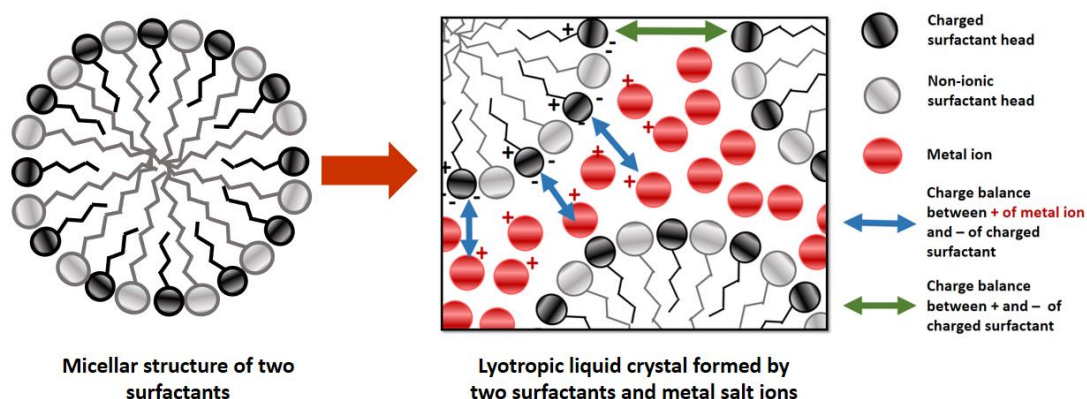


**Figure 1.4.** Schematic representation of LLC by two surfactants and transition metal salts.

### 1.1.5 Successive Ionic Layer Adsorption and Reaction (SILAR)

In the early 1980, Nicolau and François found a method that is used for thin film synthesis utilized by adsorbed ions and solid solution interface reaction. They named the technique as successive ionic layer adsorption and reaction (SILAR). The process was patented by U.S. Patent Office.[47] In SILAR method, process includes the immersing of a substrate into ionic solution. Cations are adsorbed by the surface of substrate. Then, the substrate is rinsed with water and process is followed by immersing the substrate into a solution that includes desired anion. So cations and anions react at interface. After reaction, substrate is washed and clean thin film is synthesized. To control the thickness of the film, method is repeated and multilayer of the compound could be obtained.[47], [48] In 1985, Nicolau used the method to synthesize ZnS and CdS, by dipping CdS slide into CdSO<sub>4</sub> solution. Then, Cd<sup>+2</sup> are adsorbed after immersion and after washing, the process was followed by immersion of substrate into Na<sub>2</sub>S solution.[47]. In 1990, Zn<sub>1-x</sub>Cd<sub>x</sub>S thin film deposition was worked.[49]. Nair *et al.* synthesize ZnO thin film by SILAR method. A glass substrate was immersed into zinc ammine solution and rinsing step was done by hot water (96°). So, zinc cations were oxidized by this thermal treatment to form ZnO.[50] In 2004, porous film of ZnO was obtained by modified SILAR method. [51] After invention of the technique, many transition metals like Zn, Cd, Cu, Sn and Ni etc. were synthesized as their sulphide, selenide and oxide forms and their optical properties were investigated.[52]–[55] In Figure 1.5, SILAR method is shown.

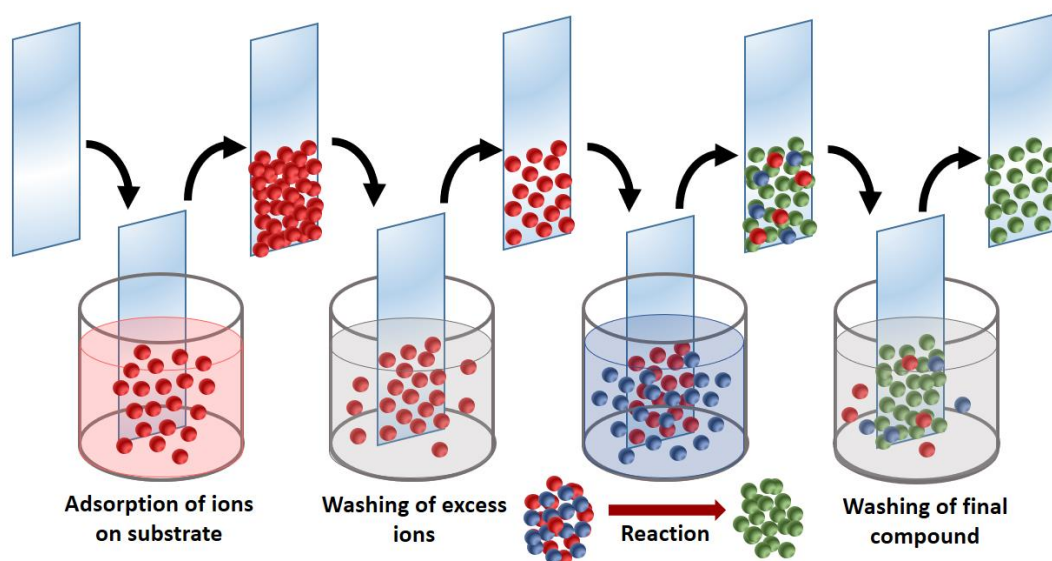


**Figure 1.5.** Schematic representation of SILAR method

### 1.1.6 Application Fields of Mesoporous Metal Oxides

The mesoporous metal oxides were synthesized successfully using both hard and soft templating methods. Having high surface area and reasonable pore sizes of mesoporous materials, provides them significant roles in many applications like, energy conversion and storage, chemical reactions and adsorption etc.[56]

For energy storage and conversion, mesoporous metal oxides have been in the applications, like solar cells, lithium ion batteries, and supercapacitors. For examples, O'Regan and Gratzel have used mesoporous  $\text{TiO}_2$  as a photo anode on a conductive glass in a dye synthesized solar cell (DSSC) in 1991 with decent cell performance. [57] Then, mesoporous  $\text{CeO}_2$  and  $\text{SnO}_2$  were shown with increasing quantum yield in DSSC. [56], [58]

Also, mesoporous metal oxides have been used in lithium ion batteries as both anode and cathode electrodes. The reasons of using them as electrode materials in the batteries is firstly, small particles making pore-walls that provide good conductivity and efficient transportation of electrons. Secondly, thin crystalline walls of mesoporous materials enhance the  $\text{Li}^+$  ion diffusion in the pore-walls. [56] As cathode materials, especially  $\text{LiCoO}_2$ ,  $\text{LiMn}_2\text{O}_4$ , and many transition metal oxides have been studied as lithiated metal oxides.[23], [59], [60]. As anode electrodes,  $\text{Co}_3\text{O}_4$ ,  $\text{NiO}$ ,  $\text{MoO}_2$ , and  $\text{TiO}_2$  etc. have been investigated in lithium ion batteries. [61], [62] In 2008,

Bruce *et al.* showed difference between bulk and mesoporous of spinel- $\text{Li}_{1.12}\text{Mn}_{1.88}\text{O}_4$  in terms of efficiencies in a lithium ion battery. Study reported that mesoporous form of the material has 50% higher efficiency than that of the bulk form in terms of storing  $\text{Li}^+$  ion in charge-discharge experiments.[63]

The mesoporous materials have generally been investigated as redox supercapacitors, named as pseudocapacitors. High current density could be obtained from the pseudocapacitors but higher energy is not required for charge-discharge process, because there is no intercalation of an ion in the process. Fast charging could be done compared to batteries.[56] In 2001, Antonelli *et al.* reported the electrochemical behaviors of some transition metal oxides. They showed that in  $\text{TiO}_2$ ,  $\text{Ti}^{+2/+3}$  redox couple is fully reversible and the material could be used as a pseudocapacitor.[64] In 2003, Owen *et al.* introduced a synthesis method for a supercapacitor of  $\text{Ni}/\text{Ni}(\text{OH})_2$  by electroplating mesoporous Ni surface.[65]

Mesoporous metal oxides are also used as catalyst, such as in photocatalysis or redox catalysis to split a chemical compound into sub-molecular species.[56] Photoelectrolysis of water has been studied for many years to produce hydrogen and oxygen. For this purpose,  $\text{TiO}_2$ ,  $\text{WO}_3$ , and  $\text{Ta}_2\text{O}_5$  etc. have been used as bulk semiconductors. Domen *et al.* synthesized a mesoporous nanocrystalline  $\text{Ta}_2\text{O}_5$  as a water splitting photocatalyst under UV light. First reports showed low efficiency for hydrogen evolution ( $50 \mu\text{mol}/\text{h}$ ) and no oxygen evolution. Then, a small weight percentage of NiO was added to the catalyst that showed an increased both hydrogen and oxygen gas evolutions. The very satisfying photocatalytic performance was obtained for hydrogen ( $3360 \mu\text{mol h}^{-1}$ ) and oxygen evolution ( $1630 \mu\text{mol h}^{-1}$ ) by using little amount of NiO on Ta oxide as co-catalyst.[66], [67]

Mesoporous metal oxides are used as redox electrocatalysts to oxidize or reduce many chemical compounds. [56] One of the most important materials to oxidize is carbon monoxide (CO) and oxidation of CO has an important mission for cleaning air. Catalysts like mesoporous manganese oxides,  $\text{Fe}_2\text{O}_3$ , NiO, and some mixed transition metal oxides were studied in the field of CO oxidation.[68] Schüth *et al.* synthesized mesoporous  $\text{Co}_3\text{O}_4$  and playing with thermal parameters, they controlled the size of the pores and surface area. By the controlling number of active

sites on surface, they showed a trend between surface area and CO oxidation efficiency. Higher efficiency was reported as  $0.8 \text{ mmol g}^{-1} \text{ h}^{-1}$ . [69]

The mesoporous metal oxides are important in energy storage and conversion, such as supercapacitors or electrodes for batteries. Also, they could be used as efficient photocatalysts or efficient electrocatalysts. In electrochemistry, they can be used as water oxidation electrocatalysts, because  $\text{H}_2$  is an important energy source. Evolution of hydrogen or water reduction is more efficient than water oxidation electrochemically. To have an efficient water splitting reaction, the  $\text{H}_2$  evolution should not be limited by the water oxidation process. So, for an efficient water splitting, the water oxidation electrocatalysts have significant roles in energy production.

## 1.2 Water Oxidation Electrocatalysts

The clean energy demand is increasing day by day, because of reduced fossil fuel resources as well as its environmental impacts. Hydrogen is one of a clean energy source and it could be extracted by hydrolysis of water. The hydrogen required for energy could be obtained by using proper electrocatalysts like metal oxides.[70] However, this process requires two electrodes, where both cathodic (water reduction or  $\text{H}_2$  evolution reaction (HER)) and anodic (oxygen evolution reaction (OER) or water oxidation reaction) occurs. In previous studies, the  $\text{O}_2$  evolution catalysts side of water splitting was shown to be kinetically limiting, compared to  $\text{H}_2$  evolution, because OER requires multistep electron transfer (4 electrons) besides 2 electron process of HER. So, between these two half reaction, the OER has the limitations for hydrogen production. [71], [72]

### 1.2.1 Mesoporous Metal Oxides as Water Oxidation Electrocatalysts

Metal oxides were generally used for the OER in alkaline media because of lower overpotential values for higher current densities. The most efficient materials, used as OER electrocatalysts are  $\text{RuO}_2$  and  $\text{IrO}_2$ . [70]

In 1977, Iwakura *et al.* reported the catalytic efficiency of  $\text{RuO}_2$  in bulk form with a Tafel slope of  $40 \text{ mV dec}^{-1}$ . [73], [74] In the end of 1970s, Lodi and Gallizioli showed the change in Tafel slopes by playing morphology of  $\text{RuO}_2$  as single crystal

and film forms by thermal methods. [75]–[77] Also, same research group showed that increase in compactness in films causes higher Tafel slopes so lower OER efficiencies and they created defects on surface of electrodes to disturb compactness of the materials. By doing this, the Tafel slopes was reported as low as 30 mV dec<sup>-1</sup> to 40 mV dec<sup>-1</sup>. [75] Also, IrO<sub>2</sub> was investigated in terms of efficiency in OER and found to be more stable in alkaline media compared to RuO<sub>2</sub>. [78] Typical IrO<sub>2</sub> electrodes, prepared by the same method of RuO<sub>2</sub>, had similar Tafel slopes. [79], [80] Also, both pure oxides of ruthenium and iridium had overpotentials of around 300 mV at 10 mA and even lower overpotentials by their modified forms by mixing, doping etc. have been reported. [81] Also, mesoporous RuO<sub>2</sub> and IrO<sub>2</sub> electrocatalysts were synthesized. The overpotential values were decreased down to around 250 mV [82], [83]

IrO<sub>2</sub> and RuO<sub>2</sub> are highly active materials for OER. However, production of these two materials in large scales is problem because they are two of scarcest and noble elements on earth. [70], [84] Because of low abundance of these noble metals, studies have been focused on more abundant transition metal oxides as OER catalysts and their catalytic efficiencies are compared with the noble metal oxides. In 1972, Fujishima *et al.* used TiO<sub>2</sub> for OER reaction for the first time and observed the evolution of O<sub>2</sub> bubbles on the electrode surface. [85] With this invention, researchers around the globe started working on the first row transition metal oxides, such as oxides of manganese, iron, cobalt, and nickel etc. as catalysts for water splitting. [70] In 1970s, Harriman and Morita synthesized MnO<sub>2</sub> and Mn<sub>2</sub>O<sub>3</sub> and they reported that the catalysts were functioned in OER. [86], [87] Frei *et al.* synthesized mesoporous manganese oxide by using silica as a template and by thermal treatment from low to higher temperature, the manganese oxide type changed from Mn<sub>3</sub>O<sub>4</sub> to Mn<sub>2</sub>O<sub>3</sub> and then, to MnO<sub>2</sub>. At each temperature, they reported O<sub>2</sub> yield resulted by reaction and at 600 °C, nanoclusters of Mn<sub>2</sub>O<sub>3</sub> gave the highest yield compared to micron sized MnO<sub>2</sub> and Mn<sub>2</sub>O<sub>3</sub>. [88] Gorlin *et al.* showed efficiency of a nano manganese oxide synthesized by electrodeposition and reported overpotential value at 10 mA as 1.0 V vs NHE and compared it with noble metals. The Pt, Ir and Ru in their metallic forms have overpotentials of 1.25V, 0.84V, 0.85V, respectively, vs NHE. [89]

Also, studies have been done on Fe<sub>2</sub>O<sub>3</sub> because of low cost and abundance. [70] Studies have shown that the  $\alpha$ -Fe<sub>2</sub>O<sub>3</sub> electrodes are sensitive to light and has

photocatalytic activity in OER.[90] Turner *et al.* worked on  $\alpha$ -Fe<sub>2</sub>O<sub>3</sub> to convert solar energy into hydrogen and oxygen but the efficiency is reported to be very low, 0.05%. In 2013, Rodney *et al.* synthesized an amorphous  $\alpha$ -Fe<sub>2</sub>O<sub>3</sub> by annealing it at 150 °C and report a Tafel slope of as low as 40 mV dec<sup>-1</sup>. However, the problem is that the overpotential value is high, 320 mV at 0.5 mA cm<sup>-2</sup>. [91] Cesar *et al.* showed that nanocrystalline  $\alpha$ -Fe<sub>2</sub>O<sub>3</sub> doped with silicon gave 2.1% conversion efficiency.[92]

Cobalt oxides types, Co<sub>3</sub>O<sub>4</sub>, Co<sub>2</sub>O<sub>3</sub> and CoO<sub>2</sub> have been studied as OER many times. The reason of focusing on mostly cobalt oxides in OER is being very stable in alkaline mediums.[70] In 1981, Iwakura *et al.* showed that the Co<sub>3</sub>O<sub>4</sub> film has catalytic efficiency in OER by oxygen evolution.[93] 2 years later, Tseung *et al.* demonstrated the effect of lithium doping in Co<sub>3</sub>O<sub>4</sub> by changing the amount of lithium in terms of oxygen yield because oxygen evolution voltage was decreased by increasing the doping amount of lithium. [94] In 1990, Singh *et al.* reported a Tafel slope of bulk Co<sub>3</sub>O<sub>4</sub> as 60 mV dec<sup>-1</sup> in 1 M KOH solution and also they showed the effect of pH of the media by changing molarity of KOH electrolyte and reported that increasing pH causes a decrease in the overpotential.[95] Da Silva *et al.* mixed RuO<sub>2</sub> and Co<sub>3</sub>O<sub>4</sub> and worked in an acidic 1 M electrolyte and they reported that the mixed material, which contain 30% to 80% RuO<sub>2</sub> as mole ratio, showed better Tafel slopes around 30 mV dec<sup>-1</sup> compared to pure Co<sub>3</sub>O<sub>4</sub> and RuO<sub>2</sub>, having Tafel slopes of 60 mV dec<sup>-1</sup> and 40 mV dec<sup>-1</sup>, respectively.[96] In 2013, Tuysuz *et al.* demonstrated the performance change between bulk and mesoporous Co<sub>3</sub>O<sub>4</sub>, having a surface area of 113 m<sup>2</sup> g<sup>-1</sup>. They reported current density value at an exact potential value of 735 mV and current density of bulk and mesoporous materials were 2.8 and 13.16 mA cm<sup>-1</sup>, respectively. [97]

In 1966, Bode *et al.* showed the catalytic behavior of NiO in OER. [98] In 1980s, by iron doping, NiO efficiency has been increased. [99], [100] Zhao *et al.* showed a Tafel slope of bulk NiO in 1M KOH is around 200 mV dec<sup>-1</sup> and they also worked on nanosheets of NiO by loading 1 and 2 sheets of material. The results of the Tafel slope didn't change. Then, they mixed NiO and TiO<sub>2</sub> and synthesized monosheet of mixed material and they could obtain a 52 mV dec<sup>-1</sup> Tafel slope.[101] Yu *et al.* coated carbon nanotubes with NiO and compared the results of NiO coated indium doped tin oxide (ITO). Use of a carbon nanotube as a substrate is to increase active

sites of NiO by multi-walled form of nanotubes. So, they reported that the bulk NiO on ITO gave lower current density than NiO on carbon nanotube at 1.1 V and they proved the electrode substrate effect on electrochemical performances. [102] Liu *et al.* synthesized mesoporous NiO and NiFe<sub>2</sub>O<sub>4</sub> and reported their Tafel slopes and overpotentials at 10 mA as 58 mV dec<sup>-1</sup> and 364 mV and 44 mV dec<sup>-1</sup> and 342 mV, respectively, and explained the results by decrease in charge transfer resistance in the case of adding iron into NiO.[103]

### 1.2.2 Mesoporous Lithiated Metal Oxides as Water Oxidation Electrocatalysts

Lithiated transition metal oxides have been used as electrode materials for the lithium ion batteries. [23], [63] These oxide types could be used as water oxidation catalysts, because in spinel structure of LiM<sub>2</sub>O<sub>4</sub>, where M is a transition metal, metal and oxygen bond is longer or weaker compared to non-cubic structures and it provides smaller energy barrier for the water oxidation reaction.[104]

Wang *et al.* synthesized bulk and nanosheets of LiCoO<sub>2</sub> and reported Tafel slopes of both form of the material as 156 mV dec<sup>-1</sup> and 88 mV dec<sup>-1</sup>, respectively. Also this change was also proved by the current density values at 1.7 V as 2 mA cm<sup>-2</sup> and 12 mA cm<sup>-2</sup>, respectively.[105] In 2015, Cady *et al.* investigated electrocatalytic behavior of Li mixed transition metal oxides, where the transition metals are manganese and cobalt. They mixed the cobalt and manganese in various ratios and synthesized mesoporous nanocrystalline forms. They reported that with increasing cobalt amount in the oxide, the Tafel slope decreased from 140 mV dec<sup>-1</sup> to 50 mV dec<sup>-1</sup>. Same stoichiometric ratio of manganese and cobalt in LiMnCoO<sub>4</sub> was reported as 120 mV dec<sup>-1</sup>. Overpotential values at 1 mA, was reduced from 550 mV to 370 mV by increasing the cobalt species. At 10 mA, the LiCo<sub>2</sub>O<sub>4</sub> provided a 410 mV overpotential.[104]

In 2018, Dag *et al.* synthesized mesoporous LiCoO<sub>2</sub> having surface area 62 m<sup>2</sup> g<sup>-1</sup> by using MASA method and they reported a Tafel slope of 49 mV dec<sup>-1</sup> with an overpotentials of 282 mV at 1 mA cm<sup>-2</sup> and 376 mV at 10 mA cm<sup>-2</sup> current densities.[106] Then, they worked on stable mesoporous LiMn<sub>2-x</sub>Co<sub>x</sub>O<sub>4</sub> electrodes, where x is 0, 0.5, 1, 1.5, 2 for OER and improved the efficiencies and stabilities of the electrodes by using MASA approach to have mesoporous and perfectly smooth thin films with remarkable surface areas.[34].

In this thesis, the characterization methods of mesoporous  $\text{LiMn}_{2-x}\text{Co}_x\text{O}_4$  thin films and their electrocatalytic performances in OER were investigated and as a continuation of the project, improvement of the performance of electrodes in OER by modification of the  $\text{LiMn}_{2-x}\text{Co}_x\text{O}_4$  films were shown.

## 1.3 Electrochemical Background of Water Oxidation Reaction Electrocatalysts

### 1.3.1 Cyclic Voltammetry

Cyclic voltammetry (CV) is one of the substantial technique in the electrochemistry and it is used to understand the redox behavior of chemicals. Definition of CV is sweeping the potential linearly with time and collecting the current at each potential. [107]–[109] According to IUPAC convention, CV is shown like sweeping of potential is from negative voltage (left) to positive voltage (right) and it brings that anodic current or oxidation peak is in positive current side and cathodic current (reduction) is in negative current side in the cyclic voltammograms, see Figure 1.6. Also, as seen in the cyclic voltammograms, the OER is appeared after 0.6 V vs

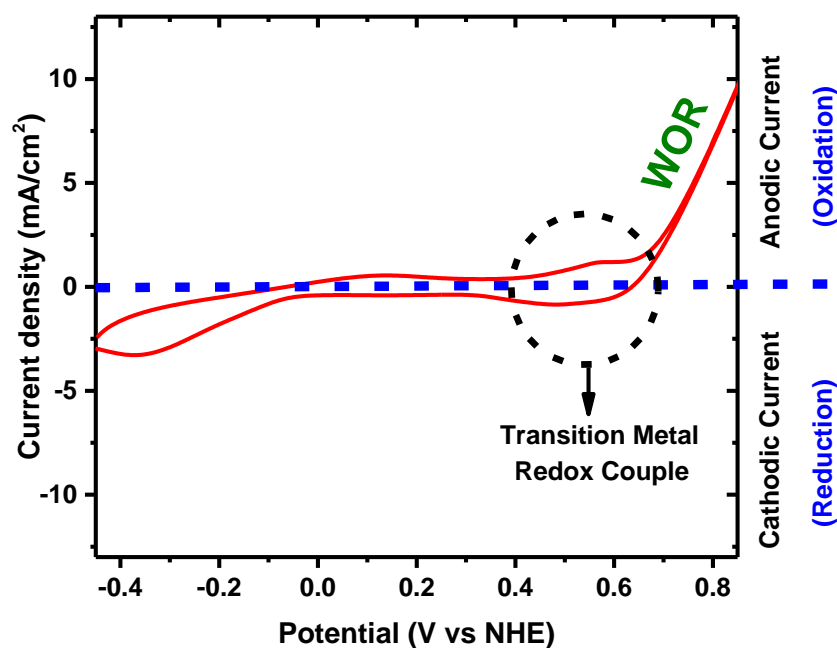


**Figure 1.6.** Typical cyclic voltammogram of a transition metal oxide working electrode.

NHE and it is understood by sharp increase in current density by sweeping the potential up to 0.85 V.

CV is a very useful technique to understand behavior of redox species on surface, OER efficiency, and performance of the catalysts in OER. For a detailed electrochemical measurement, generally CV is analyzed to determine potential ranges showing various redox processes and detailed investigation is started after determination these voltages. With the help of CV, the surface concentration, capacitance property, Tafel slope analysis etc. could be done easily.

### 1.3.2 Surface Concentration of Active Redox Species

Cyclic voltammetry could be used to evaluate the surface concentration of an electrode in terms of redox active species. In most catalytic electrochemical reactions, species in electrolyte are adsorbed on the electrode surface, where the redox reaction takes place. In the CV curve, this process appears as oxidation and reduction peaks. So, the current of these peaks of the electrode-adsorbed species is directly dependent on the scan rate and by this dependence, the surface coverage could be obtained. [107], [108] In Equation 1.2, the relation among the current density of peak ( $i_p$ ), scan rate ( $v$ ), and surface coverage ( $\Gamma$ ) are shown.

$$i_p = \frac{n^2 F^2}{4RT} v A \Gamma \quad \text{(Equation 1.2)}$$

Where  $i_p$  is the current of the peak (top) (A),  $n$  is the number of electron,  $F$  is the Faraday constant,  $96485 (C mol^{-1})$ ,  $R$  is the gas constant,  $8.314 J K^{-1} mol^{-1}$ ,  $T$  is the temperature ( $^{\circ}K$ ),  $v$  is the scan rate ( $V s^{-1}$ ),  $A$  is the electrode area ( $cm^2$ ),  $\Gamma$  is the surface coverage ( $mol cm^{-2}$ )

Notice that the current  $i_p$  of a redox peak is, for both oxidation and reduction case, linearly proportional with the scan rate. In 2003, this equation has been driven to another form[110], see Equation 1.3.

$$slope = \frac{n^2 F^2 A \Gamma}{4RT} \quad \text{(Equation 1.3)}$$

According to the equation, the CV are recorded several times by increasing or decreasing scan rate with an equal interval and for each scan rate value, the current density values of the peak were collected. The slope is obtained by plotting the scan rates versus their current values and used for the calculation of surface-adsorbed specie. By this method, instead of using only one scan rate, a correlation between the scan rate and current values of peaks is obtained and by linear fitting of the data,  $i_p$  vs  $v$ , the redox process species on surface could be analyzed.

### 1.3.3 Capacitance

Cyclic voltammetry is also used for calculation of surface charge density, ( $q$ ) of an electrode and by dividing this charge density into potential range that is scanned from initial voltage to final voltage, capacitance ( $C$ ) or specific capacitance ( $C_s$ ) (in case of known catalytic load), of the electrode surface could be interpreted. The equation to obtain specific capacitance ( $C_s$ ) by a cyclic voltammogram is represented in Equation 1.4. [111], [112]

$$C_s = \frac{1}{2 m v \Delta V} \int i dV \quad \text{(Equation 1.4)}$$

Where  $C_s$  is the specific capacitance ( $F g^{-1}$ ),  $m$  is the catalytic load ( $g$ ),  $v$  is the scan rate ( $V s^{-1}$ ),  $\Delta V (V_f - V_i)$  is potential range of the CV curve ( $V$ ),  $\int i dV$  is the polygon area of CV curve ( $A V$ )

Most of times, the catalytic material is coated on a conducting substrate in small amount and generally used as a thin film. For the same reason, the catalytic load ( $m$ ) couldn't be reliably determined. Therefore, instead of reporting specific capacitance, just capacitance of the electrode is reported by using the same equation without dividing into catalytic load.

### 1.3.4 Tafel Equation and Tafel Slope

Tafel equation is used for reporting the electrocatalytic activities of catalysts that are used in water splitting processes and other energy fields. The equation was introduced by Julius Tafel in 1905 and informs about electrode kinetic in catalytic reactions.[107] According to the equation, the logarithm of current ( $\log i$ ) is linearly dependent to the overpotential ( $\eta$ ), see Equation 1.5. [107], [113], [114]

$$\eta = a + b \log(i) \quad \text{(Equation 1.5)}$$

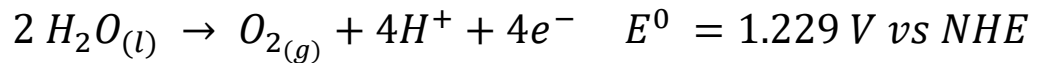
Where  $\eta$  is the overpotential (V),  $i$  is the current (A), (alternatively current density,  $j$  could be used ( $A\ cm^{-2}$ )),  $b$  is the Tafel slope ( $V\ dec^{-1}$  or  $mV\ dec^{-1}$ ),  $a$  is an empirical value.[114]

According to the Tafel equation, in an electrochemical reaction logarithm of current or current density is linearly dependent on overpotential but this linearity depends on a parameter “b” in the equation, known as “Tafel slope”. For a good activity of a catalysts, smaller values of Tafel slope are desired. Because a lower overpotential should result a higher current density. Therefore, lower Tafel slope is a good indicator for a good activity of a catalyst in a reaction.[115]

### 1.3.5 Origin of the Overpotential in Water Oxidation Reaction

In the analysis of electrocatalysis, performance of a material could be reported as an overpotential during the OER. The overpotential is extracted from the Nernst equation indirectly.

Water oxidation reaction (OER) is written as [107]:



According to OER, the reaction includes 4 electrons as discussed before and contains  $4H^+$  with a standard potential of 1.229 V vs NHE (at pH 0). By placing the components of the OER on Nernst equation[107], the potential could be calculated, see Equation 1.6.

$$E = E^0 + \frac{RT}{nF} \ln P_{O_2} [H^+]^4 \quad \text{(Equation 1.6)}$$

Where  $E$  is the potential (V),  $E^0$  is the standard potential (for OER: 1.229 V),  $R$  is the gas constant,  $8.314\ J\ K^{-1}\ mol^{-1}$ ,  $T$  is the temperature ( $^{\circ}K$ ),  $n$  is the number of electrons,  $F$  is the Faraday constant,  $96485\ (C\ mol^{-1})$ ,  $P_{O_2}$  is 1 atm.[107]

The potential (E) could be found using Equation 1.6. Because of H<sup>+</sup> ion concentration, the potential is dependent on the pH of the environment. So, the Equation 1.6 can be rewritten as in Equation 1.7.

$$E = 1.229V + 0.059 \text{ pH (V vs NHE)} \quad \text{(Equation 1.7)}$$

So, the potential or energy required for OER, decreases with increasing pH of the media. This effect has been shown in many studies by using same electrode in different pH of acidic and alkaline mediums.[116]–[118] So, many metal oxides are performed in alkaline medium with pH 14 because these pH value brings a potential as 0.404 V vs NHE and it means energy required for OER at pH 14 is very low. According to this potential definition, the potential required to evolve oxygen gas is decreased by increasing pH of solution, used as an electrolyte. The calculated potential, extracted from the Equation 1.7, is the required potential in case a perfect catalyst and the system without a resistance, having only diffusion problems. It also means the potential is only spent for an electron-transfer. Otherwise, the additional potential, required to drive the reaction, is called overpotential and it is represented by a symbol, “ $\eta$ ”.[107] So, using alkaline solutions or higher pH is because of decreasing E by 0.059 times pH.[70] The efficiency of a catalyst in OER is reported by  $\eta$  in voltage unit at an exact current density. Small additional potential represents a better catalytic performance in electrochemical reaction. So, the overpotential is obtained by using Equation 1.8.

$$\eta = E^{exp} - E \quad \text{(Equation 1.8)}$$

Where  $E^{exp}$  is experimental potential (V),  $E$  is potential (V).

# Chapter 2

## Experimental Section

### 2.1 Synthesis of Mesoporous Materials

#### 2.1.1 Preparation of Solutions of Salts and Surfactants

The solutions of salts and surfactants were prepared using  $\text{LiNO}_3$ ,  $[\text{Mn}(\text{H}_2\text{O})_4](\text{NO}_3)_2$  and  $[\text{Co}(\text{H}_2\text{O})_6](\text{NO}_3)_2$  salts, pluronic, P123 (tri-block copolymer,  $\text{EO}_{20}\text{-PO}_{70}\text{-EO}_{20}$ , where EO is ethylene oxide blocks and PO is propylene oxide block) as a non-ionic surfactant and cetyltrimethylammonium bromide (CTAB) as a charged surfactant, concentrated  $\text{HNO}_3$  (65 %), and absolute ethanol (99.9 %). All the chemicals were purchased from Sigma-Aldrich corporation and used without further purification.

All the solutions were prepared in 25 ml vials. In a general solution preparation, first, P123 is completely dissolved in a 5 ml ethanol by stirring on magnetic stirrer for 5 min and then CTAB is added to the solution by stirring. To this clear solution, first  $\text{LiNO}_3$  salt at once and finally  $\text{HNO}_3$  are added dropwise and stirred for 5 min to obtain a homogenous clear solution. The transition metal salts ( $[\text{Mn}(\text{H}_2\text{O})_4](\text{NO}_3)_2$  and  $[\text{Co}(\text{H}_2\text{O})_6](\text{NO}_3)_2$ ) are added to the above clear solution sequentially with 5 min intervals. Then, the vial is sealed to prevent any ethanol evaporation during stirring for 24 hours to obtain a homogenous and clear solution. In case of cobalt free solutions,

the same procedure is used without the addition of the cobalt nitrate salt. A schematic representation of the general solution preparation is shown in Figure 2.1.

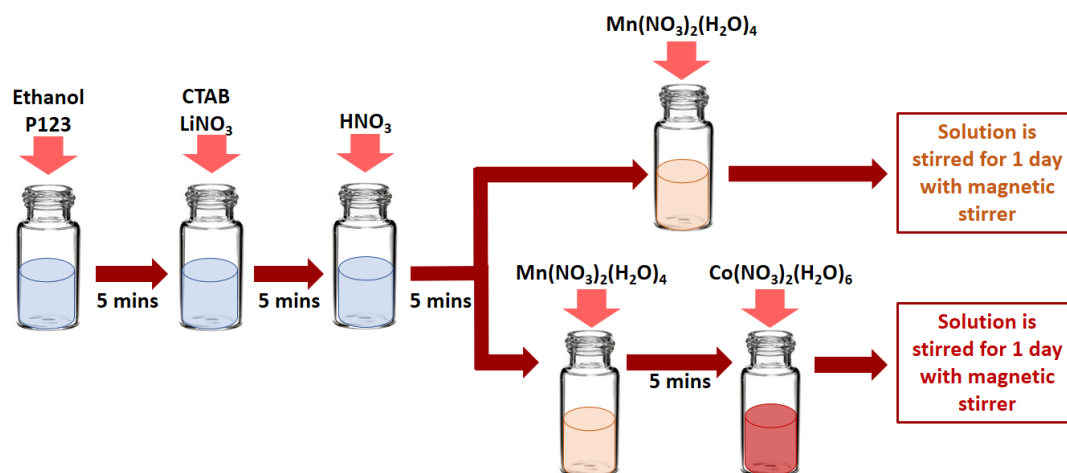


**Figure 2.1.** Schematic representation of the preparation procedure of the salts-surfactants solutions.

Amount of each ingredient for all solutions are tabulated in Table 2.2. In all solutions, the charged to non-ionic surfactant mole ratio was kept to be 1.0 and the total salt/P123 mole ratio of 60 (20 lithium salt and 40 transition metals). Ethanol and nitric acid amounts were also kept constant in all solutions, 5 g and 0.55 g, respectively. Instead of using mole ratio labeling for the solutions, mole percentage of manganese and cobalt were used because all other chemicals mole ratios were kept as constant. In Table 2.1, the mole percentage notation is given.

<b>Mol ratios of chemicals in the solutions Li-Mn-Co-CTAB-P123</b>	<b>Notation of mole percentage of Mn%-Co% in the solutions</b>
20Li-40Mn-1CTAB-1P123	Mn100-Co0
20Li-30Mn-10Co-1CTAB-1P123	Mn75-Co25
20Li-20Mn-20Co-1CTAB-1P123	Mn50-Co50
20Li-10Mn-30Co-1CTAB-1P123	Mn25-Co75
20Li-40Co-1CTAB-1P123	Mn0-Co100
40Mn-1CTAB-1P123	Mn100*
40Co-1CTAB-1P123	Co100*

**Table 2.1.** Mol ratios of chemicals in the solutions and notation of the solutions by mole percentages of Mn(II) and Co(II) salts.

Notation of the solutions Mn%-Co%	Weight of LiNO <sub>3</sub> (g)	Weight of Mn(NO <sub>3</sub> ) <sub>2</sub> (g)	Weight of Co(NO <sub>3</sub> ) <sub>2</sub> (g)	Weight of CTAB (g)	Weight of P123 (g)	HNO <sub>3</sub> (g)	EtOH (g)
Mn100-Co0	0.173	1.254	-	0.045	0.725	0.55	5
Mn95-Co5	0.173	1.192	0.073	0.045	0.725	0.55	5
Mn90-Co10	0.173	1.129	0.146	0.045	0.725	0.55	5
Mn85-Co15	0.173	1.067	0.218	0.045	0.725	0.55	5
Mn80-Co20	0.173	1.004	0.291	0.045	0.725	0.55	5
Mn75-Co25	0.173	0.940	0.363	0.045	0.725	0.55	5
Mn50-Co50	0.173	0.627	0.727	0.045	0.725	0.55	5
Mn25-Co75	0.173	0.314	1.089	0.045	0.725	0.55	5
Mn0-Co100	0.173	0	1.452	0.045	0.725	0.55	5
Mn100*	-	1.254	-	0.045	0.725	0.55	5
Co100*	-	-	1.452	0.045	0.725	0.55	5

**Table 2.2.** Quantities of LiNO<sub>3</sub>, [Mn(H<sub>2</sub>O)<sub>4</sub>](NO<sub>3</sub>)<sub>2</sub>, [Co(H<sub>2</sub>O)<sub>6</sub>](NO<sub>3</sub>)<sub>2</sub>, CTAB, P123, HNO<sub>3</sub>, and ethanol, used in the solutions.

### 2.1.2. Preparation of Lyotropic Liquid Crystalline (LLC) Films

The mesophases were prepared using above clear solution by drop-cast coating for thick and spin coating for thin LLC films. The thick films were prepared on microscope slides by using 7 drops of the above homogenous solutions and aged to gelation for an hour. The thick LLC films were used to synthesize lithium transition metal oxides for some analysis that requires more powder sample. So, Lithium

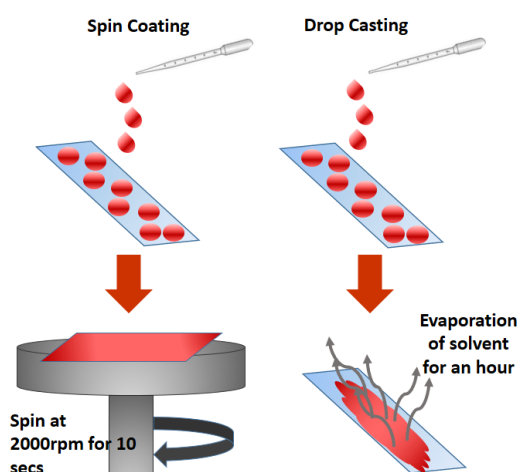


**Figure 2.2.** Schematic representation of the preparation of the LLC mesophases by spin coating and drop-cast coating methods.

transition metal oxide (LMO) thick films and powders are for large quantities. In the second path, a spin coating technique was used to obtain thin films of the LLC and LMOs. To prepare the thin films, a few drops of above solution were put on a glass substrate or FTO coated glass and spun at 2000 rpm for 10 s. The thin films were used for characterization, using a small angle XRD technique. Schematic representation of both drop-cast and spin coating methods are shown in Figure 2.2.

### 2.1.2 Synthesis of Mesoporous $\text{LiMn}_{2-x}\text{Co}_x\text{O}_4$ Films

Synthesis of mesoporous LMOs were carried using the MASA approach. The LLC films, obtained from drop-cast and spin coating processes, were calcined in a pre-heated oven at 300 °C. Drop-cast coated films were calcined for 3 hrs and scraped over the glass substrates to obtain large quantities of the powder forms for the XRD and  $\text{N}_2$  adsorption-desorption measurements. The spin coated films were calcined for 1 hr. These films were also scraped from the substrate for SEM and TEM imaging and EDX analysis. In Figure 2.3, the formation of thick and thin films of LMOs by two coating methods are shown. Table 2.4 tabulates the notations and empirical formulas of the mesoporous  $\text{LiMn}_{2-x}\text{Co}_x\text{O}_4$ .



**Figure 2.3.** Synthesis of LMOs on microscope slides by drop-cast and spin coating methods.

<b>Mole percentage notation of solutions for LLCs and LMOs Mn%-Co%</b>	<b>LMOs are synthesized by calcination of (Mn%-Co%) LLCs (LiMn<sub>2-x</sub>Co<sub>x</sub>O<sub>4</sub>)</b>
<b>Mn100-Co0</b>	<b>LiMn<sub>2</sub>O<sub>4</sub></b>
<b>Mn75-Co25</b>	<b>LiMn<sub>1.5</sub>Co<sub>0.5</sub>O<sub>4</sub></b>
<b>Mn50-Co50</b>	<b>LiMnCoO<sub>4</sub></b>
<b>Mn25-Co75</b>	<b>LiMn<sub>0.5</sub>Co<sub>1.5</sub>O<sub>4</sub></b>
<b>Mn0-Co100</b>	<b>LiCo<sub>2</sub>O<sub>4</sub></b>
<b>Mn100*</b>	<b>Mn<sub>3</sub>O<sub>4</sub></b>
<b>Co100*</b>	<b>Co<sub>3</sub>O<sub>4</sub></b>

**Table 2.4.** Percentage notations (Mn%-Co%) of LMOs and empirical formulas of LiMn<sub>2-x</sub>Co<sub>x</sub>O<sub>4</sub>.

Also, to evaluate the effect of calcination temperature on the materials, the annealing temperature was changed from 400 °C to 500 °C with 50 °C increments. For this purpose, all the samples were first calcined at 300 °C. Then, the powders, scraped from the substrates were annealed in a pre-heated oven at 400 °C for 1h and then at 500 °C for 1 more hour.

### 2.1.3 Preparation of LiMn<sub>2-x</sub>Co<sub>x</sub>O<sub>4</sub> Working Electrodes on FTO Glasses

The LMOs, synthesized using MASA process over a conductive substrate (fluorine doped tin oxide (FTO) coated glass), were used for water oxidation reaction (OER) as working electrodes (WEs). The WE was fabricated by spin coating the clear solutions of the corresponding composition, followed by a calcination with a size of 1x1cm<sup>2</sup>. In the fabrication process, half of the FTO substrate (2x1 cm<sup>2</sup>) was covered with a tape and the rest was coated using one drop of the solution and spinning the substrate at 2000 rpm for 10 s. The coated area of FTO was 1 cm<sup>2</sup>. After spin coating and gelation, the tape was removed and the gel film over the FTO was calcined at various temperatures, generally 300°C for 1h. The electrodes were used for electrochemical measurements and also for the analysis like XPS, SEM, EDX, etc. Schematic representation of the preparation of WEs are shown in Figure. 2.4.

The WEs were prepared by calcination of the LLCs on the substrate at 300 °C for 1 h and then annealing at 400 °C for 1h and 500 °C for 1 h.

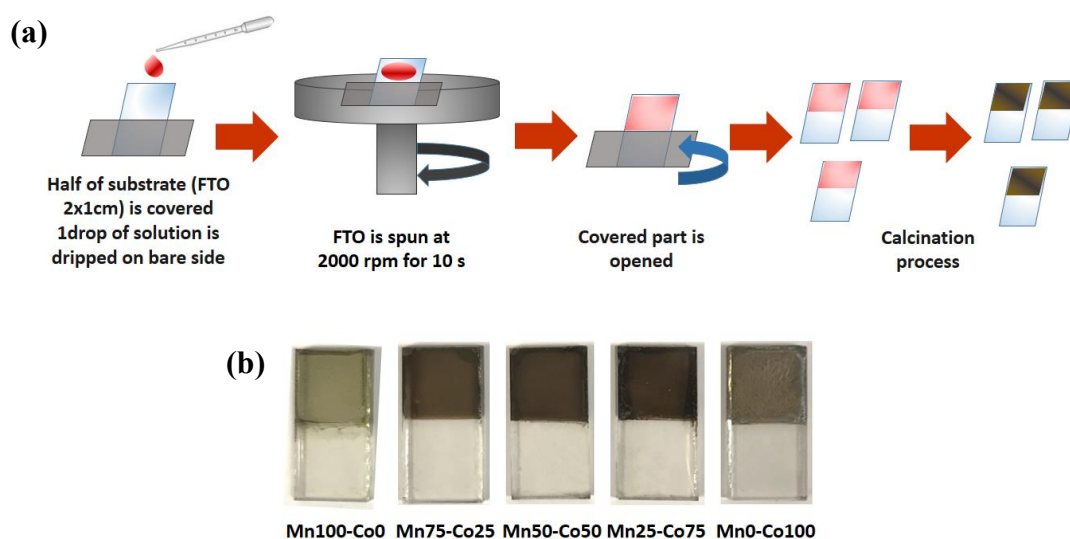


**Figure 2.4.** (a) Schematic representation of the preparation of WEs over FTO substrates (b) Photos of the WEs with various percentages of manganese and cobalt (Mn%-Co%) in  $\text{LiMn}_{2-x}\text{Co}_x\text{O}_4$  calcined at  $300\text{ }^\circ\text{C}$  for 1h.

#### 2.1.4 Preparation of $\text{LiMn}_{2-x}\text{Co}_x\text{O}_4$ Working Electrodes on Graphite Substrate

For the electrochemical measurements of the LMOs, another substrate in place of FTO was used. For this purpose, a cheap and well known material, graphite, 5mmx50mm rods were used. To coat the graphite surface with LMO, dip-coating method was employed by dipping the rods into a corresponding solution. Area that should be dipped was first estimated to coat  $1\text{ cm}^2$  and the rest of the rod was blocked by parafilm prior to coating. The dipping and pulling speed was set to  $8\text{ cm min}^{-1}$ . The rod was dipped into the solution completely at once and pulled out to obtain the LLC coated rods, see Figure 2.5. Dipped graphite rod was aged for 1 hour to evaporate excess solvent. Then, the rod was calcined in a small vial at  $300\text{ }^\circ\text{C}$  for 1h.

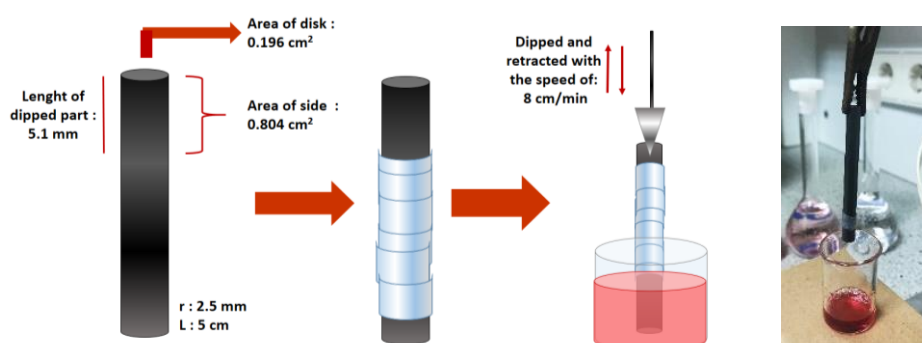


**Figure 2.5.** Schematic representation and setup of dip-coating of graphite substrate.

### 2.1.5 Preparation of Modified Electrodes by Dipping into 1 M $\text{Co}^{+2}$ Solution

The electrodes of LMOs by using FTO substrate were modified by dipping into a 1 M  $[\text{Co}(\text{NO}_3)_2](\text{H}_2\text{O})_6$  solution to coat or to deposit cobalt species on surface of LMO electrodes. The method is inspired by successive ionic layer adsorption and reaction (SILAR) method. 3 small beakers were used for this purpose, one was filled with 1 M cobalt nitrate solution, the other 2 were filled with deionized water. The LMO coated FTO was dipped into the first beaker, filled with cobalt nitrate, for 20 seconds. Then, it was hold over a paper towel to get rid of excess droplets of the solution and then dipped into the beaker filled with deionized water for another 20 s to get rid of excess cobalt in the film. In the final step, the film was dipped into the third beaker with deionized water to remove cobalt species, accept the monolayer of cobalt over pore surface. For each dipping process, a fresh deionized water was used. After dipping and washing steps, the LMOs were calcined at 300 °C for 1h. After each dipping and calcination, the same procedure was repeated for 3-, 5-, and 7- times coating for more cobalt deposition on the pore surface. Schematic representation for modification of electrodes is depicted in Figure 2.6.

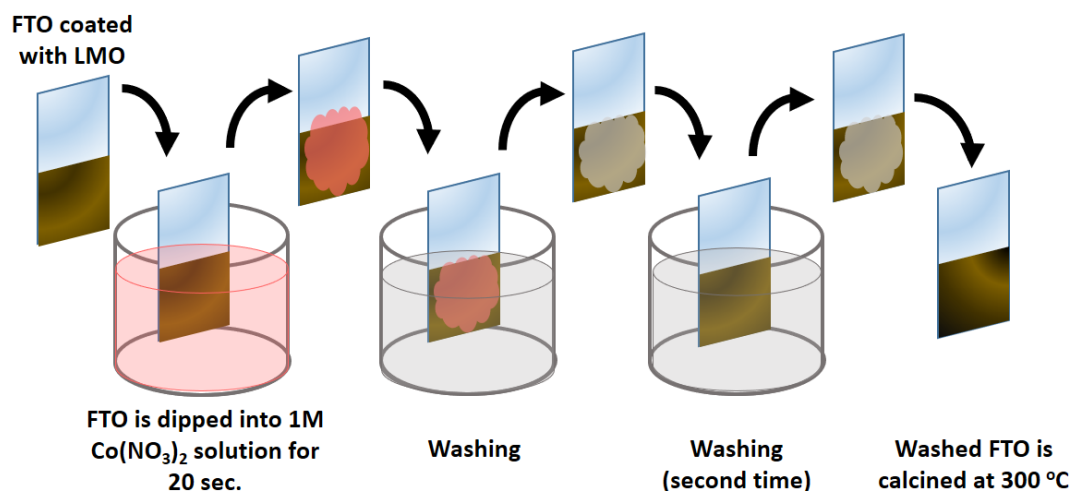


**Figure 2.6.** Schematic representation of modification of electrodes by dipping into 1M  $\text{Co}^{+2}$  solution.

## **2.2 Instrumentation**

### **2.2.1 X-ray Diffraction (XRD) Measurements**

Small angle and wide angle X-ray diffraction patterns of the LLC thin films on the microscope slide were collected using Rigaku Miniflex diffractometer, equipped with an X-ray source, Cu K $\alpha$  (1.54056 Å) operated at 30 kV and 15 mA. The microscope slide, coated with an LLC phase was inserted into the sample holder position in the diffractometer and the XRD patterns were collected between 1 and 5° with a scan rate of 0.5° min<sup>-1</sup>. The wide angle XRD patterns were collected in the range of 10 to 80° with 3° min<sup>-1</sup> scan rate.

The wide angle XRD patterns of powders were recorded using Panalytical multipurpose X-ray diffractometer, equipped with a Cu K $\alpha$  source (1.54056 Å), operated at 45 kV and 40 mA. The materials were obtained by scratching slides and packed smoothly on silicon holder as a powder. The XRD patterns were collected between 10° and 80° with the scan step size 0.01313° and scan rate 3° min<sup>-1</sup>.

The patterns recorded by X-ray diffractometers were compared and indexed by using PDF cards of Joint Committee on Powder Diffraction Standards (JCPDS).

### **2.2.2 Attenuated Total Reflection Fourier-Transform Infrared (ATR-FTIR) Spectroscopy**

Powder ATR-FTIR-spectra were collected using Bruker Alpha Platinum spectrometer with a resolution of 4 cm<sup>-1</sup> and 64 scans in the range of 400-4000 cm<sup>-1</sup>. Little amount of the powder was placed on diamond micro plate of the spectrometer and squeezed to form compact powder.

### **2.2.3 N<sub>2</sub> (77.4 K) Adsorption-Desorption Isotherms**

150 mg of a scratched powder from the glass slides was used to measure the isotherms. Before the N<sub>2</sub> sorption measurement, the powder samples were dehydrated for 2 hrs at 200 °C in a vacuum. The isotherms were recorded using TriStar 3000 automated gas adsorption analyzer in the relative pressure range of 0.01 to 0.99 atm. Saturated pressure measurements were repeated with 120 minute intervals. Surface area of the materials were obtained by 5 points in the range of 0.05 to 0.3.

#### **2.2.4 Scanned Electron Microscope (SEM) – Energy Dispersive X-ray Spectroscopy (EDX)**

The SEM images of the materials were collected using a FEI-Quanta 200 FEG at 15 kV. Very little amount of powder scraped from a microscope slide or FTO, was placed on a carbon tape that is placed on an aluminum stub. The same sample was used for the EDX data and to collect the data, a silicon drift detector (SDD) was used with a cooling system.

#### **2.2.5 X-ray Photoelectron Spectroscopy (XPS)**

XPS spectra were obtained using powders of LMO by placing it over a XPS holder with a metal ribbon to provide electron flow. Thermoscientific K-alpha device with Al K $\alpha$  monochromatic source (1486.68 eV) was used. The experiments were performed with a spot size of 400  $\mu$ m under ultra-high vacuum conditions. The data collected were calibrated according to C 1s peak.

### **2.3 Electrochemical Measurements and Analysis**

The electrodes, prepared over FTO, were used for the electrochemical measurements. The experiments were focused on active redox species on electrode surfaces and water oxidation efficiencies. The measurements were performed using a Gamry Instrument, Potentiostat – PCI4G750 and three electrode system. The polypropylene cell was used to inhibit aging effect of the electrolyte. As reference electrode (RE), Ag/AgCl (3.5M KCl) was used and potential was converted and reported with respect to normal hydrogen electrode (NHE). A platinum wire was used as a counter electrode (CE) and the working electrodes (WE) were synthesized LMOs over FTO substrates. The experiments were performed in an alkaline medium, 1 M KOH electrolyte. The electrochemical setup is shown as an illustration in Figure 2.7. Prior to the electrochemical measurements, nitrogen gas was purged into the electrolyte solution for 15 minutes to get rid of any dissolved oxygen and by using the same setup in Figure 2.7. The cyclic voltammetry (CV), chronoamperometry (CA), and chronopotentiometry (CP) measurements were done subsequently for each electrode.

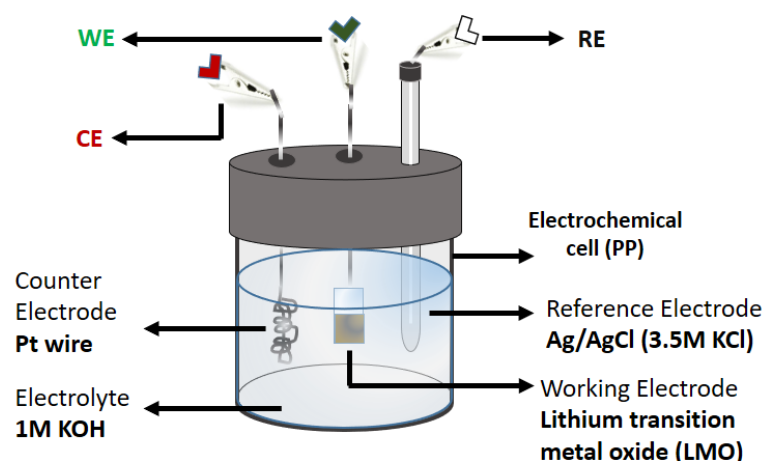


**Figure 2.7.** Electrochemical setup illustration for three electrode system.

### 2.3.1 Cyclic Voltammetry (CV)

CVs of the WEs were recorded in the potential range of  $-0.4$  V and  $1$  V (V vs NHE) with a scan rate of  $50$   $\text{mV s}^{-1}$ . For each cyclic voltammogram, three cycles were collected, where the 2<sup>nd</sup> cycle was presented. Positive feedback method was not applied during measurements, so all measurements and their curves were reported without IR compensation. Before going to a next step (e.g. CA to CP), cyclic voltammogram of electrodes was recorded to check whether there was any problem in the electrodes or setup.

Also, from the CV curves of an electrode some analysis could be done, such as the surface concentration of active redox species and calculation of charge or capacitance value of an electrode surface could be obtained.

#### 2.3.1.1 Data Analysis of Surface Concentration of Active Redox Species

The active redox concentration of an electrode surface was calculated using an equation, derived from the Nernst equation (see Equation 1.3). Firstly, the potential range of the redox reaction of active surface species is determined. Then, a set of CV is run in this potential range using a series of scan rates, depending on kinetics on surface. Figure 2.8 shows a set of CVs from a material as an example for determination of the potential range of redox species on the surface and CV curves recorded at a series of scan rates.

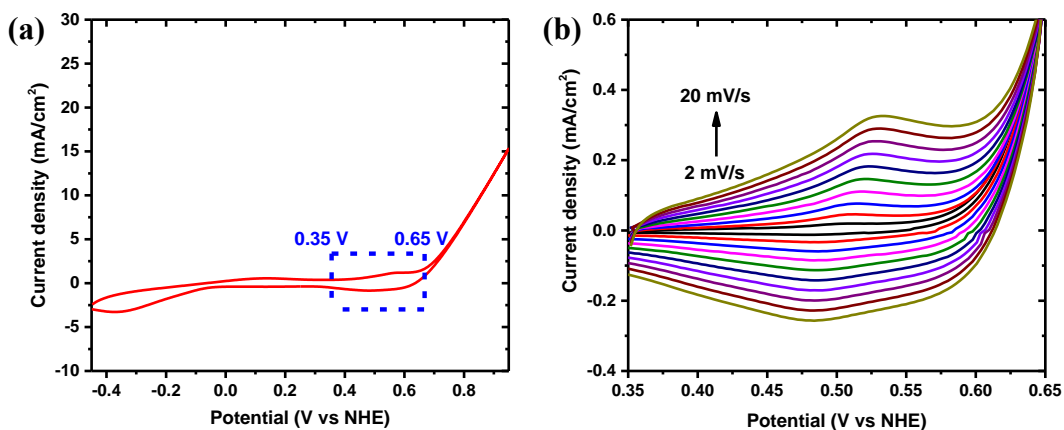


**Figure 2.8.** (a) Determination the potential range of redox couple as between 0.35 V and 0.65V (b) Set of CV curves recorded by increasing scan rate from 2 mV s<sup>-1</sup> to 20 mV s<sup>-1</sup> with intervals of 2 mV s<sup>-1</sup>.

Maxima of the peaks (oxidation or reduction) of each CV curves, shown in Figure 2.8 (b), are determined (as indicated in Figure 2.9 (a)). These values are plotted as function of scan rate (see Figure 2.9 (b), in this example, oxidation peaks were used).

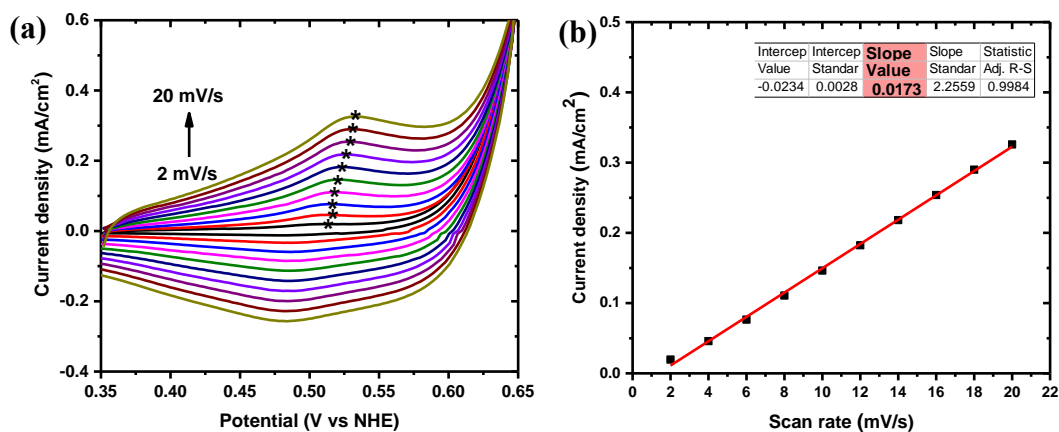


**Figure 2.9.** (a) CV curves with a series of scan rates (2 to 20 mV s<sup>-1</sup>) (b) Plot of current densities of peaks (maxima) vs scan rate to obtain the slope.

From the linear fit of the data, the slope of the fit is obtained and used in Equation 1.3 and by introducing the other components of the equation, the surface concentration ( $\Gamma$ ) of electrode is calculated and reported as nmol cm<sup>-2</sup>. In this example, the surface concentration of the redox couple,  $\Gamma$ , is found to be 18.42 nmol cm<sup>-2</sup>.

### 2.3.1.2 Calculation of Capacitance of the Electrodes

A CV curve could be used for calculation of capacitance or specific capacitance (in case of known catalytic load) of an electrode. The potential range of the redox (both oxidation and reduction) peaks is determined by the first CV curve. Then, using this potential range, a new CV curve is obtained with any scan rate. So the mathematical area of the curve is calculated in AV. The mathematical area of a CV curve that includes both oxidation and reduction is represented in Figure 2.10.

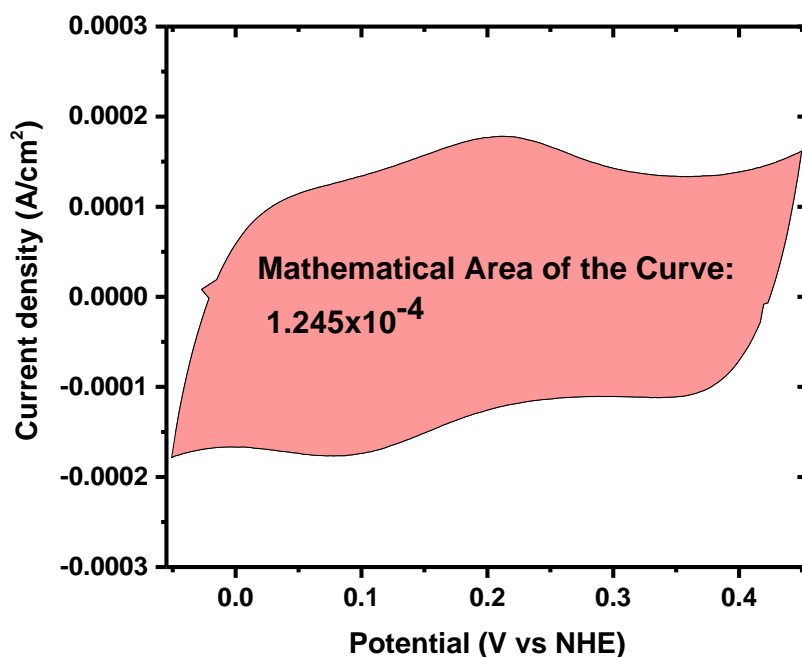


**Figure 2.10.** CV curve in a potential range (between -0.05 and 0.45 V) of a redox couple with the scan rate of 20 mV s<sup>-1</sup>.

Capacitance of an electrode could be calculated using Equation 1.4. So, for the use this equation,  $\int idV$  should be extracted from the CV curve; this term is equal to the area of the curve and used in the equation in place of  $\int idV$ . By inserting the other components of the equation, the capacitance of the electrode is calculated.

In example shown in Figure 2.10, the mathematical area is found to be  $1.245 \times 10^{-4}$  AV and catalytic load is 150  $\mu\text{g}$ ,  $\Delta V$  is 0.5 V and scan rate is 0.02 V s<sup>-1</sup>. As a result of this calculation, the specific capacitance  $C_s$  is found to be 41.5 F g<sup>-1</sup>.

### 2.3.2 Chronoamperometry (CA)

Pre-determined potentials were applied to WE to collect current data. At each potential, the potential was applied for 5 to 10 mins, depending on how fast a stable current level is reached. During the experiment, electrolyte was stirred using a magnetic stirrer. After time interval that potential is applied, last data point (of current) of the measurement is reported and used.

#### 2.3.2.1 Tafel Slope Analysis

Tafel slopes were determined with the help of chronoamperometry experiments. For this analysis, starting potential of the water oxidation reaction is determined by first CV and an earlier potential value is adjusted as a starting point of chronoamperometry experiment. In Figure 2.11, determination of OER and starting point of CA is shown.

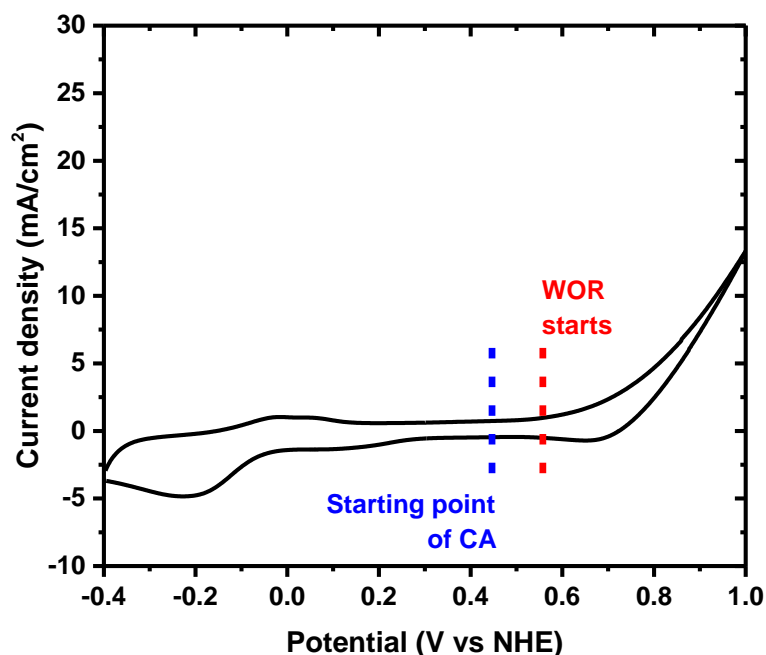


**Figure 2.11.** Determination of OER starting and starting potential of CA experiment.

With the determination of the starting point for the CA experiment, an adjusted potential is applied to WE by CA 5 or 10 minutes and the current value at the end of the experiment is noted. This step is repeated at every 20 mV (0.02 V) increments and current values are noted for each potential. Then, each current value is converted into

log(i) or log (j) and these logarithm values of currents is plotted to overpotential values that applied in CA experiment, see Figure 2.12.

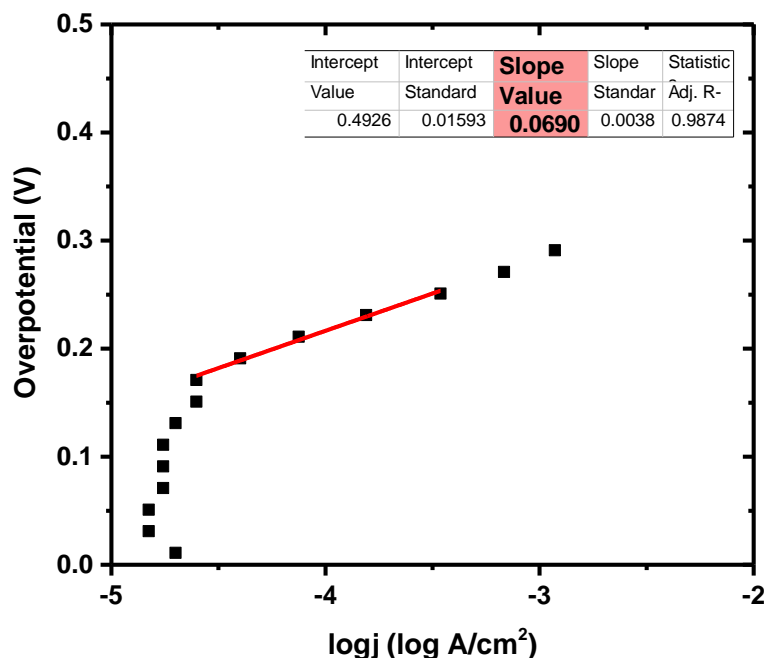


**Figure 2.12.** Plot of logi vs overpotential extracted by CA experiment and linear fitting.

According to the Tafel slope (see Equation 1.5) the potential vs logarithm of current should show a linear trend. So, in the plot, the linear region is determined, fitted and reported as Tafel slope. In the example, Tafel slope value is found as 0.069 V dec<sup>-1</sup> and this value is reported as 69 mV dec<sup>-1</sup>. Also from this linear fit, Tafel equation could be also extracted and overpotential value for 1 mA and 10 mA could be obtained by inserting these current values. So estimated overpotential values could be calculated.

### 2.3.3 Chronopotentiometry (CP)

Current density was fixed at various values, such as 1 mA cm<sup>-2</sup>, 10 mA cm<sup>-2</sup> etc. to obtain the potential values on the WEs. The potential data were collected for 1 hour to 12 hours. In the experiment, the electrolyte was always stirred with the help of a magnetic stirrer. The last data point was reported as a voltage value of a CP experiment.

### ***2.3.3.1 Overpotential reporting by CP experiment***

Chronopotentiometry experiment is performed by fixing the current density on the electrode. Then, potential required for the OER is subtracted from the collected data. The potential for OER in pH 14 is 0.404 V vs NHE and 0.199 V vs Ag/AgCl (3.5 M) According to the reference electrode that is used in the experiment, the potential could be determined and last point of the CP experiment is reported as the overpotential.

# Chapter 3

## Results & Discussion

### 3.1 Characterization of Liquid Crystalline Mesophases of Lithium, Two Transition Metal Salts (Mn(II) and Co(II)) and Two Surfactants System

Solutions of all ratios were stirred for 1 day to obtain homogeneity. The solutions were coated on glass substrates and evaporation of excess solvent was provided. The lyotropic liquid crystalline (LLC) mesophases of all ratios of the solutions were prepared by spin coating at 2000 rpm for 10 s and their small angle XRD were obtained as their as-prepared forms. Also to investigate stability of LLC films, high angle XRD patterns were obtained to observe whether salt uptake formed in mesophase.

#### 3.1.1 Liquid Mesophase Formation and Characterization

Lyotropic liquid crystalline (LLC) mesophases are formed by mixing salts and surfactants. The surfactant domains form the mesophase in which the salt species fill the hydrophilic nanospaces. Simply, first step involves a preparation of clear solution of salt-surfactant mixture in ethanol. After evaporation of ethanol, the aggregated surfactant domains (micelles) get together with an ordered LLC mesophase.

In all transition metal salt/P123 mole ratios of  $[\text{Mn}(\text{H}_2\text{O})_4](\text{NO}_3)_2$  and  $[\text{Co}(\text{H}_2\text{O})_6](\text{NO}_3)_2$ , the LLC mesophase formed, as shown by a small angle XRD measurement, see Figure 3.1.

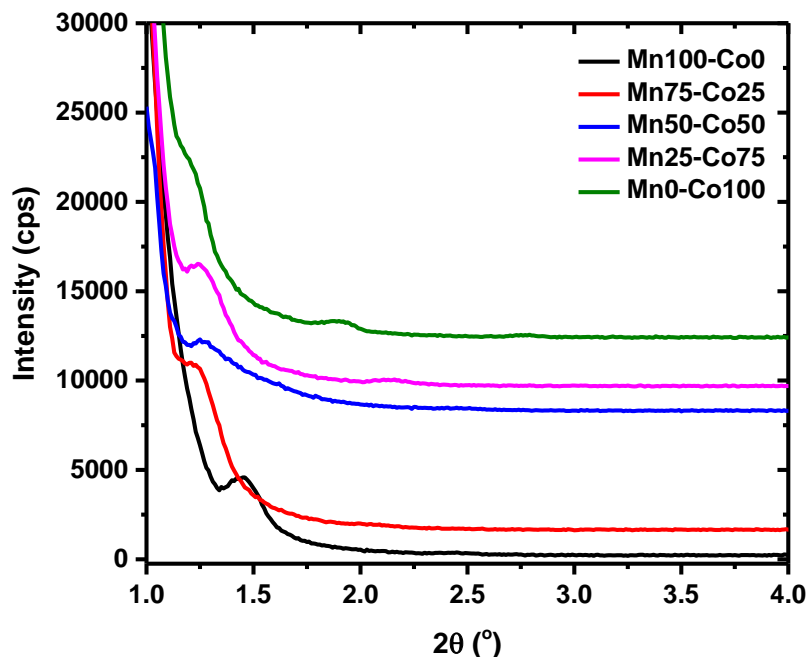


**Figure 3.1.** Small angle XRD patterns of LLCs of 20Li-40(Mn%-Co%)-1CTAB-1P123 with increasing cobalt ratio from top to bottom, prepared by spin coating at 2000 rpm for 10 s.

According to the XRD data, the increase in the  $[\text{Co}(\text{H}_2\text{O})_6](\text{NO}_3)_2$  mole percentage in the LLC mesophase causes a shift on the diffraction line to a lower angle. It means that the unit cell of the LLC mesophases get larger with the addition of cobalt nitrate salt. When the mesophase has mostly cobalt salt inside, the second diffraction line becomes well resolved at around  $2^\circ$ ,  $2\theta$ . Considering the Bragg's law ( $2d\sin\theta = n\lambda$ , where  $\theta$  is half of the measured angle in the pattern,  $d$  is d-spacing, and  $\lambda$  is the wavelength of the X-ray, 1.54056 Å,  $n$  is 1), d-spacing of the LLC mesophases can be evaluated from the diffraction lines, see Table 3.1.

<b>Mn%-Co% notation</b>	<b>1<sup>st</sup> Line (°)</b>	<b>d-spacing (Å)</b>
<b>Mn100-Co0</b>	<b>1.45</b>	<b>60.88</b>
<b>Mn75-Co25</b>	<b>1.21</b>	<b>72.95</b>
<b>Mn50-Co50</b>	<b>1.25</b>	<b>70.62</b>
<b>Mn25-Co75</b>	<b>1.24</b>	<b>71.18</b>
<b>Mn0-Co100</b>	<b>1.20</b>	<b>73.56</b>

**Table 3.1.** Diffraction angles and d-spacing values of the LLC mesophases of as prepared 20Li-40(Mn%-Co%)-1CTAB-1P123 samples.

There is a significant change in the first diffraction line (from 61 to 71 Å) with an addition of 25% cobalt salt (mole %) to the media, but the change at higher ratios are not significant, almost constant at around 71 Å.

The structure of the LLC mesophases in all mole ratios of cobalt and manganese salts, are cubic. The proof comes from the polarized optical microscope images of LLC phases, the POM images are dark in all LLC mesophases in all ratios, indicating the cubic structures.[39]

### 3.1.2 Liquid Crystalline Mesophase Stability

Stability of the LLC mesophases is very important because they are used to synthesize mesoporous and pure materials. Salt uptake in mesophase is also as important to preserve the structure and composition in the mesoporous materials after calcination step. If the transition metal salts are leached out from the mesophase, they usually form their bulk metal oxide. In addition to salt crystallization, a formation of a tetrabromometallate ion,  $[MBr_4]^{2-}$  may also leach out  $(CTA)_2[MBr_4]$  crystals. So, these formations may change the composition of the targeted compound,  $LiM_2O_4$ . To synthesize a pure  $LiM_2O_4$ , the stability of the gel phase is critical before the calcination. Therefore, the salt uptake time should be investigated. For a wright LLC to calcine to form the mesoporous  $LiM_2O_4$ , the high angle XRD patterns of the LLC were also recorded, see Figure 3.2 to inspect if there are any crystal formations.

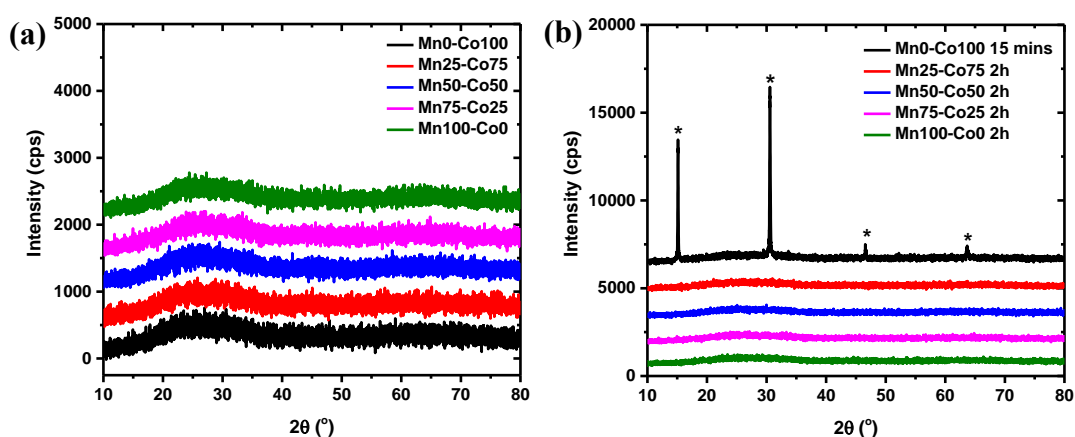


**Figure 3.2.** High angle XRD patterns of LLCs  $20Li-40(Mn\%-Co\%)-1CTAB-1P123$  (a) As prepared LLCs at 2000rpm for 10 s (b) Aged LLCs with various times (\*)  $Co(NO_3)_2(H_2O)_6$

In the XRD patterns, if the LLC phase, obtained by spin coating, does not show any diffraction in the range of  $10^\circ$  to  $80^\circ$ , it means that there is no salt crystal formation in the freshly formed mesophase. However, after 15 min aging the film of 20Li-40Co-1CTAB-1P123 (Mn0-Co100) system, the pattern displays some diffraction lines at wide angles. A similar behavior is also observed in the samples with higher salt ratios. The mesophase in the cobalt salt system has limited stability, so the cobalt nitrate salt leaches out as predicted from the XRD pattern. The pattern can be indexed to cobalt nitrate salt (PDF-00-053-0426). However, with the addition of manganese salt, the salt uptake of cobalt decreases. Simply the presence of manganese salt prevents cobalt nitrate crystallization. The LLC phase forms with a better stability, even if the gels are aged for 2 hrs or longer, no crystal formation was observed.

## **3.2 Characterization of Mesoporous $\text{LiMn}_2\text{O}_4$ and $\text{LiMn}_{2-x}\text{Co}_x\text{O}_4$ Thin Films**

### **3.2.1 Characterization of Mesoporous $\text{LiMn}_2\text{O}_4$**

Calcination of the Li(I)-Mn(II)-CTAB-P123 mesophase produces a mesoporous  $\text{LiMn}_2\text{O}_4$  thin films. For the characterization of the mesoporous  $\text{LiMn}_2\text{O}_4$ , the following techniques and procedure were employed. First the XRD patterns were collected to identify the composition, crystallinity, particle size etc. by controlling the synthesis conditions. Temperature dependent experiments have been performed to identify the thermal behaviors of the films. From the collected data, crystal size has been calculated, using full width half maximum, FWHM, of the diffraction lines, and Scherrer equation ( $D = 0.94\lambda / (B \cos\theta)$ , where D is average crystal size, B is FWHM of the diffraction line in radians,  $\theta$  is Bragg's angle,  $\lambda$  is 1.54056 Å), see Equation 1.1. Using  $\text{N}_2$  adsorption-desorption isotherms, Brunauer–Emmett–Teller (BET) surface area is calculated. The morphology of the material is obtained from the SEM images. The LLC film of 20Li-40Mn-1CTAB-1P123 (Mn100-Co0) is calcined at 300 °C and then annealed from 300 °C to 650 °C by increment of 50 °C. At all temperatures, the diffraction patterns of the mesoporous  $\text{LiMn}_2\text{O}_4$  were recorded and compared with the reference data (PDF-00-054-0252), see Figure 3.3.

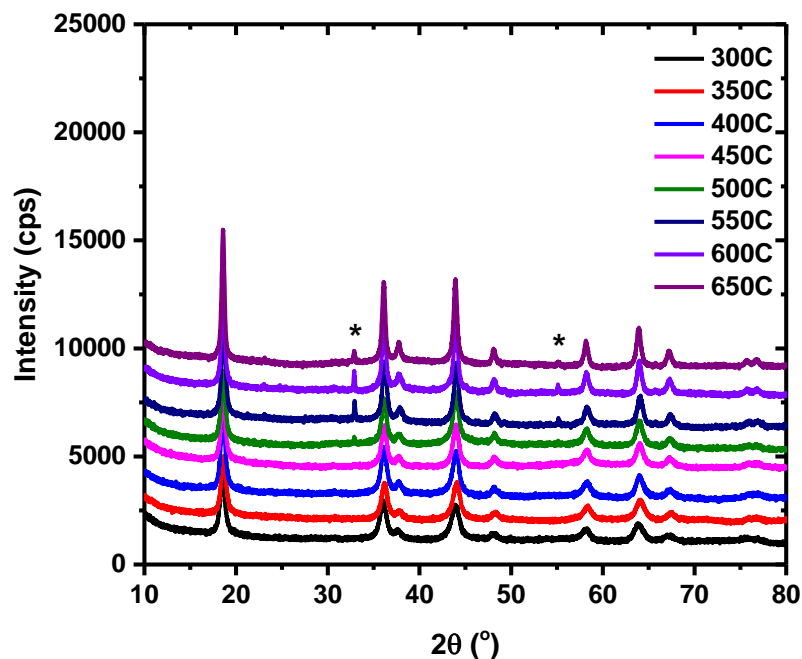


**Figure 3.3.** XRD patterns of mesoporous  $\text{LiMn}_2\text{O}_4$  (Mn100-Co0) by calcination at different temperatures 300 °C to 650 °C - (\*)  $\text{Mn}_2\text{O}_3$

According to the XRD patterns of  $\text{LiMn}_2\text{O}_4$  by increasing calcination temperature, the diffraction lines of  $\text{LiMn}_2\text{O}_4$  get sharper, indicating that the crystal size is increasing with increasing calcination/annealing temperature. Also,  $\text{Mn}_2\text{O}_3$  crystals (shown with an asterisk, \*) are formed by annealing above 500 °C (compare those signals with the reference PDF-00-041-1442). The calculated crystal size is also related to the BET surface area of the materials. If a material has small particles, it has larger surface area and its pore size is smaller. To prove this,  $\text{N}_2$  adsorption-desorption isotherms were collected and the BET surface area and crystal size with the calcination temperature were correlated. In Table 3.2, the BET surface areas and pore sizes, pore volumes are shown with the calcination temperature for the mesoporous  $\text{LiMn}_2\text{O}_4$ .

<b><math>\text{LiMn}_2\text{O}_4</math> (Mn100-Co0) calcination temperature (°C)</b>	<b>BET Surface Area (<math>\text{m}^2\text{g}^{-1}</math>)</b>	<b>BJH Pore size (nm)</b>	<b>Pore volume (<math>\text{cm}^3\text{g}^{-1}</math>)</b>
300	98	11.1	0.26
400	90	10.8	0.25
500	69	12.9	0.28
600	33	22.5	0.24

**Table 3.2.**  $\text{N}_2$  adsorption-desorption data of  $\text{LiMn}_2\text{O}_4$  at different calcination temperatures.

According to BET data of  $\text{LiMn}_2\text{O}_4$ , the surface area of the material decreases with increasing the calcination temperature. Reason of this decrease could be due to collapse of small pores into bigger ones due to the growth of the pore-walls. Therefore, it is reasonable to lose surface area. Barrett-Joyner-Halenda (BJH) pore size distribution results also show the same trend with increasing calcination temperatures, since increase in calcination temperature leads to increase in the size of mesopores.

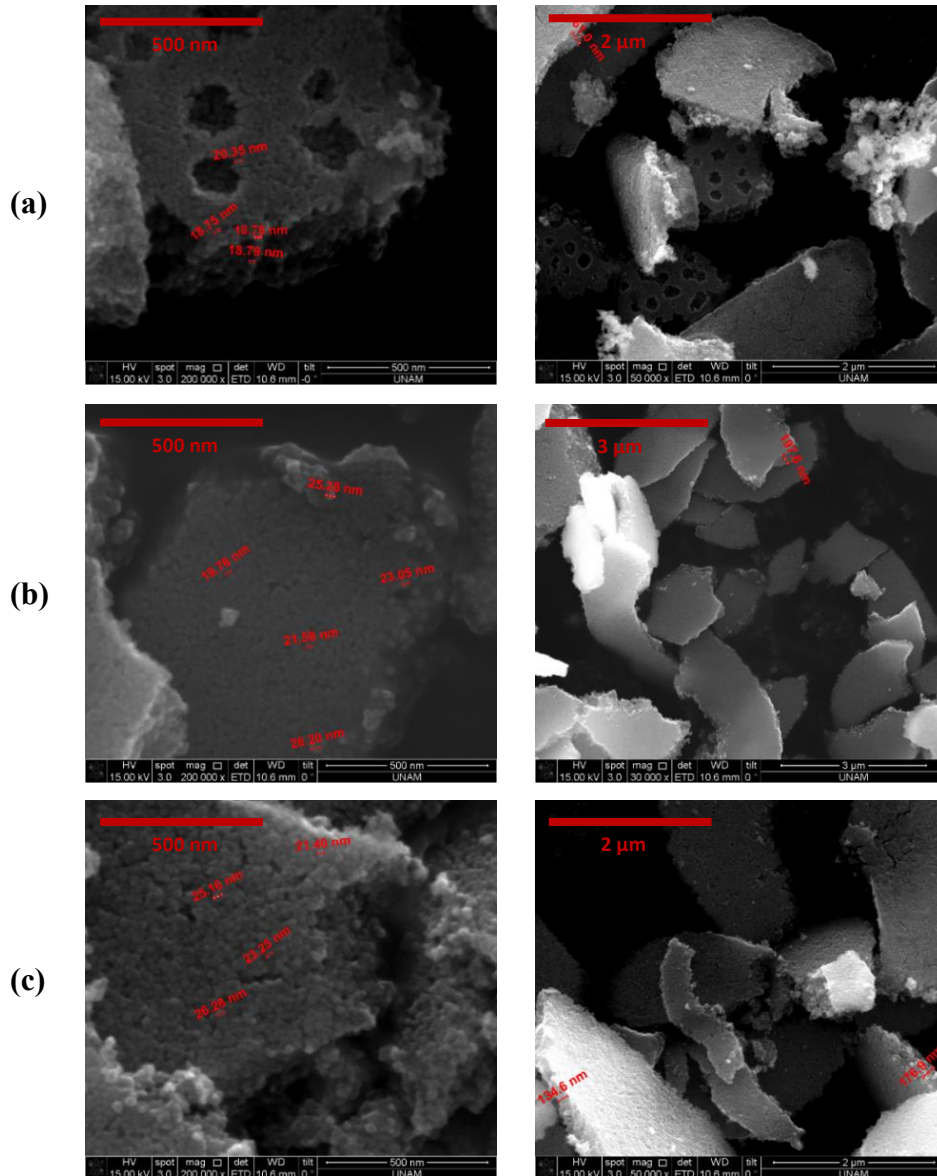


**Figure 3.4.** SEM images of  $\text{LiMn}_2\text{O}_4$  (Mn100-Co0) calcined at **a)** 300°C 1h **b)** 400°C 1h (by annealing) **c)** 500°C 1h (by annealing).

Using the same set of samples, the SEM images of the  $\text{LiMn}_2\text{O}_4$  calcined at various temperatures were also collected, see Figure 3.4. Even if resolution of the microscope is not enough to image in detail, the particle size growth has been detected with increasing annealing temperature, at a scale bar 500 nm. Also in low magnification, the film thickness was measured to be in the range of 150 to 200 nm.

### 3.2.2 Characterization of Mesoporous $\text{LiMn}_{2-x}\text{Co}_x\text{O}_4$

Calcination of the mixed salt (Mn(II) and Co(II)) mesophase also produce transparent mesoporous  $\text{LiMn}_{2-x}\text{Co}_x\text{O}_4$  films. Characterization of the  $\text{LiMn}_{2-x}\text{Co}_x\text{O}_4$  films was done by using the XRD data,  $\text{N}_2$ -adsorption-desorption isotherms, and SEM imaging (with EDX spectrum) to determine the composition of manganese and cobalt in the materials.

X-ray diffraction patterns of the mixed metal (Mn and Co) oxides were collected in the range of  $10^\circ$  to  $80^\circ$ , see Figure 3.5. The patterns were compared with the reference patterns of  $\text{LiMn}_2\text{O}_4$  [PDF-00-054-0252] and  $\text{LiCoO}_2$  [00-044-0145].

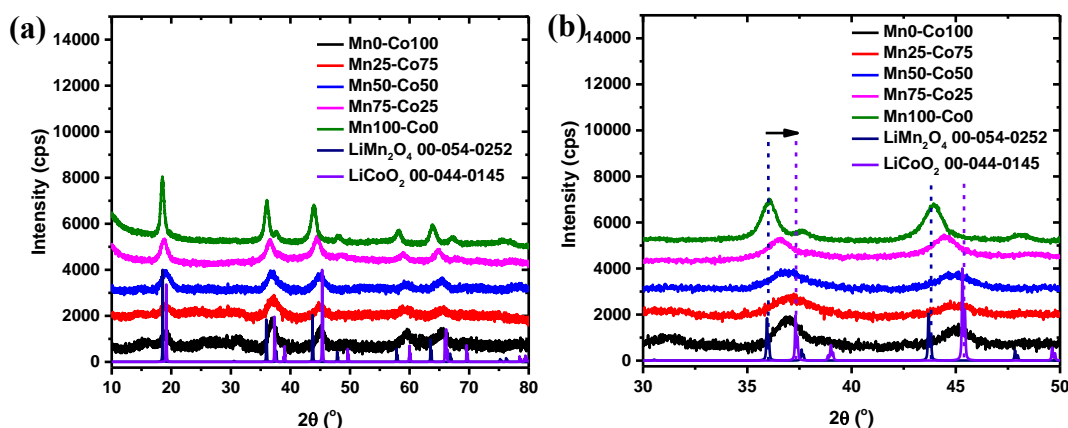


**Figure 3.5.** XRD patterns of  $\text{LiMn}_{2-x}\text{Co}_x\text{O}_4$  (Mn%-Co%) at  $300^\circ\text{C}$  for 1 hour 2000rpm 10s and PDF cards of  $\text{LiMn}_2\text{O}_4$ -00-054-0252 and  $\text{LiCoO}_2$ -00-044-0145.

The diffraction patterns of the mixed oxides change slightly by changing the cobalt and manganese ratios but the patterns, are very similar to each other because these two transition metals are very similar in terms of being in the first row of transition metals and having close atomic size. So, their crystal structures are also close

to each other. These reference XRD patterns have little shifts from each other with same intensity patterns. Figure 3.5 shows the diffraction patterns in the range of  $30^\circ$  and  $50^\circ$ ,  $2\theta$ , and comparison with the corresponding PDF cards. The diffraction lines of  $\text{LiMn}_2\text{O}_4$  are slightly shifted to lower angles compared to  $\text{LiCoO}_2$ . As a result of that, the diffraction lines of the intermediate ratios of cobalt and manganese should be between these diffraction lines of the pure LMOs, proving a solid solution formation in the  $\text{LiMn}_{2-x}\text{Co}_x\text{O}_4$  samples and also from a large broadening in the diffraction lines, it is clear that the nanocrystals are smaller in the mixed oxides.

<b><math>\text{LiMn}_{2-x}\text{Co}_x\text{O}_4</math> 300 °C (Mn%-Co%)</b>	<b>BET Surface Area (<math>\text{m}^2\text{g}^{-1}</math>)</b>	<b>BJH Pore size (nm)</b>	<b>Pore volume (<math>\text{cm}^3\text{g}^{-1}</math>)</b>
<b>Mn100-Co0</b>	<b>98</b>	<b>11.1</b>	<b>0.26</b>
<b>Mn75-Co25</b>	<b>144</b>	<b>6.7</b>	<b>0.27</b>
<b>Mn50-Co50</b>	<b>124</b>	<b>6.6</b>	<b>0.23</b>
<b>Mn25-Co75</b>	<b>103</b>	<b>5.7</b>	<b>0.17</b>

**Table 3.3.**  $\text{N}_2$  adsorption-desorption results of  $\text{LiMn}_{2-x}\text{Co}_x\text{O}_4$  according to Mn%-Co% mole percentages at 300 °C.

The surface area, from the  $\text{N}_2$ -adsorption-desorption measurement of the mixed oxides with an addition of 25 mole percent cobalt into the material, increases from  $98 \text{ m}^2 \text{ g}^{-1}$  to  $144 \text{ m}^2 \text{ g}^{-1}$ , see Table 3.3. Then further increasing cobalt percentage causes decrease in the surface area, but still they have higher surface area compared to pure  $\text{LiMn}_2\text{O}_4$ . Also the pore sizes of the mesoporous mixed oxides drop to around 6 nm with the addition of cobalt. So there is a synergetic interaction between cobalt and manganese salts while forming  $\text{LiMn}_{2-x}\text{Co}_x\text{O}_4$ . The BET surface area can be correlated by the pore size. A large decrease in the pore size is also a proof of an increase in the surface area. So, they are inversely proportional to each other.

The surface area of the  $\text{LiMn}_{2-x}\text{Co}_x\text{O}_4$  can also be correlated by XRD data; the addition of cobalt into LMO cause a further broadening in the diffraction lines. The broadening originates from smaller nanocrystallite size or smaller pore-wall thickness, see Figure 3.5.

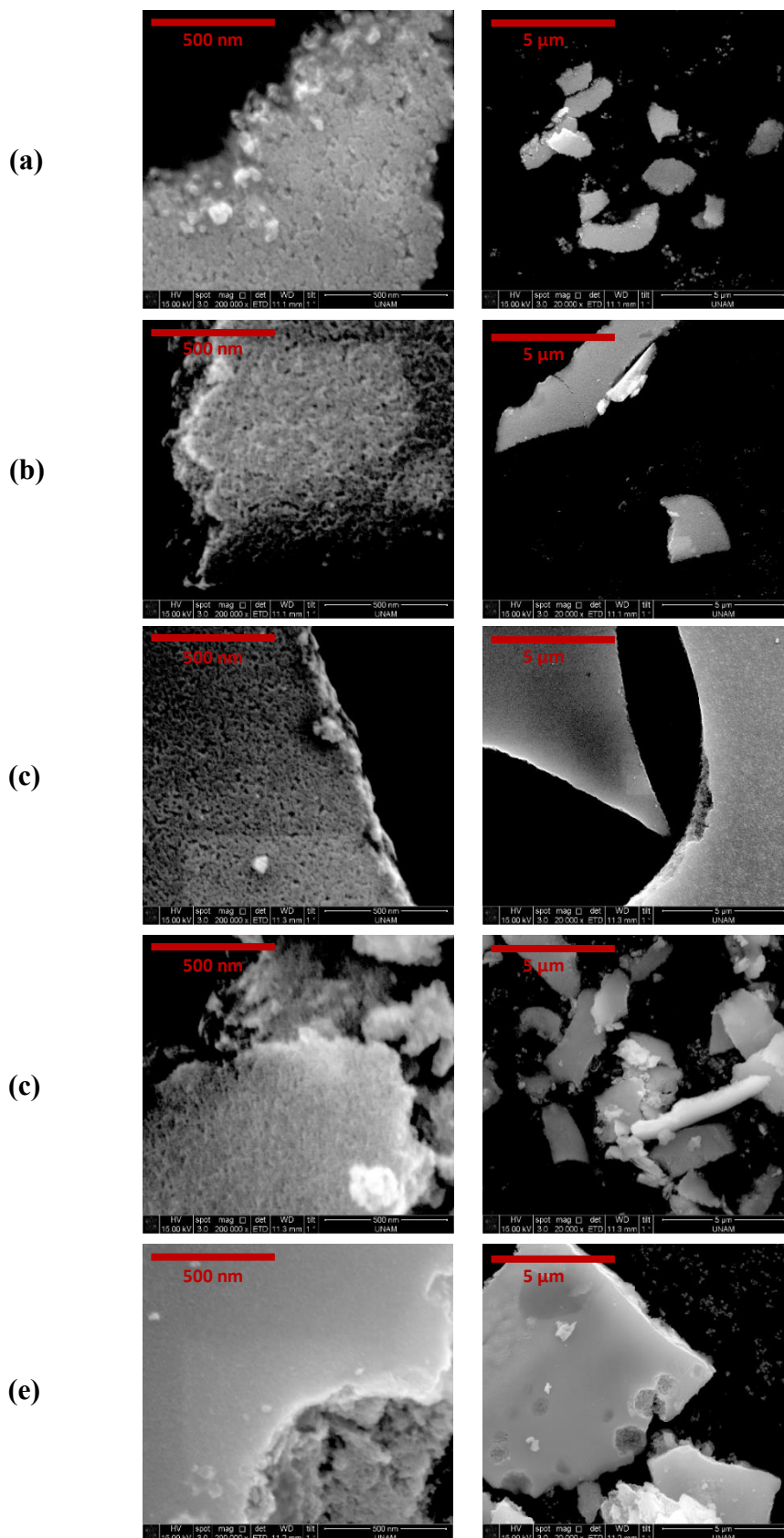


**Figure 3.6.** SEM images of  $\text{LiMn}_{2-x}\text{Co}_x\text{O}_4$  at  $300^\circ\text{C}$  (a) Mn100-Co0 (b) Mn75-Co25 (c) Mn50-Co50 (d) Mn25-Co75 (e) Mn0-Co100

In the SEM images of the mixed  $\text{LiMn}_{2-x}\text{Co}_x\text{O}_4$  (see Figure.3.6), the LMO domains are obvious, consist of 20 nm particles. However, the particles get smaller with the addition of cobalt, and becomes invisible in the SEM images, showing a reduction in the size of crystalline  $\text{LiMn}_{2-x}\text{Co}_x\text{O}_4$  domains in the films. Also at lower magnifications in the microscope, the film pieces are visible and become better (more uniform) with the addition of cobalt into  $\text{LiMn}_{2-x}\text{Co}_x\text{O}_4$ . Better film quality could be due to decrease in the particle size and smaller pores in the materials. So, the SEM images of the  $\text{LiMn}_{2-x}\text{Co}_x\text{O}_4$  materials also correlate the BET surface area and BJH pore sizes.

EDX spectra of the  $\text{LiMn}_{2-x}\text{Co}_x\text{O}_4$  samples were recorded to determine their atomic percentage of each element. Figure 3.7 shows a set of EDX spectra of  $\text{LiMn}_{2-x}\text{Co}_x\text{O}_4$ . Atomic percentages of Co and Mn in the samples were correlated with the initial compositions in the gel phase in terms of manganese and cobalt mole ratios.

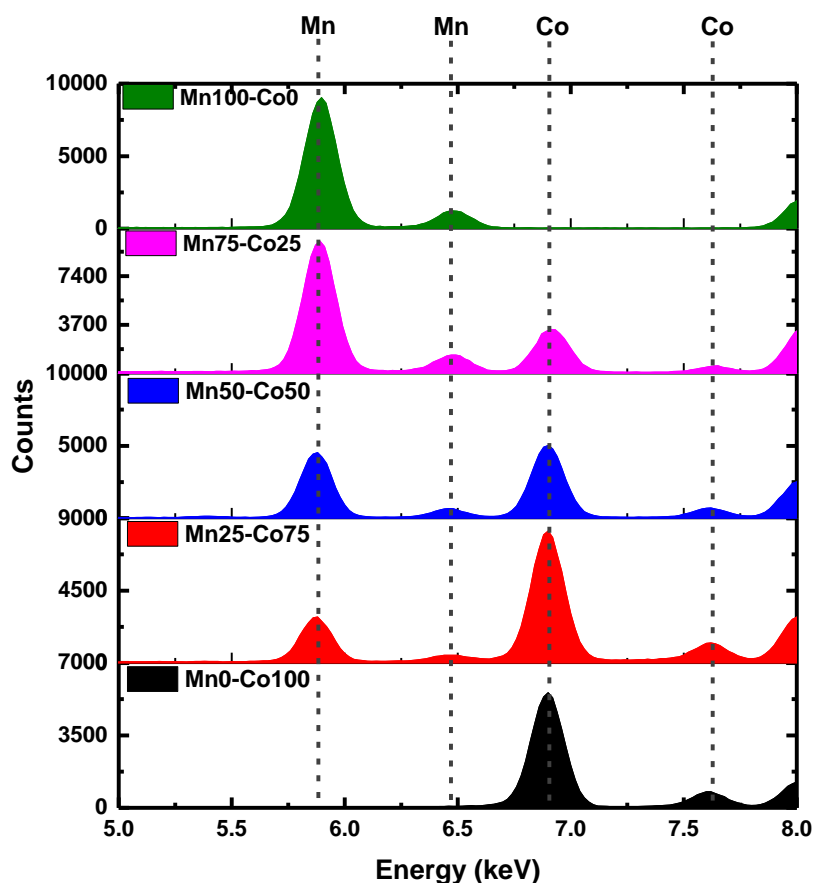


**Figure 3.7.** EDX spectra of  $\text{LiMn}_{2-x}\text{Co}_x\text{O}_4$  (Mn%-Co%) at 300 °C for 1h.

The EDX peaks, due to manganese and cobalt, are observed in the 5-8 keV region. There are two peaks from each element but the peaks at around 6 and 7 keV due to Mn and Co, respectively, were used for the quantitative analysis, because of their high intensity. These two transition metals have a very similar  $K\alpha_1$  peak (slightly different energies with same intensities). So, the counts (intensity) can be used to determine the ratios of each element. With the addition of cobalt into  $\text{LiMn}_2\text{O}_4$ , intensity of the peak at around 7 keV gradually increases with increasing Co in the  $\text{LiMn}_{2-x}\text{Co}_x\text{O}_4$ . Notice also that the  $\text{LiMnCoO}_4$  (Mn50-Co50) sample has equal intensities at these two peaks. Also, the intensity ratio of these two peaks of the other compositions correlates with the atomic ratio of these two elements in their original solutions. Therefore, the EDX spectra can be used to determine the atomic percentage of elements in all compositions. The quantitative data obtained from the EDX spectra are tabulated in Table 3.4.

<b><math>\text{LiMn}_{2-x}\text{Co}_x\text{O}_4</math> 300 °C (synthesized) Mn%-Co% (mole percentage)</b>	<b>Atomic % by quantification Mn</b>	<b>Atomic % by quantification Co</b>
<b>Mn100-Co0</b>	<b>100</b>	<b>0</b>
<b>Mn75-Co25</b>	<b>72.2</b>	<b>27.8</b>
<b>Mn50-Co50</b>	<b>49.7</b>	<b>50.3</b>
<b>Mn25-Co75</b>	<b>23.4</b>	<b>76.6</b>
<b>Mn0-Co100</b>	<b>0</b>	<b>100</b>

**Table 3.4.** Quantity of Mn and Co (in percent) in the  $\text{LiMn}_{2-x}\text{Co}_x\text{O}_4$  (Mn%-Co%) samples.

### 3.3 Electrochemical Measurements of Mesoporous $\text{LiMn}_{2-x}\text{Co}_x\text{O}_4$ Thin Films as Water Oxidation Electrocatalysts

#### 3.3.1 Electrochemical Characterization and Efficiency in Water Oxidation of $\text{LiMn}_{2-x}\text{Co}_x\text{O}_4$ Films

After successful synthesis and characterization of the mesoporous  $\text{LiMn}_2\text{O}_4$  and  $\text{LiMn}_{2-x}\text{Co}_x\text{O}_4$  films, their electrodes were prepared over FTO coated glasses and used in electrochemical measurements to determine their electrochemical characteristics, efficiencies for water oxidation reaction (OER), and stabilities after usage in OER. Cyclic voltammetry (CV), chronoamperometry (CA), and chronopotentiometry (CP) experiments were also performed for the electrochemical characterization of the films.

For all electrodes, the characterization was started by recording a CV. Different regions of the CV curves were used for different purposes, like determination of active surface sites or surface coverage, Tafel slope, and overpotential at an exact current density. The CVs of the  $\text{LiMn}_{2-x}\text{Co}_x\text{O}_4$  electrode (used as working electrodes (WE))

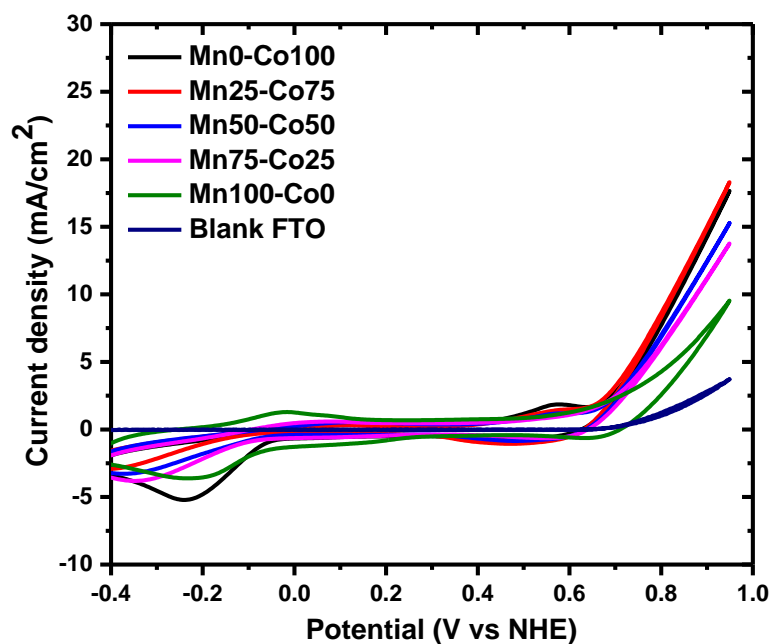


**Figure 3.8.** Cyclic voltammograms of  $\text{LiMn}_{2-x}\text{Co}_x\text{O}_4$  (Mn%-Co%) (calcined at 300°C for 1h) electrode with a scan rate of 50  $\text{mV s}^{-1}$ .

were collected with a  $50 \text{ mV s}^{-1}$  scan rate in the range of  $-0.4$  and  $1 \text{ V}$  vs NHE in  $1 \text{ M}$  KOH alkaline solution, see Figure 3.8.

In the range of  $-0.4$  and  $0.2 \text{ V}$ , the Mn ion species on the WE surface are oxidized (positive current) and reduced (negative current). The cobalt species on the WE surface are oxidized (positive current) and reduced (negative current) at around  $0.5$ - $0.6 \text{ V}$  region. By sweeping the potential over  $0.6 \text{ V}$ , the current density increased in all materials. Above this critical potential value, the oxygen evolution reaction (OER) or water oxidation reaction occurs where the current density ( $j$ ) linearly increases with increasing the applied potential, see Figure 3.8. High current density, up to  $20$  or  $30 \text{ mA cm}^{-2}$  at relatively low over potentials means performance of the electrode is suitable for water oxidation. In other words, if the current density increase is sharp, OER is more efficient. So by inspecting the CV cycles of the  $\text{LiMn}_{2-x}\text{Co}_x\text{O}_4$  materials, the efficient electrodes have cobalt ion species. Their current density increases sharply, indicating that the cobalt in the materials are more active than manganese in the OER process.

The current density, due to oxidation and reduction of transition metal species, provides information about the catalytically active sites of the metal ion species on the electrode surface. If the current density is high, the catalytic active surface or surface coverage, which is in contact with the electrolyte is high and vice versa. The amount of active sites of the metal ion species can also be obtained by a derived equation (see Equation 1.3) from Nernst's equation. To apply the equation in an accurate way, these redox parts are scanned with different scan rates and the surface coverage is obtained for all materials, synthesized in this thesis.

Figure 3.9 shows the CVs of the materials, prepared in all ratios of manganese and cobalt. The CVs were collected in the range of  $-0.2$  to  $0.2 \text{ V}$  for the analysis of Mn ion and  $0.4$  to  $0.7 \text{ V}$  for the Co ion species with scan rates from  $2 \text{ mV s}^{-1}$  to  $20 \text{ mV s}^{-1}$  by an increment of  $2 \text{ mV s}^{-1}$ . So their oxidation peaks were investigated to find active surface species. The change was plotted as function of the scan rate vs current density of the peaks, see Figure 3.10. The peaks maxima were taken as the current density value for further calculations.

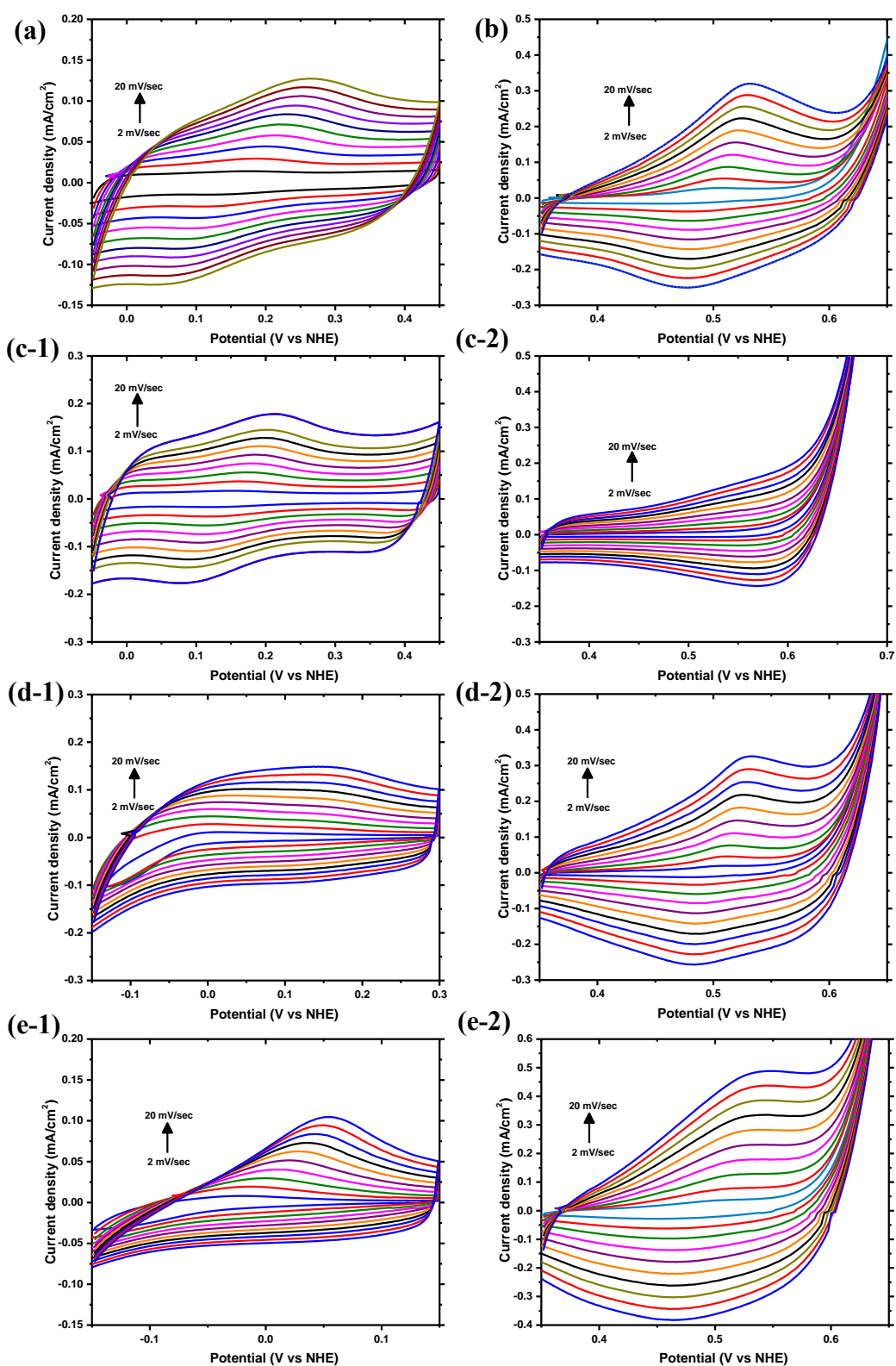


**Figure 3.9.** CVs of the electrodes with scan rates of 2 to 20 mV s<sup>-1</sup> in the range of Mn and Co ions redox potentials; the composition of the electrodes are  
**(a)**Mn100-Co0-(Mn)                      **(b)**Mn0-Co100-(Co)                      **(c-1)**Mn75-Co25-(Mn)  
**(c-2)**Mn75-Co25-(Co)                      **(d-1)** Mn50-Co50-(Mn)                      **(d-2)**Mn50-Co50-(Co)  
**(e-1)** Mn25-Co75-(Mn)                      **(e-2)**Mn25-Co75-(Co)

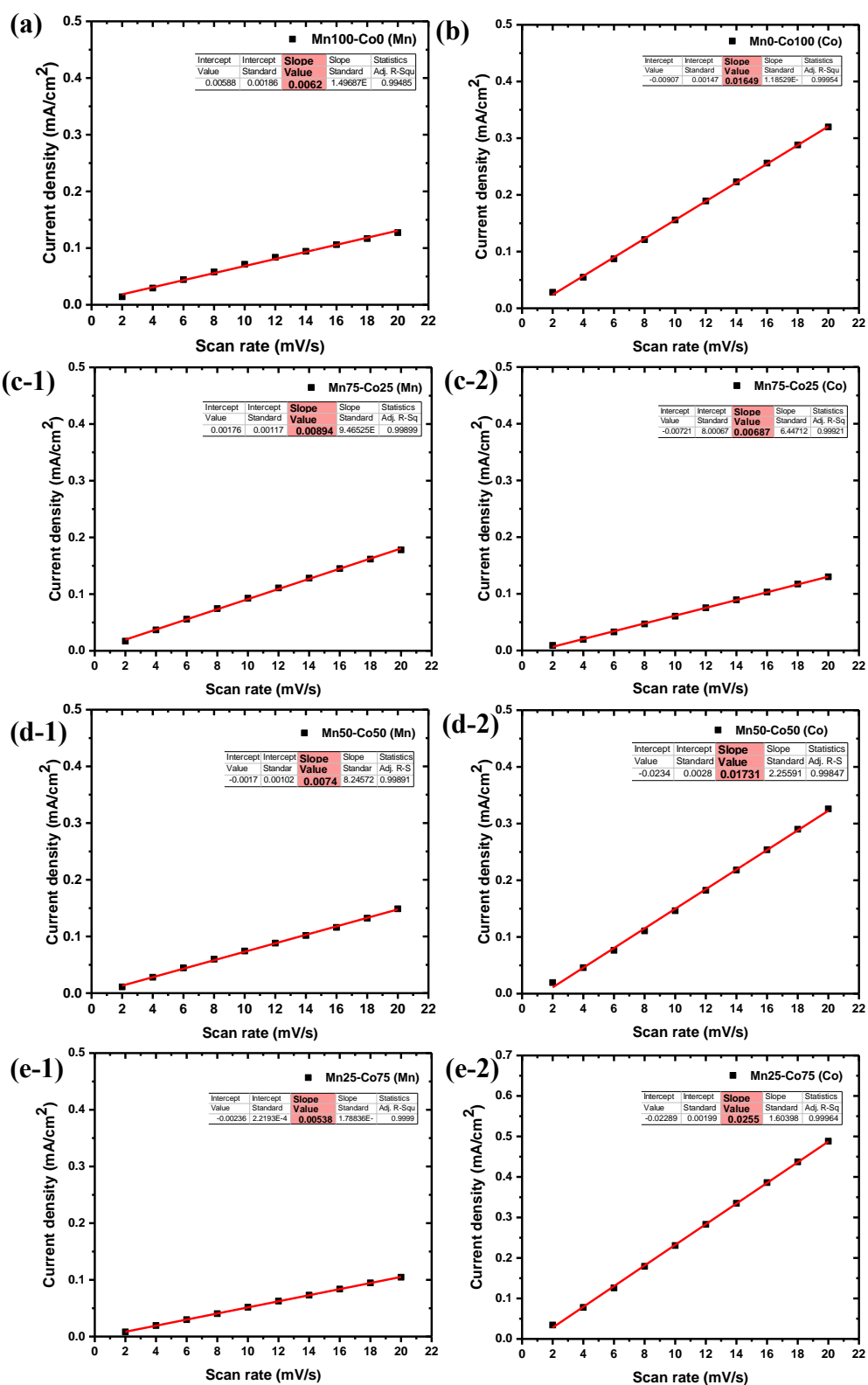


**Figure 3.10.** Current densities of oxidation peaks of Mn and Co with changing scan rates (a)Mn100-Co0-(Mn) (b)Mn0-Co100-(Co) (c-1)Mn75-Co25-(Mn) (c-2)Mn75-Co25-(Co) (d-1) Mn50-Co50-(Mn) (d-2)Mn50-Co50-(Co) (e-1) Mn25-Co75-(Mn) (e-2)Mn25-Co75-(Co)

According to Equation 1.3, the current density of a redox species is linearly dependent on the scan rate. In the case of lower scan rate, the current density is smaller and larger for faster scan rates. Also the current density depends on the active redox species on the WE. Reason for running many cycles with various scan rates is to obtain reliable values and to show linearity between scan rate and current. Deducing a slope from the plot provides a reliable result of the surface concentration. The slopes of the plots and calculated amounts of redox species are tabulated in Table 3.5.

<b>Materials</b> <b>LiMn<sub>2-x</sub>Co<sub>x</sub>O<sub>4</sub> (Mn%-Co%)</b>	<b>Mn ions</b>		<b>Co ions</b>	
	<b>Slope</b>	<b>Surface Coverage</b> nmol cm <sup>-2</sup>	<b>Slope</b>	<b>Surface Coverage</b> nmol cm <sup>-2</sup>
<b>Mn100-Co0</b>	<b>0.00625</b>	<b>6.653</b>	<b>-</b>	<b>-</b>
<b>Mn75-Co25</b>	<b>0.00894</b>	<b>9.517</b>	<b>0.00687</b>	<b>7.313</b>
<b>Mn50-Co50</b>	<b>0.00747</b>	<b>7.952</b>	<b>0.01731</b>	<b>18.427</b>
<b>Mn25-Co75</b>	<b>0.00538</b>	<b>5.227</b>	<b>0.02555</b>	<b>27.146</b>
<b>Mn0-Co100</b>	<b>-</b>	<b>-</b>	<b>0.01649</b>	<b>17.554</b>

**Table 3.5.** Surface concentration of Co and Mn ion species on electrodes of LiMn<sub>2-x</sub>Co<sub>x</sub>O<sub>4</sub> (Mn%-Co%)

The manganese species on the electrode surface don't show huge differences as the amounts of Mn changes; their surface concentration varies between 5 and 10 nmol cm<sup>2</sup> even in the presence of cobalt in the LMOs. However, with the addition of cobalt into materials, the Co active species on the surface increase gradually from Mn100-Co0 to Mn25-Co75. Reason for this observation is due to both cobalt amounts and also an increase in the surface area of the materials with the addition of cobalt. As a result of these two parameters, the LiMn<sub>2-x</sub>Co<sub>x</sub>O<sub>4</sub> materials also have good catalytic performance and mostly cobalt species on surface are more responsible for the OER efficiencies.

According to the CV curves in Figure 3.9, the electrodes show pseudo-capacitor property. So, from the CV curves, collected at a 20 mV s<sup>-1</sup> scan rate, specific capacitance of the WEs were calculated using Equation 1.2 and tabulated in Table 3.6.

$\text{LiMn}_{2-x}\text{Co}_x\text{O}_4$ Mn%-Co%	Catalytic load (mg)	$C_s$ (Mn) ( $\text{F g}^{-1}$ )	$C_s$ (Co) ( $\text{F g}^{-1}$ )
Mn100-Co0	90	44	-
Mn75-Co25	150	42	37
Mn50-Co50	130	37	72
Mn25-Co75	140	16	98
Mn0-Co100	90	-	101

**Table 3.6.** Specific capacitance values of  $\text{LiMn}_{2-x}\text{Co}_x\text{O}_4$  by CVs in redox potential ranges of manganese and cobalt species with a scan rate of  $20 \text{ mV s}^{-1}$ .

According to the  $C_s$  of the LMOs, they show same trend with surface coverage results by increasing cobalt species in the  $\text{LiMn}_2\text{O}_4$ . However, pseudo-capacitance properties are small compared to a good working capacitor

In addition to cyclic voltammetry of  $\text{LiMn}_{2-x}\text{Co}_x\text{O}_4$ , Tafel slopes for OER were evaluated to obtain a detailed information about the efficiencies of all the electrodes. This analysis was done by employing a chronoamperometry (CA) measurement. Very early potential value, before OER is determined as starting point for applying potential and then the applied voltage was increased with an increment of 20 mV. Each potential was applied for 10 minutes and the current densities at each potential were collected. According to the Tafel, the logarithm of current density ( $j$ ) is linearly proportional to

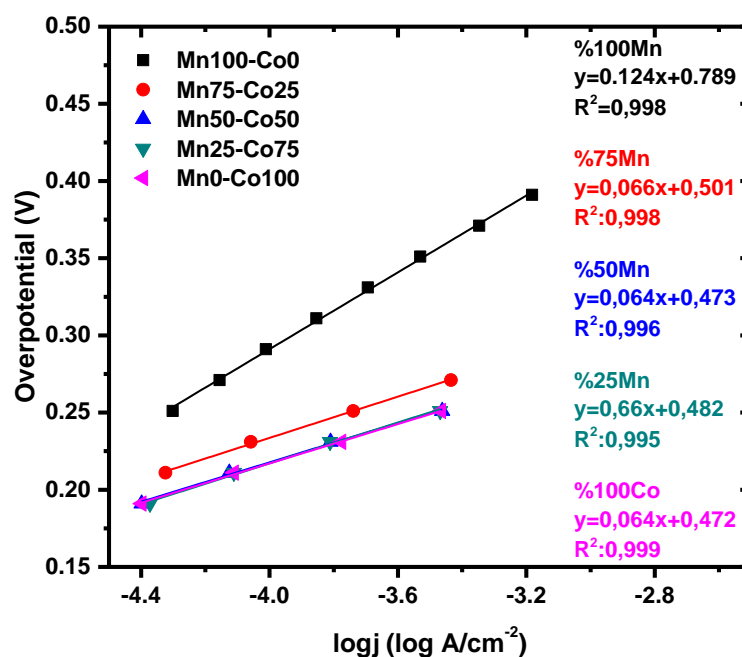


**Figure 3.11.** Tafel plots and equations of  $\text{LiMn}_{2-x}\text{Co}_x\text{O}_4$  (Mn%-Co%).

the applied potential. Therefore, the overpotentials ( $\eta$ ) vs logarithm of the current density,  $\log(j)$ , were plotted to obtain the Tafel slopes, see Figure 3.11.

If the current density sharply increases in the CVs starting from the water oxidation potential, the electrode has a good catalytic property in OER. From the Tafel equation, a series of plots is constructed by overpotential vs  $\log(j)$ . According to the equation, if the current density is huge at a given potential, then the slope must be low and vice versa if the current density is low. Therefore, for a good efficiency, the Tafel slope should be low. These slopes can be reported as Tafel slope of the electrode. Increase in the current density in the OER potential range in the CV curves could be correlated by cobalt amount added and also the results can be correlated to Tafel slopes. This is because, adding cobalt into  $\text{LiMn}_2\text{O}_4$  decreases Tafel slope from  $124 \text{ mV dec}^{-1}$  to around  $66 \text{ mV dec}^{-1}$ , indicating the cobalt effect on the OER process. However, addition of more cobalt doesn't help to improve Tafel slope for the OER. Simply, even 25% cobalt in the sample does the same work for producing oxygen.

An overpotential required for the OER at common current densities (like a  $1 \text{ mA cm}^{-2}$  and  $10 \text{ mA cm}^{-2}$ ) were also extracted from the Tafel equations for each composition and tabulated in Table 3.7.

$\text{LiMn}_{2-x}\text{Co}_x\text{O}_4$ <i>Mn%-Co%</i>	Tafel Slope ( $\text{mV dec}^{-1}$ )	$\eta$ at 1mA (mV)	$\eta$ at 10mA (mV)
<b>Mn100-Co0</b>	<b>124</b>	<b>417</b>	<b>541</b>
<b>Mn75-Co25</b>	<b>66</b>	<b>300</b>	<b>367</b>
<b>Mn50-Co50</b>	<b>64</b>	<b>281</b>	<b>345</b>
<b>Mn25-Co75</b>	<b>66</b>	<b>284</b>	<b>350</b>
<b>Mn0-Co100</b>	<b>64</b>	<b>280</b>	<b>344</b>

**Table 3.7.** Tafel slopes, overpotential ( $\eta$ ) at  $1 \text{ mA cm}^{-2}$  and  $10 \text{ mA cm}^{-2}$  by calculation from the Tafel equations of the  $\text{LiMn}_{2-x}\text{Co}_x\text{O}_4$  (Mn%-Co%) electrodes.

The overpotential, obtained from the Tafel equations of the pure  $\text{LiMn}_2\text{O}_4$  is much higher than the other compositions. It also means that  $\text{LiMn}_2\text{O}_4$  requires higher potential or energy for the OER. With the addition of 25% cobalt into the oxides, the potential required for the oxygen evolution decreases to 300 mV and at the higher cobalt amounts, the potential can decrease down to 280 mV. These values also correlate with the Tafel slopes. For a  $10 \text{ mA cm}^{-2}$  current density, a higher overpotential is required. Inherently, the higher current values require higher energies.

The overpotentials required for the pure Mn100-Co0 sample is 541 mV at 10 mA cm<sup>-2</sup>. However, addition of cobalt decreases this potential value down to 344 mV. From the Tafel slopes and the other analysis, we found that addition of cobalt to LMOs increases the efficiency and therefore, those electrodes require less energies for the OER process.

The same electrodes were further used for the chronopotentiometry (CP) measurements to obtain overpotential results at 1 mA cm<sup>-2</sup> and high current densities. The current density was fixed to 1 mA cm<sup>-2</sup> and the potential was applied for 3 hours on each electrode, see Figure 3.12.

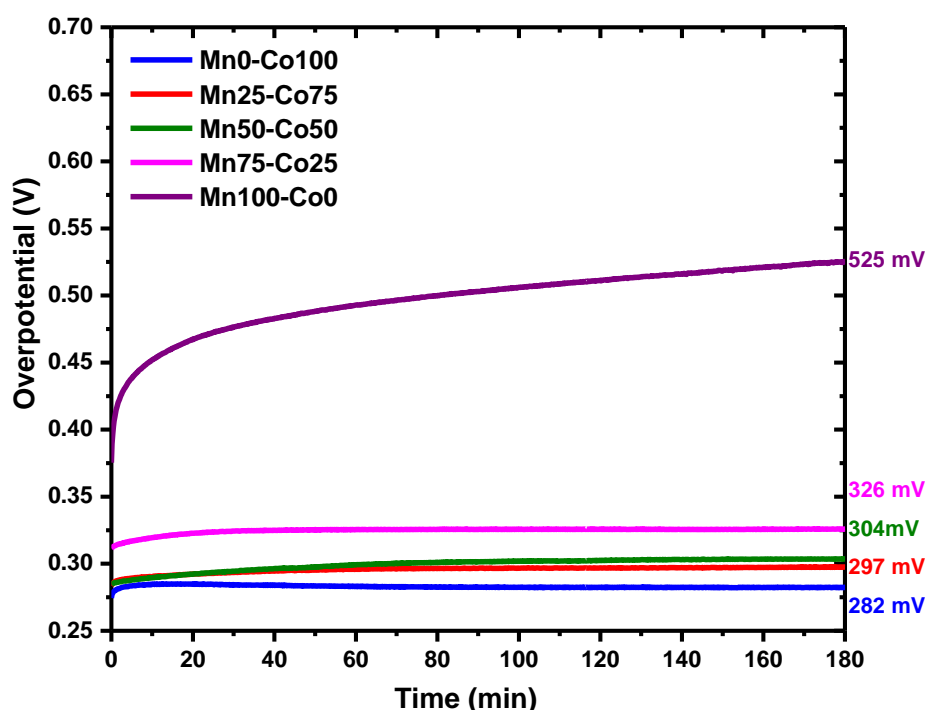


**Figure 3.12.** Chronopotentiometry results of the  $\text{LiMn}_{2-x}\text{Co}_x\text{O}_4$  (Mn%-Co%) electrode at current density 1 mA cm<sup>-2</sup> for 3 hours.

The CP experiments, performed at 1 mA cm<sup>-2</sup>, show that the required potentials for OER is similar to the extracted voltage from the Tafel equation. In the pure  $\text{LiMn}_2\text{O}_4$ , the potential started at around 400 mV but during the experiment, it gradually increased up to 525 mV. The reason for this increase is attributed to an electrode decomposition under our reaction conditions. The electrode loses its efficiency due to low stability, material lost during usage, and therefore the required

energy for OER increases. By adding cobalt into  $\text{LiMn}_2\text{O}_4$  enhances the electrode stability in the electrolyte solution, as a result it also brings stability in the overpotentials, see Figure 3.12. Notice that there is no big potential difference between the beginning and end of the CP experiment in the  $\text{LiMn}_{2-x}\text{Co}_x\text{O}_4$  electrodes. Also the electrodes with cobalt have lower overpotentials at  $1 \text{ mA cm}^{-2}$ , also showing the effect of cobalt for OER. Therefore, addition of cobalt into  $\text{LiMn}_{2-x}\text{Co}_x\text{O}_4$  also brings stability on the electrodes for the electrochemical measurements and usage in the alkali medium.

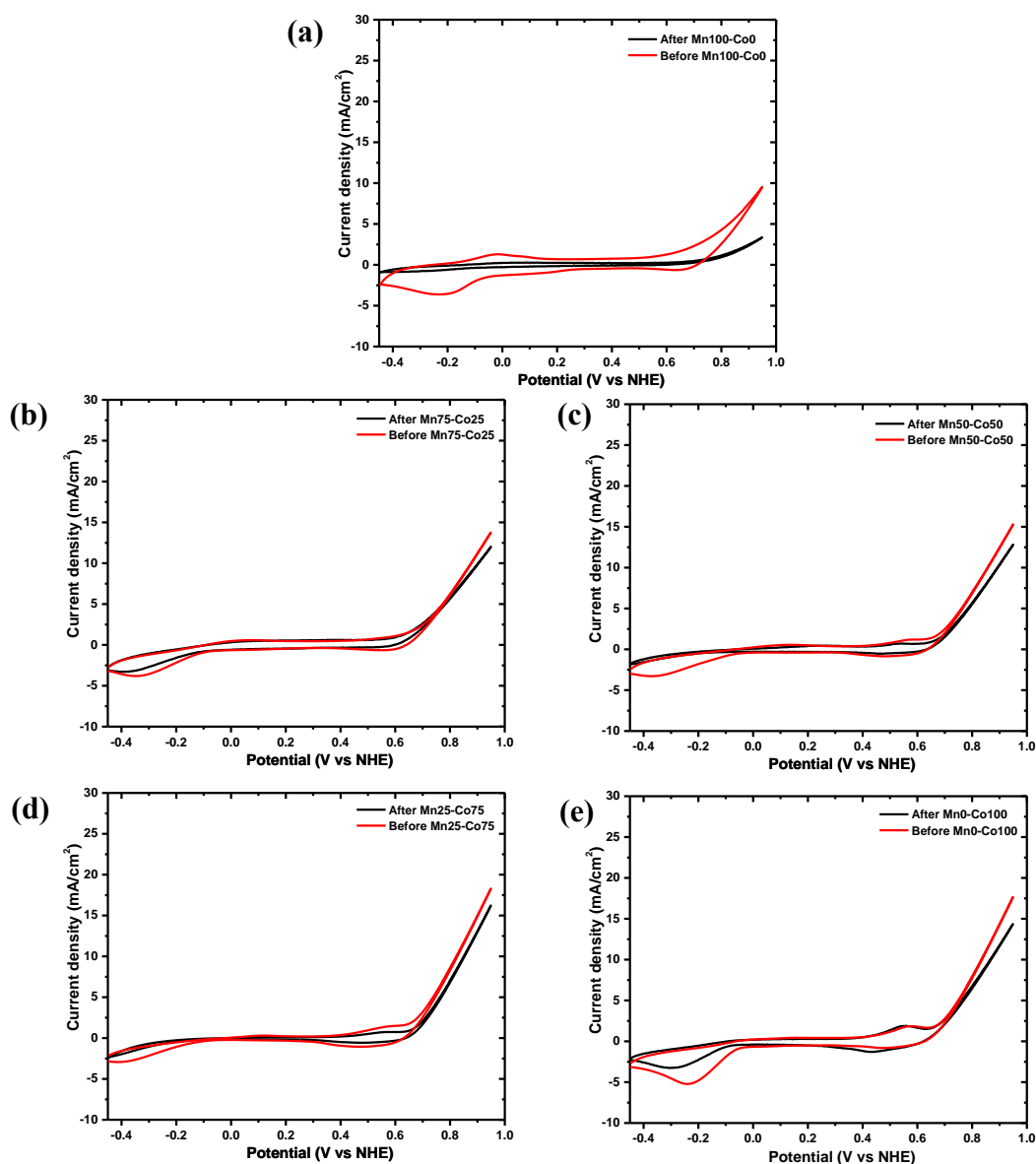


**Figure 3.13.** Cyclic Voltammograms of  $\text{LiMn}_{2-x}\text{Co}_x\text{O}_4$  (Mn%-Co%) before (1<sup>st</sup> CV) after (CV after CP at  $1 \text{ mA cm}^{-2}$ ) (a) Mn100-Co0 (b) Mn75-Co25 (c) Mn50-Co50 (d) Mn25-Co75 (e) Mn0-Co100

After 3 hrs of CP experiment, the stability of the electrodes were checked by recording CV again. Figure 3.13 shows the first (before) and last (after CP at  $1 \text{ mA cm}^{-2}$ ) CV cycles of the electrodes. The last cycles were compared with the first cycles of the same electrodes to investigate whether there is a change in current density. So, this provides information about electrode resistance for electrochemical measurements. The CV of the electrodes, after CP at  $1 \text{ mA cm}^{-2}$ , show little differences. Especially the electrodes that include cobalt inside, there are minor changes in current density in the OER region of the CVs, see Figures 3.13 (b)-(e). This means that the electrodes are quite stable when they are used at  $1 \text{ mA cm}^{-2}$  current density at OER for 3 hours. However, there is a drastic change between the first and last cycles in the pure  $\text{LiMn}_2\text{O}_4$  electrode.

### **3.3.2 Advanced Electrochemical Measurements on $\text{LiMnCoO}_4$ Working Electrode**

The electrochemical analysis of the  $\text{LiMn}_{2-x}\text{Co}_x\text{O}_4$  electrodes gives information about the surface coverage of Co and Mn ions species, catalytic efficiencies by Tafel equation, and performance in CP experiments at  $1 \text{ mA cm}^{-2}$ . One electrode with a composition of  $\text{LiMnCoO}_4$  (Mn50-Co50) was chosen for a detailed investigation on the performance for OER. The purpose of this investigation is to search for an efficient and stable electrode with a higher amount of Mn. The cobalt is definitely active than manganese but it is also more toxic and not abundant. So, the  $\text{LiMnCoO}_4$  was approved to be stable for tough experiments, like CP at  $1 \text{ mA cm}^{-2}$  for 18hrs, and higher current applications, from 10 to  $120 \text{ mA cm}^{-2}$ . The CP results of  $\text{LiMnCoO}_4$  are shown in Figure 3.14. The electrode stability was checked after all these experiments by recording their CVs after those experiments.

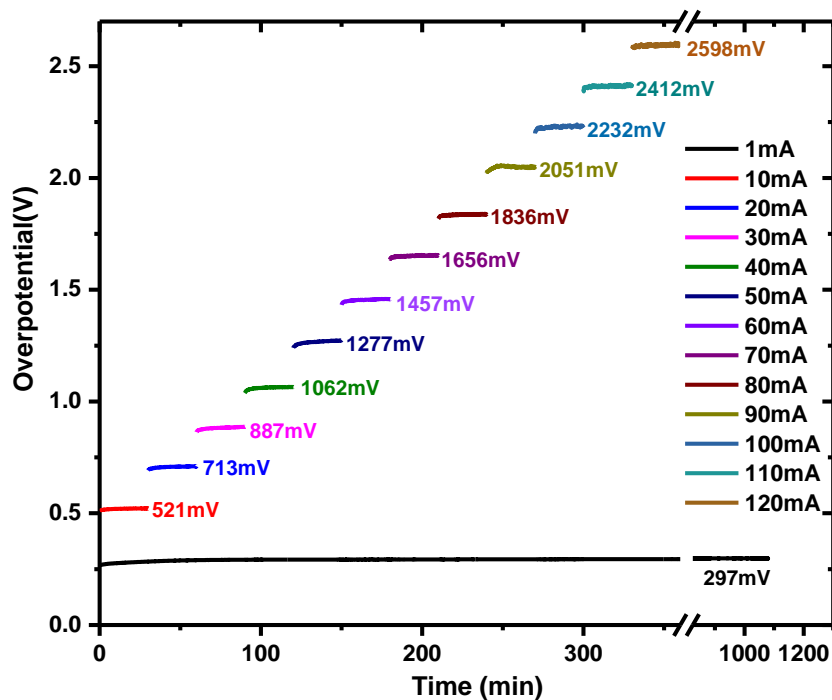


**Figure 3.14.** Chronopotentiometry results of LiMnCoO<sub>4</sub> WE at 1 mA cm<sup>-2</sup> for 18hrs (black line) and at 10 to 120 mA cm<sup>-2</sup> for 30 mins at each (colored lines) potentials.

Current density was fixed to 1 mA cm<sup>-2</sup> for 18 hrs and the overpotential data was recorded in long term. So it shows stable overpotential value of around 300 mV during 18 hrs of CP operation, and there is not much change in the potential during the experiment. It means that the electrode has a good stability in long term experiment at 1 mA cm<sup>-2</sup> and it doesn't lose its efficiency in the OER process. Also the same electrode was exposed to higher current densities of from 10 to 120 mA cm<sup>-2</sup> by increasing the current density incrementally for 30 mins. Collected overpotentials at higher current densities show that there is a linearity between the potential and current and this linearity is preserved even if the fixed current density is above 100 mA cm<sup>-2</sup>. This also show that the electrode is highly stable and robust in tough conditions. The linearity between the fixed current density and overpotential is shown in Figure 3.15 (a). Also the first CV of the LiMnCoO<sub>4</sub> and CV curve after CP at 120 mA cm<sup>-2</sup> is shown in part (b).

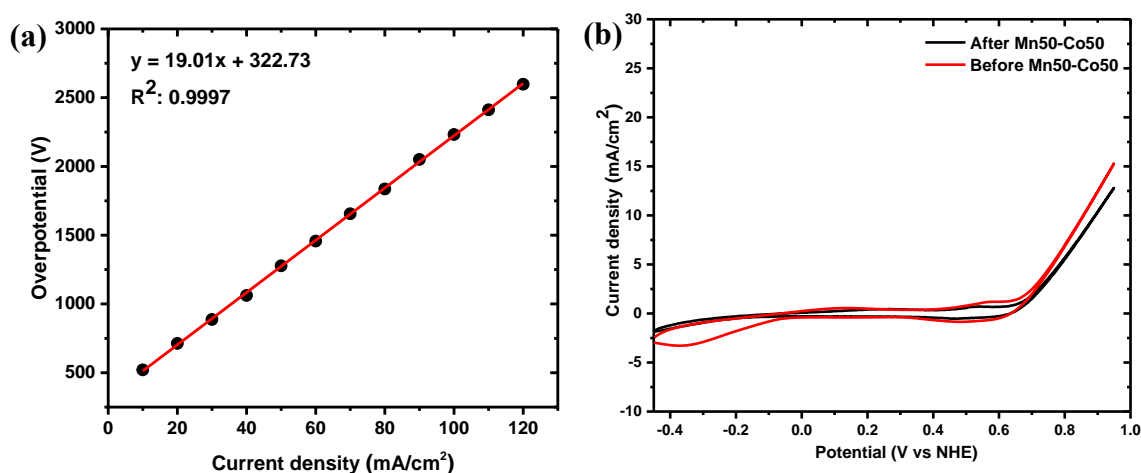


**Figure 3.15.** (a) Current density vs overpotential and linear fit (b) First CV and CV after CP at  $120 \text{ mA cm}^{-2}$  of  $\text{LiMnCoO}_4$  WE

In Figure 3.15 (a) potential vs current is linearly proportional, because  $R^2$  of linear fit is very close to 1, consequently, it shows there is no extra energy used for OER for each current value. Also, the slope of the fit gives the series resistance ( $R_s$ ) between the RE and WE because resistance can be derived from Ohm's law by a ratio of potential to current.  $R_s$  is approximately 19 ohms and it is roughly equal to the FTO resistance that is used as a substrate. So by increasing the fixed current on the WE, the extra energy loss is from the FTO or  $R_s$ . Also in part (b) of Figure 3.15, the first CV curve of the electrode and CV after CP at  $120 \text{ mA cm}^{-2}$  are depicted. After applying high current density on the electrode, the change on OER current is not much, the loss is very small and the electrode shows a similar performance after such harsh use. Therefore, it is correct to say that the  $\text{LiMnCoO}_4$  electrode has a good stability after long term and tough experiment conditions.

### 3.3.3 Coating $\text{LiMnCoO}_4$ on Graphite Substrate and OER Efficiency

Up to this part,  $\text{LiMn}_{2-x}\text{Co}_x\text{O}_4$  materials were coated on FTO surface and it is known that FTO ( $2 \times 1 \text{ cm}$ ) has around 15 to 20 ohm resistivity. So, the resistance value of FTO requires extra potential to run the current during CP measurements. Maybe, this is small at low current densities but become very important at current densities. For instance, increasing the current density to  $10 \text{ mA cm}^{-2}$ , the overpotential value increases extra as much as resistance time current. It means we need to apply extra

0.15-0.20 V at 10 mA cm<sup>-2</sup> current density and 1.5 to 2.0 V at 100 mA cm<sup>-2</sup> current density. Therefore, the substrate that is less resistive than FTO should be used to the analysis of the effect substrate on overpotential values for OER. To do that graphite rod was used and 1 cm<sup>2</sup> of surface of graphite was coated with LiMnCoO<sub>4</sub> precursors and calcined at 300 °C for 1h.

The LiMnCoO<sub>4</sub> coated graphite electrode was used in electrochemical measurements to observe the effect on OER and the curves obtained by the experiments were compared with the electrode of LiMnCoO<sub>4</sub> on FTO. The CVs of LiMnCoO<sub>4</sub> on two substrates are shown in Figure 3.16.

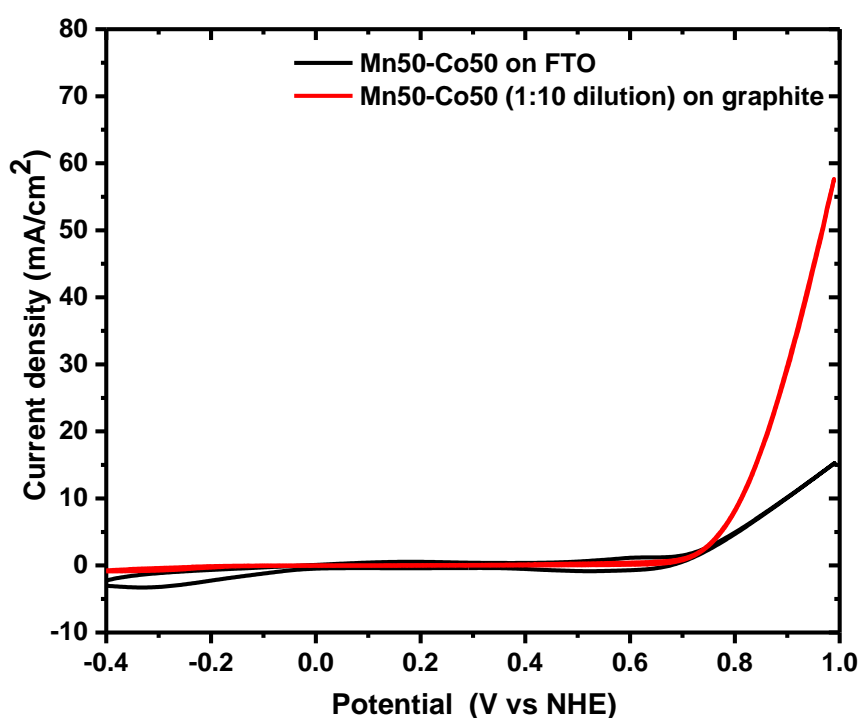


**Figure 3.16.** Cyclic voltammograms of Mn50-Co50 on FTO and graphite substrates

According to the CV curves of two WEs, current density increase in OER for graphite substrate is much larger than the FTO one. This is because, as expected graphite has lower resistivity compared to FTO. Sweeping the potential in the range of water oxidation, the current density goes up with a sharp slope in FTO case compared to graphite, compare CVs in Figure 3.16. This effect was also investigated by chronopotentiometry measurement. The CP results of both electrodes of Mn50-Co50 are shown in Figure 3.17. The trend is drastic, such that the over potential drops

from 1.277 V to 0.523 V at 60 mA cm<sup>-2</sup> current density by simply switching the substrate from FTO to graphite.

The electrode over graphite shows a much lower slope on the overpotential versus current density plot, indicating a much smaller resistance between the WE and RE. The slope of overpotential vs current density (see inset in Figure 3.17(b)) plot is only 3.7 ohm. However, the same resistance in the FTO was found to be around 19 ohm. Therefore, the high conductivity of graphite proven to be a better substrate for high current density applications.

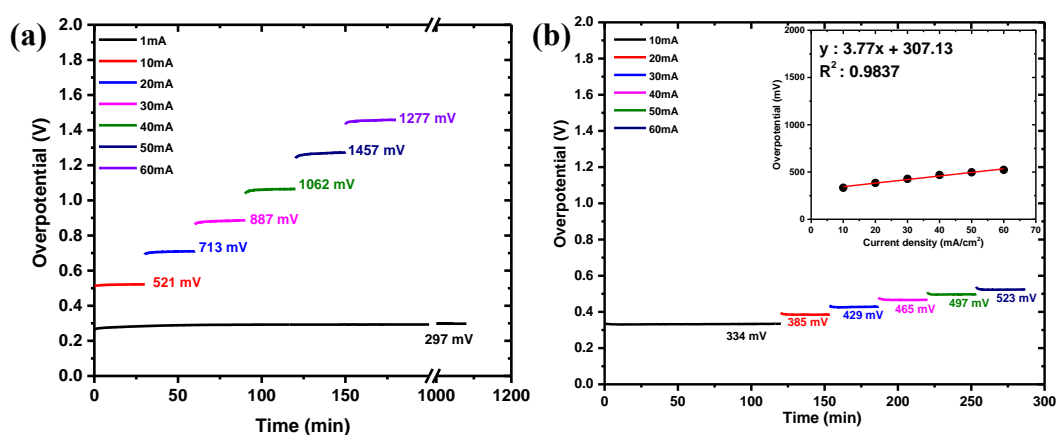


**Figure 3.17.** Chronopotentiometry results at 10 mA cm<sup>-2</sup> to 60 mA cm<sup>-2</sup> with the increments of 10 mA cm<sup>-2</sup> for 30 mins (a) LiMnCoO<sub>4</sub> on FTO (b) LiMnCoO<sub>4</sub> on graphite.

Besides the conductivity advantage of graphite, there are also some disadvantages to use graphite as a substrate. It is difficult to control the thickness and amount of LMO by dip-coating the rods. Coating may produce non-uniform thickness in the LLC phase and LMOs. Moreover, the dip-coating method is usually employed to prepare thicker films. Polymeric materials in pencil tips (pressed graphite) produce carbon species that may contaminate the LMOs. However, this may also be an advantage, because it may enhance the conductivity of LiMnCoO<sub>4</sub>.

### 3.4 Modification of Electrodes by Dipping into Cobalt Nitrate Solution & Formation of Active Thin Layer on Electrode Surface

It has been established in the previous sections that cobalt has higher activity than manganese in OER process and also it provides stability to the electrodes. In this section, the aim is to coat a very thin cobalt oxide layer (see Figure 3.18 (a)) or to diffuse cobalt ions into very top layers of the films to form  $\text{LiMn}_{2-x}\text{Co}_x\text{O}_4$  on surface (see Figure 3.18(b)). The process is inspired by SILAR technique.

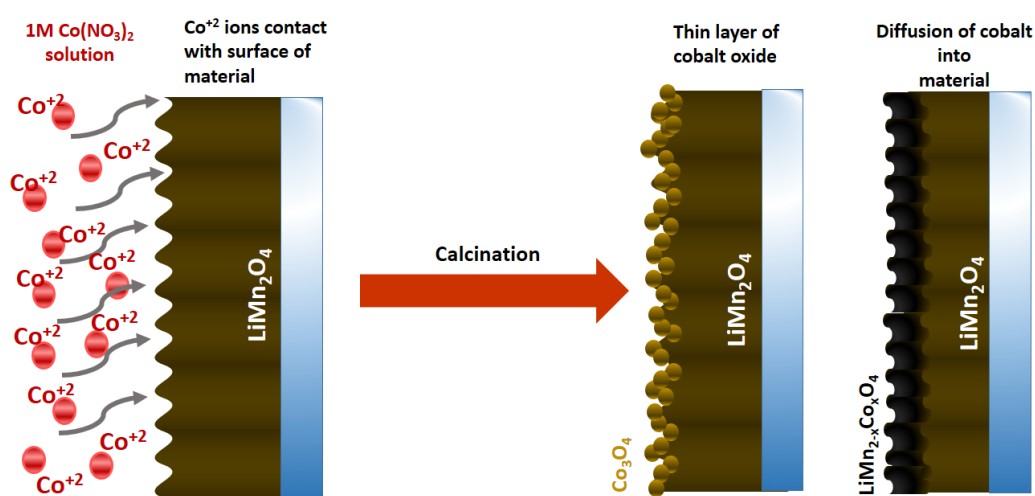


**Figure 3.18.** Schematic representation of dipping method in 1 M cobalt solution of  $\text{LiMn}_2\text{O}_4$  substrates; (a) coating of thin layer of cobalt oxide (b) diffusion of cobalt to form  $\text{LiMn}_{2-x}\text{Co}_x\text{O}_4$  on WE surface.

To establish this method, the pure (Mn100-Co0)  $\text{LiMn}_2\text{O}_4$  was used for dipping processes and the resulting samples were analyzed at various stages of the preparation using the same characterization techniques. The cobalt modified electrodes have been used in the OER process in the same electrochemical processes to determine the activities and stability after modification.

#### 3.4.1 Characterization of Modified Electrodes by Dipping into Cobalt Solution

The  $\text{LiMn}_2\text{O}_4$  electrodes were dipped into  $1\text{M} [\text{Co}(\text{H}_2\text{O})_6](\text{NO}_3)_2$  solution and then the electrodes were washed after each dipping to prevent any cobalt salt deposition in and out of electrodes. So, the dipping process has been applied several

times to coat thicker active layer to enhance the catalytic efficiency of the electrodes. The modified electrode was characterized using XRD technique. The collected diffraction patterns were compared with the diffraction pattern of pure  $\text{LiMn}_2\text{O}_4$ . Also, the XRD patterns were compared with the PDF cards of  $\text{LiCoO}_2$  and cobalt oxide,  $\text{Co}_3\text{O}_4$  to determine whether the cobalt ions diffuse into material or it forms a thin layer of cobalt oxide over the pore-walls. The XRD patterns of the dipped materials are shown in Figure 3.19.

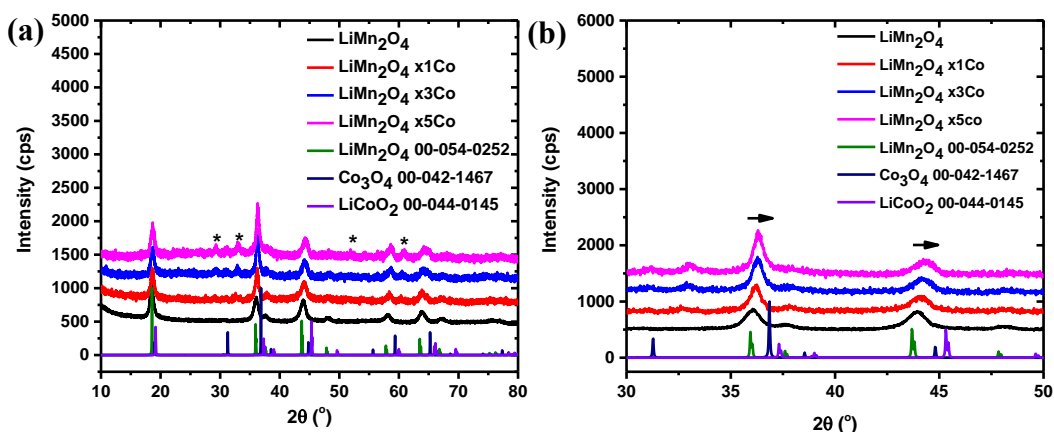


**Figure 3.19.** XRD patterns of  $\text{LiMn}_2\text{O}_4$  and  $\text{LiMn}_2\text{O}_4$  modified by dipping into cobalt solution (a)  $10\text{-}80^\circ$  (b)  $30\text{-}50^\circ$  - (\*)  $\text{Mn}_3\text{O}_4$

The XRD patterns of  $\text{LiMn}_2\text{O}_4$  and their modified forms show similar patterns with some shifts to higher angles on the diffraction lines. So, this shift in the patterns can be concluded as cobalt has some effect in the structure of  $\text{LiMn}_2\text{O}_4$  by diffusion or pore-surface coating. To understand and show in which way cobalt reacts with the material, the patterns were compared with the PDF cards ( $\text{Co}_3\text{O}_4$ , PDF 00-042-1467 and  $\text{LiCoO}_2$ , PDF 00-044-0145) of possible products. However, both patterns of  $\text{Co}_3\text{O}_4$  and  $\text{LiCoO}_2$  references are very similar in terms of diffraction angles. So, by the shift in the signals may not provide an answer for the location of Co species, see Figure 3.19 (b). However, multiple coatings and calcination, the lines corresponding to  $\text{Mn}_3\text{O}_4$  appeared and amplified in intensity (compared with the PDF-00-024-0734 of  $\text{Mn}_3\text{O}_4$ ). This means that cobalt ions over the pore-wall surface diffuse into the  $\text{LiMn}_2\text{O}_4$  pore-walls and undergo exchange with manganese ions. As a result of that, the manganese species diffuse out to the surface and form its own oxides, such as  $\text{Mn}_3\text{O}_4$ .

X-ray photoelectron spectroscopy (XPS) has been employed to determine the surface composition of the dipped electrodes. The XPS spectra of  $\text{LiMn}_2\text{O}_4$ ,  $\text{LiMn}_{1.5}\text{Co}_{0.5}\text{O}_4$ , and modified electrodes by dipping 1-, 3- and 5- times in cobalt nitrate solution are shown in Figure 3.20.

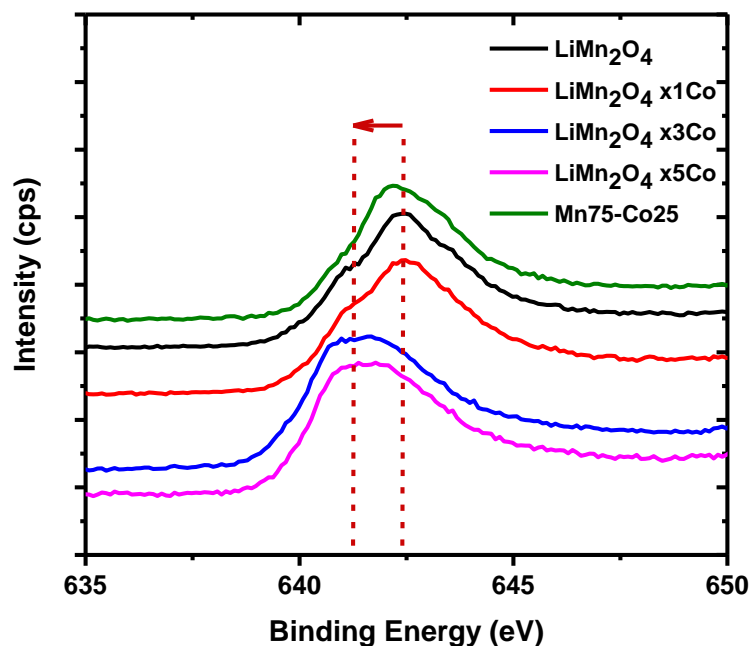


**Figure 3.20.** XPS Mn ( $^2\text{P}_{3/2}$ ) spectra of Mn75-Co25,  $\text{LiMn}_2\text{O}_4$  (Mn100-Co0) and modified WEs.

According to XPS data of these samples, pure  $\text{LiMn}_2\text{O}_4$  has  $\text{Mn}^{3+}$  and  $\text{Mn}^{4+}$  species. The spectrum in the  $^2\text{P}_{3/2}$  region consist of a shoulder on the low energy side and a peak at 643 eV. Also, the spectrum of  $\text{LiMn}_{1.5}\text{Co}_{0.5}\text{O}_4$  is very similar with a very small shift to lower energy. With increasing the number of dipping  $\text{LiMn}_2\text{O}_4$  into cobalt solution and calcination gradually shifts the  $^2\text{P}_{3/2}$  peak to lower energy, showing that the manganese oxidation state goes down.[119] This observation correlates with the XRD data that the Mn is 2+ and 3+ oxidation in  $\text{Mn}_3\text{O}_4$  and showing the formation of  $\text{Mn}_3\text{O}_4$  on the surface of the electrodes. Both XPS and XRD data proves the diffusion of cobalt species into LMO by modification. The XPS spectra of the modified electrodes were also compared with the spectra of  $\text{Mn}_3\text{O}_4$  and  $\text{Mn}_2\text{O}_3$ , see Figure 3.21.

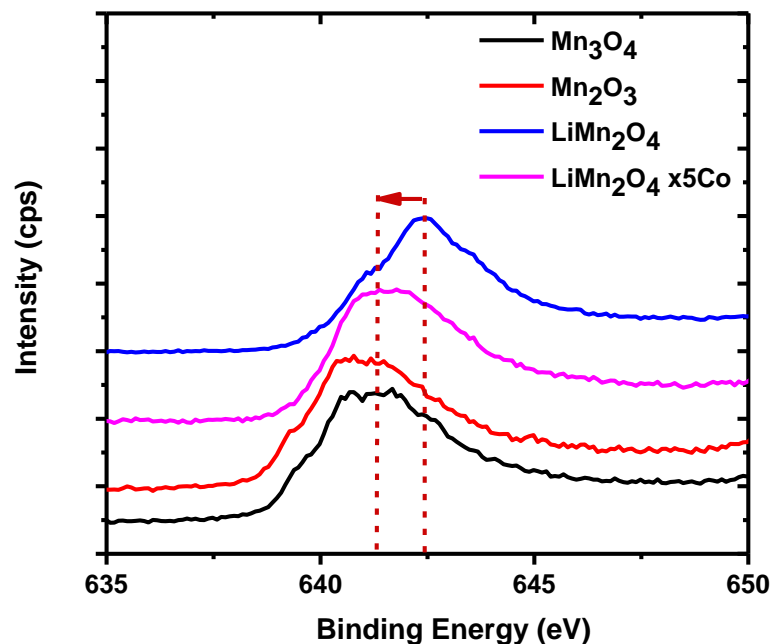


**Figure 3.21.** XPS Mn ( $2P_{3/2}$ ) spectra of  $Mn_3O_4$ ,  $Mn_2O_3$ ,  $LiMn_2O_4$  (Mn100-Co0) and modified with 5-times dipping.

The oxidation state of manganese in  $Mn_3O_4$  is 2+ and 3+ and 3+ in  $Mn_2O_3$ . Because of that their binding energies are shifted to lower energies compared to  $LiMn_2O_4$ , where the oxidation state of Mn is 3+ and 4+.[119] Notice that the XPS spectrum of 5-times dipped electrode is very similar to the  $Mn_3O_4$  spectrum. So, XPS data also prove that the surface is covered by  $Mn_3O_4$  nanocrystallites as evidenced by the XRD data. Moreover, the materials modified by dipping were also analyzed by SEM imaging to identify if there are any morphological changes on the films. The SEM images are shown in Figure 3.22.

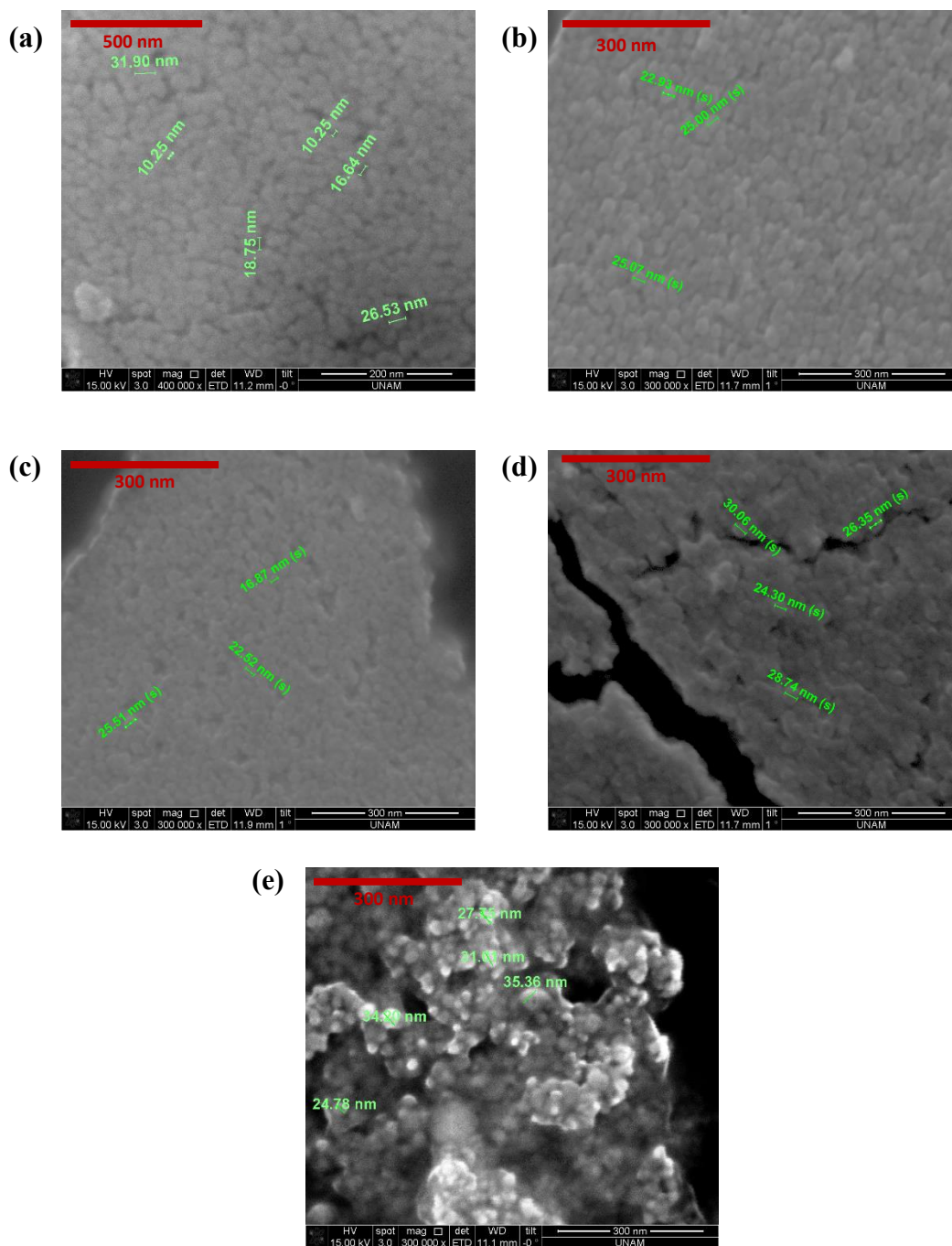


**Figure 3.22.** SEM images of  $\text{LiMn}_2\text{O}_4$  modified electrodes by dipping method (a)  $\text{LiMn}_2\text{O}_4$  without dipping (b) 1-time dipping (c) 3-times dipping (d) 5-times dipping (e) 7-times dipping.

The SEM images of the materials modified by dipping show that the morphology is preserved even in the 5-times dipped samples. However, the film morphology is slightly lost in the case of 7-times dipped sample. The only change in the materials after modification is the particle/domain size. The resolution of SEM is

not sufficient to clearly evaluate the particle size from the images. However, it is certain that some particles in the materials (see Figure 3.22) are on average smaller in the pure  $\text{LiMn}_2\text{O}_4$ , and after dipping modification of the material, average particle sizes increased, compared images in Figure 3.22. Therefore, the cobalt addition to  $\text{LiMn}_2\text{O}_4$  by dipping method causes an increase in the size of the particles.

In addition to SEM imaging, EDX spectra of modified electrodes were recorded and the amount of cobalt in the modified materials were compared with the  $\text{LiMn}_{1.5}\text{Co}_{0.5}\text{O}_4$  (Mn75-Co25) composition to determine how much cobalt is introduced into the materials by multiple dipping in Figure 3.23.

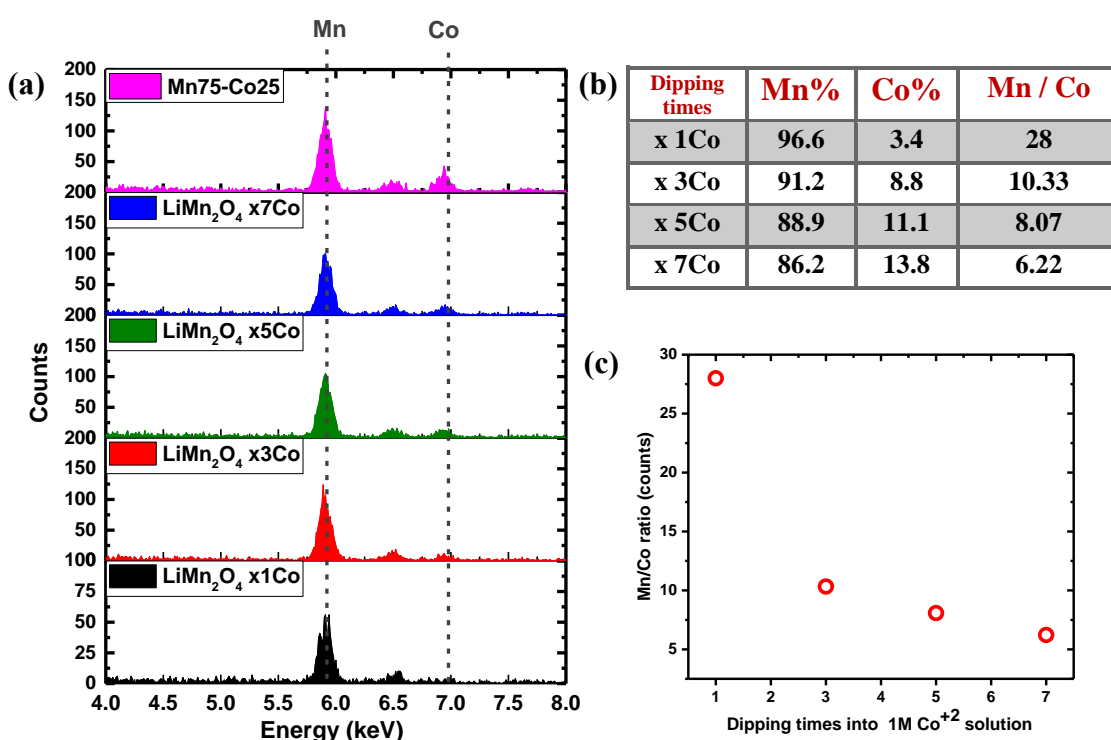


**Figure 3.23.** Atomic percentage of Mn and Co in the modified materials (a) EDX spectra of the dipped  $\text{LiMn}_2\text{O}_4$ . (b) Table of manganese to cobalt ratio as atomic percentages. (c) Plot of Mn/Co ratio vs dipping times into 1 M  $\text{Co}(\text{NO}_3)_2$  solution.

By analysis of the EDX spectra of dipped electrodes, first dipping procedure introduce small amount of cobalt into the material (3.4% compared to manganese). By continuing the dipping process, the cobalt amount could be increased but there is no linear increase, see Figure 3.23 (b) and (c). Introducing the amount of cobalt into the material decreases gradually in consecutive dipping process. The electrode, dipped 7-

times to the cobalt solution, has 13.8 % cobalt with respect to manganese. The amount cobalt is even lower than that of LMO of Mn75-Co25, obtained from the MASA process.

### 3.4.2 Water Oxidation Efficiency and Stability of Modified $\text{LiMn}_2\text{O}_4$ Electrodes by Dipping into Cobalt Solution

The modification of  $\text{LiMn}_2\text{O}_4$  produces cobalt species that diffuse into  $\text{LiMn}_2\text{O}_4$  and makes the electrode more active due to the fact that cobalt species are on the surface. To test the modified electrodes, the electrochemical characterization has been carried by first recording the CV of each electrode and compared with pure  $\text{LiMn}_2\text{O}_4$  electrode in terms of OER efficiency and current density increase. The CVs of the electrodes are shown in Figure. 3.24.

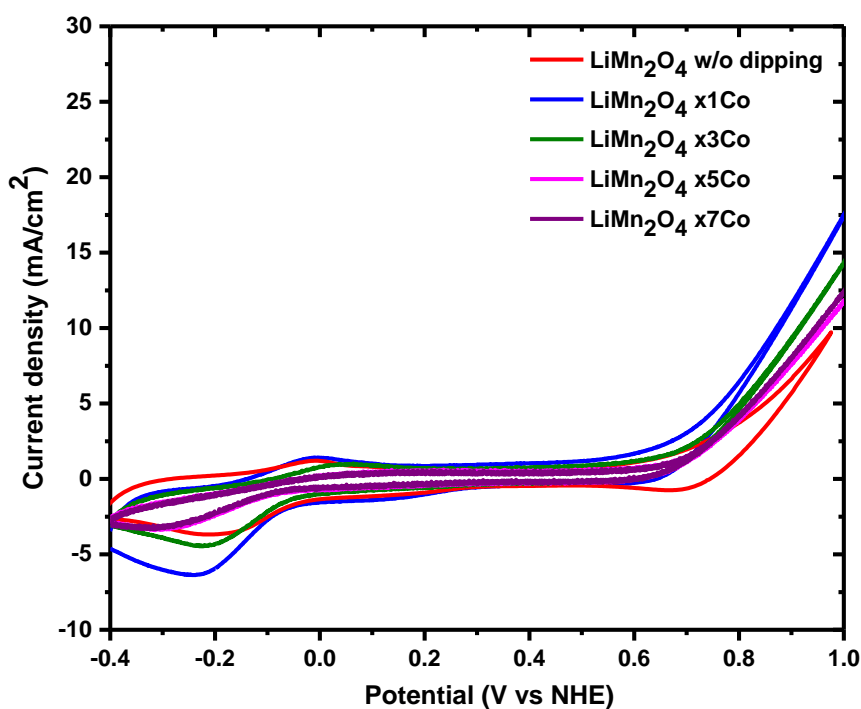


**Figure 3.24.** CV curves of  $\text{LiMn}_2\text{O}_4$  and modified forms by dipping into 1 M  $\text{Co}(\text{NO}_3)_2$  solution.

As shown in the CV curves of modified electrodes, there is current density change in the region of manganese oxidation and reduction. Manganese active species on surface decrease and current density gets smaller by each dipping step. However,

there is no significant change in cobalt redox range and its surface amount couldn't be analyzed by CV curves. More importantly, there is a change in the OER potential range. By dipping process, the current density sharpness or slope increases and is comparable with the behavior of  $\text{LiMn}_2\text{O}_4$  electrode. The current density at 1 V reached to  $20 \text{ mA cm}^{-2}$  in 1-time dipped electrode, showing the effectiveness of the modification method towards obtaining better electrocatalysts for OER. It would be expected that by each dipping the catalyst will be more active because of more cobalt loading on the surface. However, the slope on the current density versus potential gradually declined by increasing dipping times. Therefore, it is better to check the pore parameters as a function of dipping time, because by adding cobalt into material, the mesoporous structure may not preserve its own morphology, pore size, pore volume etc. and it may cause bulk formation and blocking pores. After CV analysis, the Tafel slope analysis was carried for each modified electrodes with different number of dipping, see Figure 3.25. The Tafel slopes and overpotential values extracted at  $1 \text{ mA cm}^{-2}$  for 6 hrs CP are given in Table 3.8.

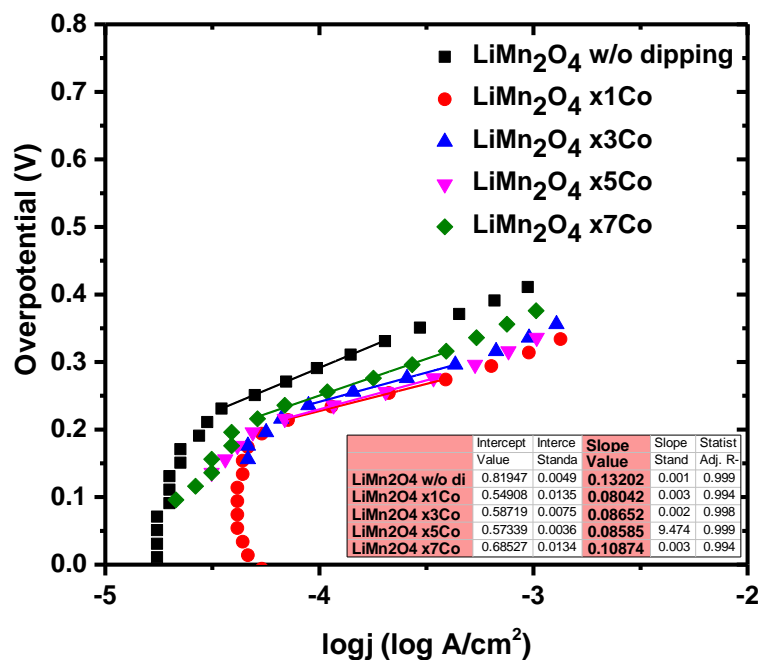
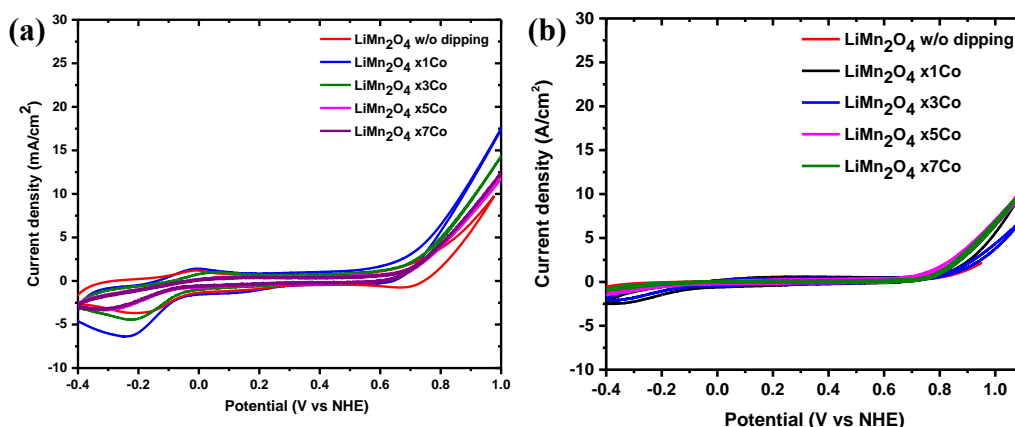


Figure 3.25. Tafel slope analysis of modified  $\text{LiMn}_2\text{O}_4$  electrodes.

Modified $\text{LiMn}_2\text{O}_4$ WE	Tafel Slope ( $\text{mV dec}^{-1}$ )	Overpotential at 1mA (mV)
$\text{LiMn}_2\text{O}_4$	132	491
$\text{LiMn}_2\text{O}_4 \times 1 \text{ Co}$	80	363
$\text{LiMn}_2\text{O}_4 \times 3 \text{ Co}$	86	377
$\text{LiMn}_2\text{O}_4 \times 5 \text{ Co}$	85	333
$\text{LiMn}_2\text{O}_4 \times 7 \text{ Co}$	108	413

**Table 3.8.** Tafel slopes and overpotential at 1 mA  $\text{cm}^{-2}$  for 6 hrs CP of the modified electrodes.

As expected from the CV curves, Tafel slopes of dipped electrodes are lower than pure  $\text{LiMn}_2\text{O}_4$  and Tafel analysis represent the effect of modification on electrode surface. Tafel slope of the electrodes are decreased from 132  $\text{mV dec}^{-1}$  to 80  $\text{mV dec}^{-1}$  by first dipping and accords well with the current density slope in CV curve of the 1-time dipped electrode. Then, with the increasing dipping time, the Tafel slope increases slightly to 85  $\text{mV dec}^{-1}$  and 3- and 5-times dipped electrodes show also good efficiency in OER with a higher Tafel slopes, compare Tafel slopes in Table 3.8. However, dipping process causes pores blocking and in 7-times dipped electrode, the Tafel slope increases to 108  $\text{mV dec}^{-1}$ . Still, the electrode has better performance than pure  $\text{LiMn}_2\text{O}_4$  but the 7-times dipped sample has the worst efficiency, compared to 1 to 5-times dipping. The CP results at 1 mA  $\text{cm}^{-2}$  are also consistent with Tafel slopes because for 1 to 5-times dipped electrodes, overpotential or energy required for OER at 1 mA  $\text{cm}^{-2}$  are decreased from 491 mV to around 350 mV. So by looking at both Tafel slopes and overpotentials, they correlate to each other.



**Figure 3.26.** Cyclic voltammograms of the modified  $\text{LiMn}_2\text{O}_4$  WEs (a) 1<sup>st</sup> CV curve (b) CV curves after CP at 1 mA  $\text{cm}^{-2}$  for 6 hrs.

Furthermore, the stability test of the WEs were done by CV curves after CP at  $1\text{ mA cm}^{-2}$ . Figure 3.26 compares the stability and shows the first and last CV curves of all WEs. As given the CVs in Figure 3.26 (a) and (b), the electrodes of all pure  $\text{LiMn}_2\text{O}_4$  and its modified forms, show significant decrease in current density after using them in OER process at  $1\text{ mA cm}^{-2}$  for 6 hrs. It was known that the pure  $\text{LiMn}_2\text{O}_4$  was not stable after using for oxygen evolution process in alkaline medium. However, in this case, the electrodes modified by dipping method also show low stabilities and they behave like pure  $\text{LiMn}_2\text{O}_4$  after CP  $1\text{ mA cm}^{-2}$ . The  $\text{LiMn}_2\text{O}_4$  material is not stable enough for long term OER applications and also using its modified form into OER gives reasonable efficiencies but shows ineffective results in stability. So, a more stable composition should be chosen to apply the dipping process. To do that all compositions should be tested before and after dipping directed modification of the electrodes.

### **3.5 Stability of $\text{LiMn}_{2-x}\text{Co}_x\text{O}_4$ Electrodes for Modification**

To improve the stability of electrode that is used for dipping process, calcination or annealing temperature of  $\text{LiMn}_2\text{O}_4$  electrode and adding small amount of cobalt (from 5 to 25%) to the preparation of the initial solutions were tested as an alternative to  $\text{LiMn}_2\text{O}_4$  electrode. This ensures consumption of less amount of cobalt salt in the solution preparation. Then, the electrodes prepared by both approaches were used for the stability tests in tough and long-term OER experiments.

#### **3.5.1 $\text{LiMn}_2\text{O}_4$ (Mn100-Co0) WE by Increasing Annealing Temperature**

In this part, the effect of crystallization on stability of electrode by increasing calcination temperature were discussed. The CVs of the  $\text{LiMn}_2\text{O}_4$  electrodes, calcined at higher temperatures of  $\text{LiMn}_2\text{O}_4$  are shown in Figure 3.27.

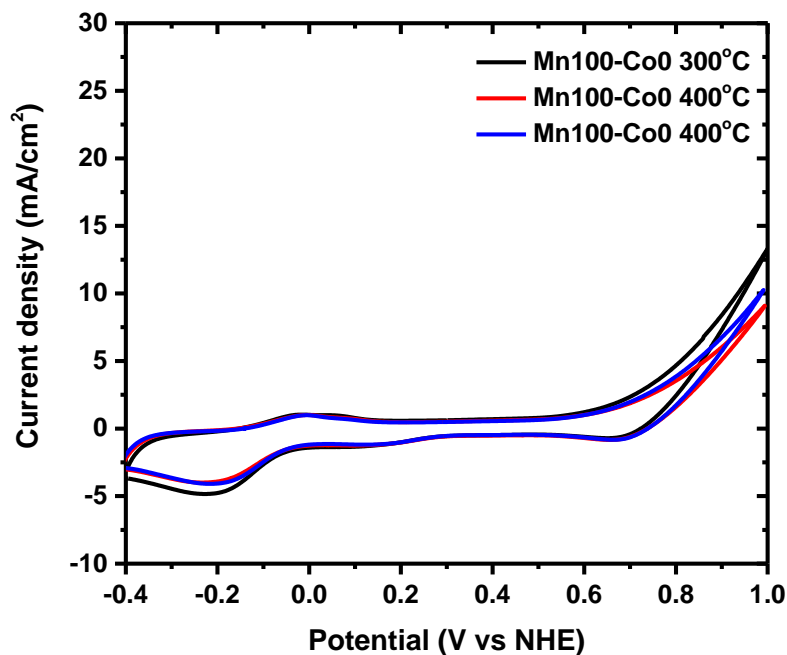


**Figure 3.27.** CVs of  $\text{LiMn}_2\text{O}_4$  electrodes, calcined at 300, 400 and 500 °C.

Accordingly, the electrodes of  $\text{LiMn}_2\text{O}_4$  were annealed to 400 °C and 500°C and compared with the one synthesized at 300 °C. The CVs of the electrodes show very similar behavior in the potential ranges of both non-faradaic and OER regions. Also, the Tafel slope analysis were done to obtain detailed information about whether there is an effect of calcination temperature on OER efficiency. To apply tough conditions on WEs, the CP experiments were run for 12 hrs at  $1 \text{ mA cm}^{-2}$  and 6 hrs at  $10 \text{ mA cm}^{-2}$ . The results of the Tafel slopes and overpotentials at 1 and  $10 \text{ mA cm}^{-2}$  current densities are given in Table 3.9.

<b><math>\text{LiMn}_2\text{O}_4</math> WE calcination temperature</b>	<b>Tafel Slope (<math>\text{mV dec}^{-1}</math>)</b>	<b>Overpotential at 1mA (mV) 12hrs</b>	<b>Overpotential at 10mA (mV) 6hrs</b>
<b>300 °C</b>	<b>130</b>	<b>491</b>	<b>1354</b>
<b>400 °C</b>	<b>128</b>	<b>351</b>	<b>1601</b>
<b>500 °C</b>	<b>123</b>	<b>582</b>	<b>1327</b>

**Table 3.9.** Tafel slopes and overpotential results at 1 and  $10 \text{ mA cm}^{-2}$  of the  $\text{LiMn}_2\text{O}_4$  WE, calcined at 3 different temperatures.

According to the Tafel slopes of the  $\text{LiMn}_2\text{O}_4$  electrodes, calcined at different temperatures, the slopes are not affected by temperature change much, the values are very close to each other and it is around  $130 \text{ mV dec}^{-1}$ . The synthesis temperature affects many properties such as crystallization, crystal size, surface area, and active side on surface. Accordingly, all these parameters may have opposing effects in the efficiencies and may cancel to each other. For instance, increasing crystallinity may improve OER efficiency by improving the conductivity of the electrode, however the surface area decreases and reduces the number of active sides on the electrode surface. So, these two parameters may eliminate each other in the OER effectivity. The CP results show that the electrode prepared at  $400^\circ\text{C}$  is an ideal material for OER at  $1 \text{ mA cm}^{-2}$ , because its overpotential is the lowest,  $351 \text{ mV}$ . To compare it with WE of  $300^\circ\text{C}$ , the  $\text{LiMn}_2\text{O}_4$  electrode prepared at  $400^\circ\text{C}$  has a lower surface area with larger crystals. Thus, the crystallinity effect is dominant in the OER process at low current densities. The electrode prepared at  $500^\circ\text{C}$  has a much larger overpotential. The reason could be due to formation of  $\text{Mn}_2\text{O}_3$  in the material (see Figure 3.3) and it decreases the OER efficiency at low current density experiments. At  $10 \text{ mA cm}^{-2}$ , the overpotentials of the WEs at  $300^\circ\text{C}$  and  $500^\circ\text{C}$  are very close but the electrode performance got worse in the  $400^\circ\text{C}$  electrode during the experiment and increases up to  $1601 \text{ mV}$  at the end of 6 hours. So this electrode is not stable in the CP experiment at high current density.

After measurements of both CP at  $1$  and  $10 \text{ mA cm}^{-2}$ , the CV curves were recorded to compare their stabilities with  $\text{LiMn}_2\text{O}_4$  at  $300^\circ\text{C}$ . In Figure 3.28, curves are shown after each CP experiments.

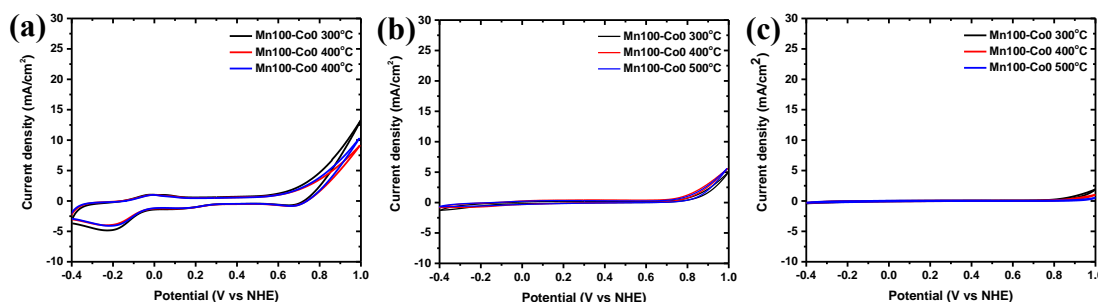


**Figure 3.28.** CVs of  $\text{LiMn}_2\text{O}_4$  at different temperatures (a) 1<sup>st</sup> curve, (b) CV after CP at  $1 \text{ mA cm}^{-2}$ , and (c) CV after CP  $10 \text{ mA cm}^{-2}$ .

So, the CV curves of WEs at from 300 °C to 500 °C after CP measurements show the instability of the  $\text{LiMn}_2\text{O}_4$  WE even if they are synthesized at higher temperatures. This is because, in the potential range of OER, the current density slopes are quite small after CP at  $1\text{mA cm}^{-2}$ . In the CV after CP at  $10\text{ mA cm}^{-2}$ , the current densities in OER range are almost disappeared.

### 3.5.2 $\text{LiMn}_2\text{O}_4$ WE by Adding 5% to 25% Cobalt(II) Salt in the Initial Preparation Solution

By increasing the calcination temperature of  $\text{LiMn}_2\text{O}_4$ , it was shown that the stability of the electrodes could not be improved in the CP measurements. In the previous sections, the synthesis of solid solutions of  $\text{LiMn}_{2-x}\text{Co}_x\text{O}_4$  has been discussed and found out the films have good stability. It has also been shown that the Mn75-Co25 is a good example in terms of stability and activity. However, 25% cobalt is still too high for the aim of using minimum amount of cobalt salt in the synthesis. Thus, in this part, the amount of cobalt salt was used as small as possible from 5 to 25% in the initial solutions to synthesize thin films and electrodes. The electrodes were tested for the stability after OER experiment, see Figure 3.29.



**Figure 3.29.** Thin films of Mn%-Co% on microscope slides

The thin films, prepared by adding small quantities cobalt species into  $\text{LiMn}_2\text{O}_4$  composition show some trends in the film quality. By increasing the cobalt salt percentage in the mesophase, the films became smooth and uniform, especially over the cobalt percentage of 10 to 15%. This distinction between pure form of

$\text{LiMn}_2\text{O}_4$  and  $\text{LiMn}_{2-x}\text{Co}_x\text{O}_4$ , synthesized by adding small quantities of cobalt salt was also investigated by SEM imaging, see Figure 3.30.

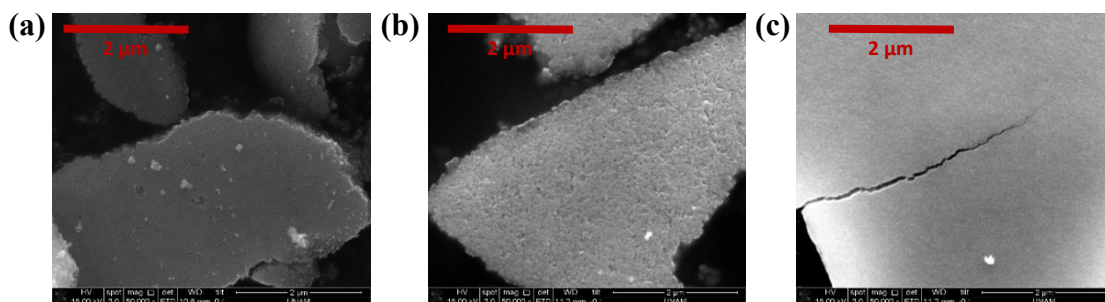


**Figure 3.30.** SEM images of Mn100-Co0, Mn90-Co10, Mn80-Co20.

According to the SEM images of the materials, the Mn90-Co10 is at the interface between quality and non-uniform films. The particles easily visible and the edges of the film are not smooth in the  $\text{LiMn}_2\text{O}_4$  film. On the other hand, the film of Mn80-Co20 has sharper edges with fine particles that are too small to observe in the SEM image. For this reason, the film of Mn90-Co10 shows feature between these two compositions.

The film quality was examined whether it provides long-term stability or not in the OER process. So, the CV of each electrode were recorded as a first step towards stability test. Figure 3.31 shows a set of CV of  $\text{LiMn}_{2-x}\text{Co}_x\text{O}_4$  between x of 0.1 and

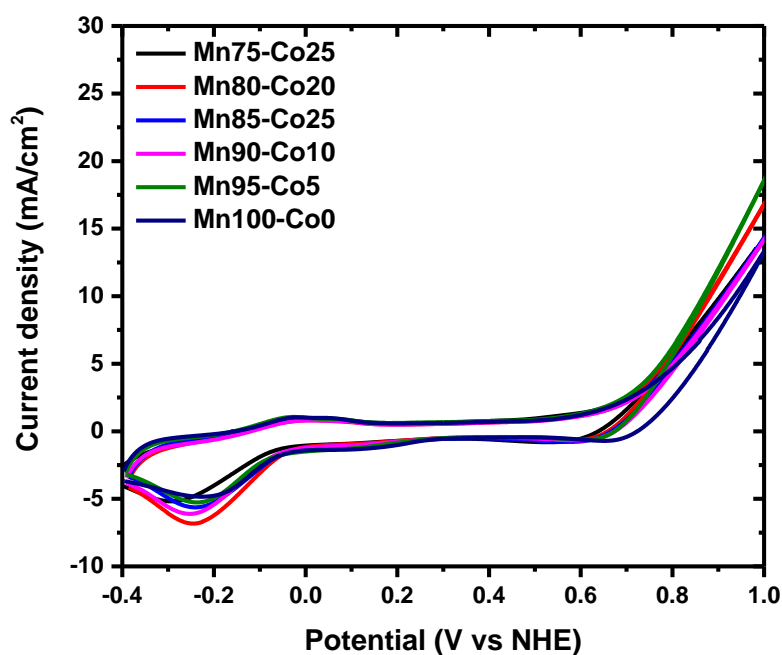


**Figure 3.31.** Cyclic Voltammograms of Mn%-Co%

0.5. The CVs of all ratios display similar results in the OER potential range. As shown previously the Mn100-Co0 WE show a low current density slope in the potential range of OER.

To determine the details on the OER efficiency and stability of the electrodes, the Tafel slope was extracted and CP experiments were done at 1 mA cm<sup>-2</sup> for 12hrs and 10 mA cm<sup>-2</sup> for 6 hrs to test the electrodes in tough experimental conditions. The Tafel slopes and overpotential results at 1 and 10 mA cm<sup>-2</sup> are tabulated in Table 3.10.

<b>Mn%-Co%</b>	<b>Tafel Slope (mV dec<sup>-1</sup>)</b>	<b>Overpotential at 1mA (mV) 12 hrs</b>	<b>Overpotential at 10mA (mV) 6 hrs</b>
<b>Mn100-Co0</b>	<b>130</b>	<b>491</b>	<b>1354</b>
<b>Mn95-Co5</b>	<b>117</b>	<b>704</b>	<b>1601</b>
<b>Mn90-Co10</b>	<b>72</b>	<b>441</b>	<b>1327</b>
<b>Mn85-Co15</b>	<b>68</b>	<b>361</b>	<b>1123</b>
<b>Mn80-Co20</b>	<b>64</b>	<b>304</b>	<b>826</b>
<b>Mn75-Co25</b>	<b>68</b>	<b>294</b>	<b>750</b>

**Table 3.10.** Tafel slopes and overpotential results of Mn%-Co% WEs at 1 and 10 mA cm<sup>-2</sup>.

According to Tafel slope values of the electrodes, by increasing cobalt species in the material, the slope gets incrementally smaller that means the WEs become more efficient by adding 5% cobalt in each time. The Mn95-Co5 still has quite a high Tafel slope (117 mV dec<sup>-1</sup>) and it is close to pure LiMn<sub>2</sub>O<sub>4</sub>. However, with the addition 5% cobalt salt once more and reaching the ratio of Mn90-Co10 makes the electrode significantly efficient with a Tafel slope of 72 mV dec<sup>-1</sup>. Then with further addition of more cobalt up to 25%, the Tafel slope is slightly improved. The CP experiments at 1 and 10 mA cm<sup>-2</sup> using each composition show the same trend. For instance, pure LiMn<sub>2</sub>O<sub>4</sub> has overpotential of 491 mV at 1 mA cm<sup>-2</sup> and 1354 mV at 10 mA cm<sup>-2</sup>. Addition of first 5% cobalt, the Mn95-Co5 sample, the overpotentials at both current densities increased and addition of another 5% cobalt, the Mn90-Co10 sample, the potential required for OER at 1 and 10 mA cm<sup>-2</sup> decreased to 441 mV and 1327 mV, respectively. Further increasing the cobalt percentage in the LMO gradually decreased the overpotentials down to 294 mV in the Mn75-Co25 sample. The stability of the electrodes were tested by recording their CV after the CP experiments at 1 and 10 mA cm<sup>-2</sup>, see Figure3.32.

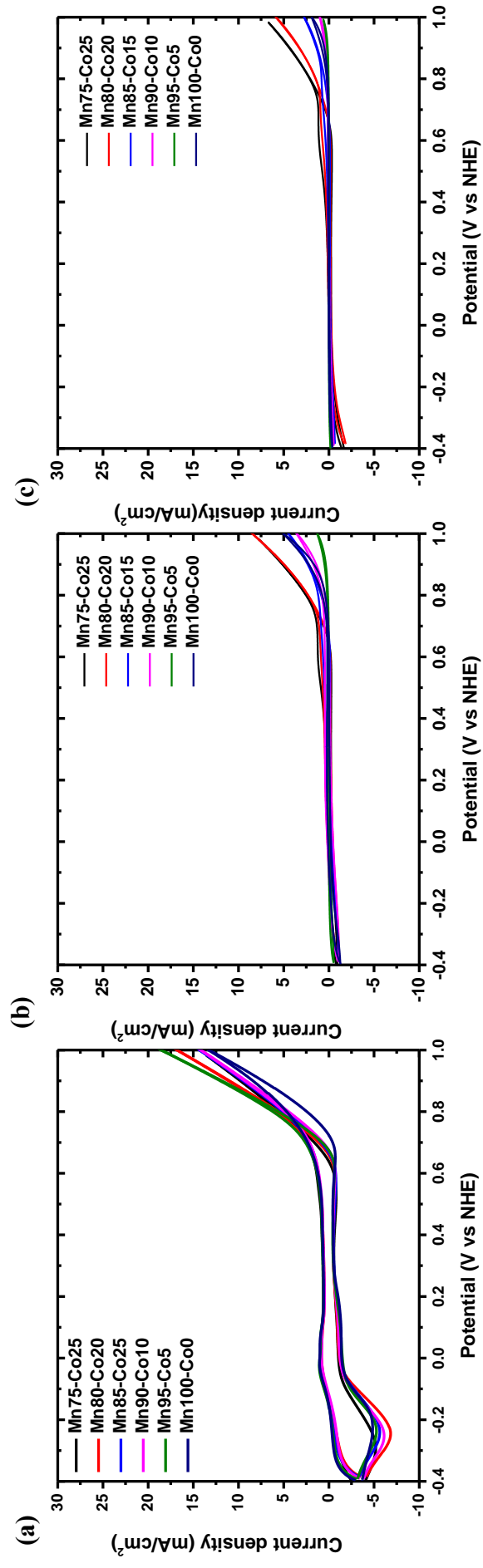


**Figure 3.32.** CVs of Mn%-Co% WEs and modified WEs (a) 1<sup>st</sup> CV curves, (b) CV curves after CP at 1 mA cm<sup>-2</sup> for 12 hrs, and (c) CV curves after CP at 10 mA cm<sup>-2</sup> for 6 hrs.

The CVs of the electrodes, including cobalt amount 5 to 25%, after CP at  $1 \text{ mA cm}^{-2}$  for 12 hrs, show a drastic current density decrease in the potential range of OER. However, some of the ratios, like Mn75-Co25 and Mn80-Co20, the drop in their current density vs potential slopes are quite in significant. This is because the samples with low cobalt, below 20%, lose their efficiencies and stabilities. Therefore, minimum 20% cobalt is needed for a high quality and highly efficient electrodes. The CP experiment at  $10 \text{ mA cm}^{-2}$  current density for 6 hrs did not alter the behavior. The Mn100-Co0, Mn95-Co5 and Mn90-Co10 electrodes lost their current density slope completely and OER abilities are destroyed. These stabilities with increasing cobalt percentage is also correlated in the film quality, see Figures 3.32 (a) and (b). The film quality gets better after 15% cobalt and it shows that the film quality has a significant effect on the activity stability of the electrodes.

Therefore, the electrodes, including from 5 to 15% cobalt, are also not stable under tough CP experiment conditions. However, the Mn75-Co25 and Mn80-Co20 still have good OER efficiency and could be used as LMO substrates for dipping process. Because the Mn80-Co20 sample has lower cobalt, it has been chosen as the composition for cobalt modification by the dipping method. Since the Mn85-Co15 sample still has efficiency in OER process (but it loses stability by lost in current density), this composition dipping process was also employed to improve its stability.

### 3.6 Modified Mn80-Co20 and Mn85-Co15 WEs and Efficiency in Water Oxidation

The electrodes with 20 and 15% of cobalt in  $\text{LiMn}_{2-x}\text{Co}_x\text{O}_4$  were chosen as two ratios to modify by dipping process and their efficiency and stabilities were tested by applying general electrochemical experiments.

#### 3.6.1 Modification of Mn80-Co20 with Dipping Process and Increase in OER Efficiency

To increase the efficiency of Mn80-Co20, dipping process was done from 1- to 5- times and the CVs of the dipped electrodes are compared with the undipped Mn80-Co20. The CVs of the modified electrodes are shown in Figure 3.33.

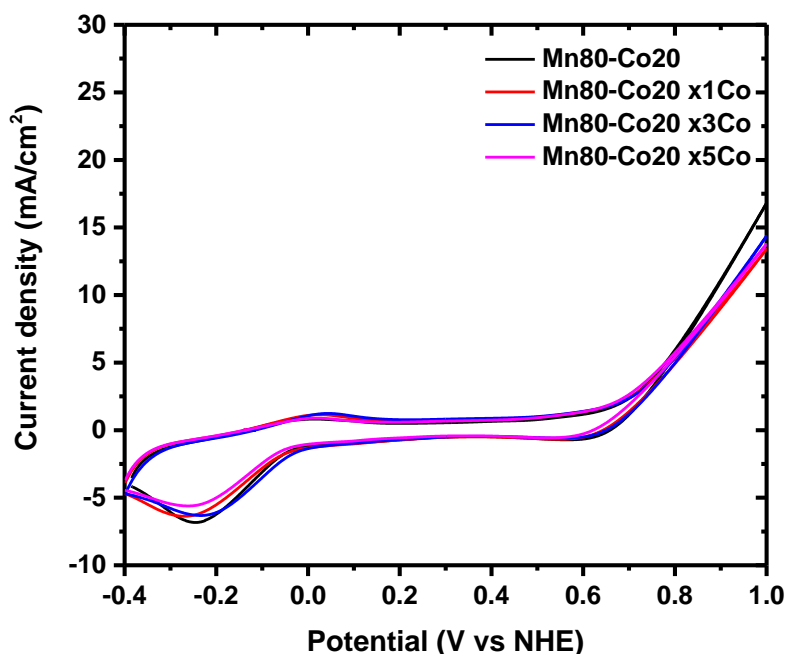


**Figure 3.33.** CV curves of Mn80-Co20 WE and modified WEs.

According to the changes in CVs, there is no changes in the current density among the modified electrodes in the potential range of OER. The Mn80-Co20 electrode without dipping into cobalt solution, has a slightly higher current density in the 0.8 and 1 V range. This could be because of the resistance of the used FTO or as expected the undipped electrode has a higher surface area. Accordingly, it may provide a slightly more active sites on electrode surface. To analyze their OER efficiencies in

detail, the Tafel slope analysis and CP at 1 mA cm<sup>-2</sup> for 12 hrs and 10 mA cm<sup>-2</sup> for 6 hrs were also done, see the results in Table 3.11.

<b>Mn80-Co20 xCo</b>	<b>Tafel slope (mV dec<sup>-1</sup>)</b>	<b>Overpotential at 1mA (mV) 12 hrs</b>	<b>Overpotential at 10mA (mV) 6 hrs</b>
<b>Mn80-Co20</b>	<b>64</b>	<b>304</b>	<b>826</b>
<b>Mn80-Co20 x1Co</b>	<b>56</b>	<b>325</b>	<b>657</b>
<b>Mn80-Co20 x3Co</b>	<b>51</b>	<b>279</b>	<b>576</b>
<b>Mn80-Co20 x5Co</b>	<b>46</b>	<b>265</b>	<b>546</b>

**Table 3.11.** Tafel Slopes and overpotential results of Mn80-Co20 and modified forms WEs at 1 mA cm<sup>-2</sup> and 10 mA cm<sup>-2</sup>

Both the Tafel slopes and overpotentials of the dipped Mn80-Co20 show a nice trend. In other words, while the Tafel slope decreases, the overpotentials at 1 and 10 mA cm<sup>-2</sup> or the required energy at these current densities decreases. Especially, these results can be compared with the Mn50-Co50 composition. By dipping method, the Mn80-Co20 electrode surface became very active, each dipping provided a significant decrease in Tafel slope values and reaches to the Tafel slope of Mn50-Co50 ratio. Remember that in the modification of Mn100-Co0, the Tafel slopes increased by each dipping process after 1<sup>st</sup> one. However, in the Mn80-Co20, the trend is opposite. Therefore, the film quality of the material has a detrimental effect on the OER efficiency of the LiMn<sub>2-x</sub>Co<sub>x</sub>O<sub>4</sub> electrodes. Also, CP experiments show that the overpotential at 1 and 10 mA cm<sup>-2</sup> are very low even compared to Mn50-Co50. The 3-times dipping of Mn80-Co20 has 265 mV at 1 mA cm<sup>-2</sup> and 546 mV at 10 mA cm<sup>-2</sup> overpotentials. These results are the best results obtained among the samples, tested in this thesis.

After obtaining lower Tafel slopes and overpotentials from the CP measurements, one of the most important parameters of the electrodes, stability, was checked by CV. The CVs of the dipped electrodes of Mn80-Co20 are shown in Figure 3.34.

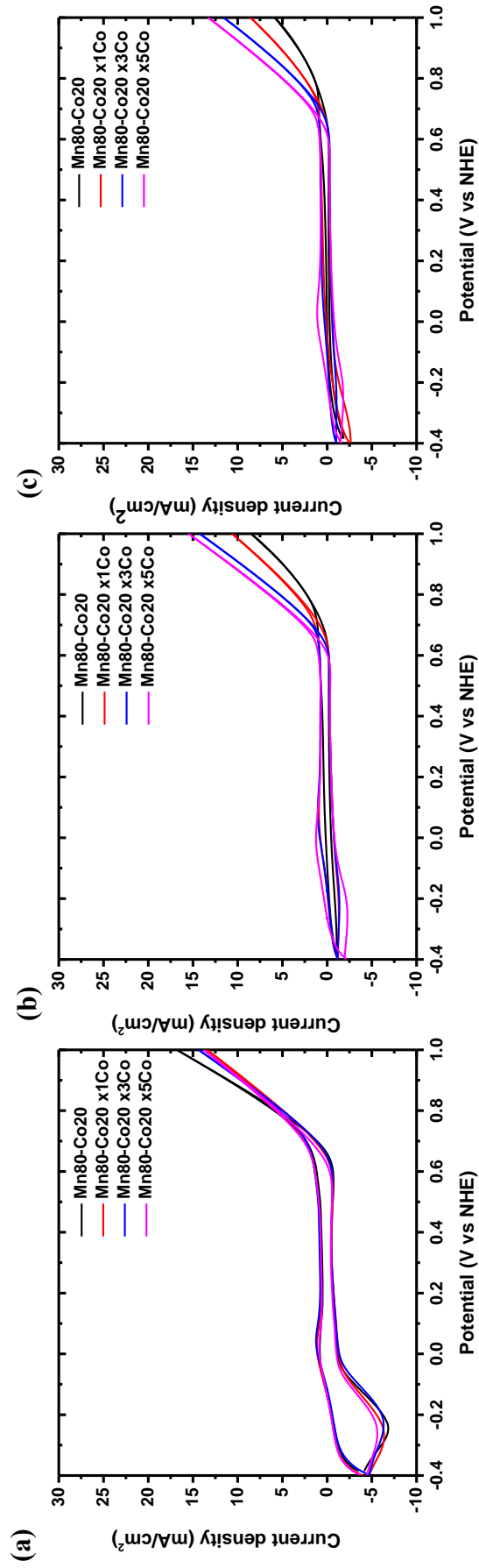


**Figure 3.34.** CVs of Mn80-Co20 WEs and modified WEs (a) 1<sup>st</sup> CV curves, (b) CV curves after CP at 1 mA cm<sup>-2</sup> for 12 hrs, and (c) CV curves after CP at 10 mA cm<sup>-2</sup> for 6 hrs.

In previous section, it has been shown that the most stable electrode with a lowest cobalt composition is Mn80-Co20. Therefore, it has been used for modification by dipping process. The CV curves of the modified electrodes after CP experiments show that the stability of the modified electrodes is also better. Especially, in the range of 0.7 and 1V, the current density lost is very low in the 1- and 3-times dipped electrodes, compared to undipped Mn80-Co20. The CV curves after CP at 1 and 10 mA cm<sup>-2</sup> of the Mn80-Co20 electrode dipped 5-times, shows almost same curve with first CV curve of the WE before CP experiment. So, both targeted efficiencies and stabilities have been achieved by this process using Mn80-Co20 electrodes.

### 3.6.2 Mn85-Mn15 with Dipping Process and Increasing Stability after OER

The Mn85-Co15 electrode was at the border line that this composition showed an average stability among WEs and it has smaller amount of cobalt. In this section, the effect of dipping method on the stability was discussed by using Mn85-Co15 ratio. The electrode was dipped from 1- to 5-times and the same measurement procedures were applied on modified Mn85-Co15 WE. So to analyze the performance of this electrode, the Tafel slope and overpotential at 1 and 10 mA cm<sup>-2</sup> current densities were extracted from the measurements. These results are given in Table 3.12.

<b>Mn85-Co15 xCo</b>	<b>Tafel Slope (mV dec<sup>-1</sup>)</b>	<b>Overpotential at 1mA (mV) 12 hrs</b>	<b>Overpotential at 10mA (mV) 6 hrs</b>
<b>Mn85-Co15</b>	<b>68</b>	<b>361</b>	<b>1123</b>
<b>Mn85-Co15 x1Co</b>	<b>59</b>	<b>290</b>	<b>837</b>
<b>Mn85-Co15 x3Co</b>	<b>52</b>	<b>283</b>	<b>596</b>
<b>Mn85-Co15 x5co</b>	<b>47</b>	<b>270</b>	<b>636</b>

**Table 3.12.** Tafel slopes and overpotential results of Mn85-Co15 and modified WEs at 1 and 10 mA cm<sup>-2</sup> current densities.

The Tafel slopes of the modified electrodes improved in each dipping, the efficiency of Mn85-Co15 increased subsequently. The Tafel slopes are very similar to the modified Mn80-Co20. Also, the overpotential values at 1 mA cm<sup>-2</sup> also showed that the required energy for OER decreases slightly by increasing dipping times from 1 to 5. However, under tough experiment conditions, such as at 10 mA cm<sup>-2</sup>, the overpotential results do not have a trend by increasing dipping times. As shown, the Mn85-Co15 and 1-time dipped samples have very close results at both 1 and 10 mA cm<sup>-2</sup>. Only 1-time dipping is not enough to reduce the overpotential. However, in the

3-times dipped electrode, there is an effective deposition of cobalt on surface because the potential required for OER at  $10 \text{ mA cm}^{-2}$  is 596 mV. When the WEs were modified by 5-times dipping, at higher current density,  $10 \text{ mA cm}^{-2}$ , the overpotential increased further to 636 mV. So, the 5-times dipping makes the electrode nondurable under harsh experiments, performed at higher current densities.

The modified electrodes of Mn85-Co15 provided constructive results about their efficiency in OER (as provided by Tafel analysis and overpotential results). However, the reason of picking this composition was to test whether the dipping process enhances the stability of the electrodes or not. So to analyze stability by dipping, the CV curves of the modified electrodes after CP at 1 and  $10 \text{ mA cm}^{-2}$  were also recorded, see Figure 3.35.

According to the CV curves, after CP  $1 \text{ mA cm}^{-2}$  as shown in previous section, the Mn85-Co15 lost electrode stability after CP at 1 and  $10 \text{ mA cm}^{-2}$ . After modification of the Mn85-Co15, the slope of current density vs voltage in the range of OER still slightly decreased in the WEs of 1 and 3-times dipped. However, the electrode, obtained after 5-times dipping, doesn't show a current lost in the range of OER. The CVs, after CP at  $10 \text{ mA cm}^{-2}$ , show that the, current density is lost more in OER in the 1-time dipped WE. However, the 3-times dipped electrode slightly loses its current density after  $10 \text{ mA cm}^{-2}$  CP experiment. It means that the modification is also successful in terms of stability. With 5-times dipping, the current density slope is almost same in last curve as in the first CV curve of the material.

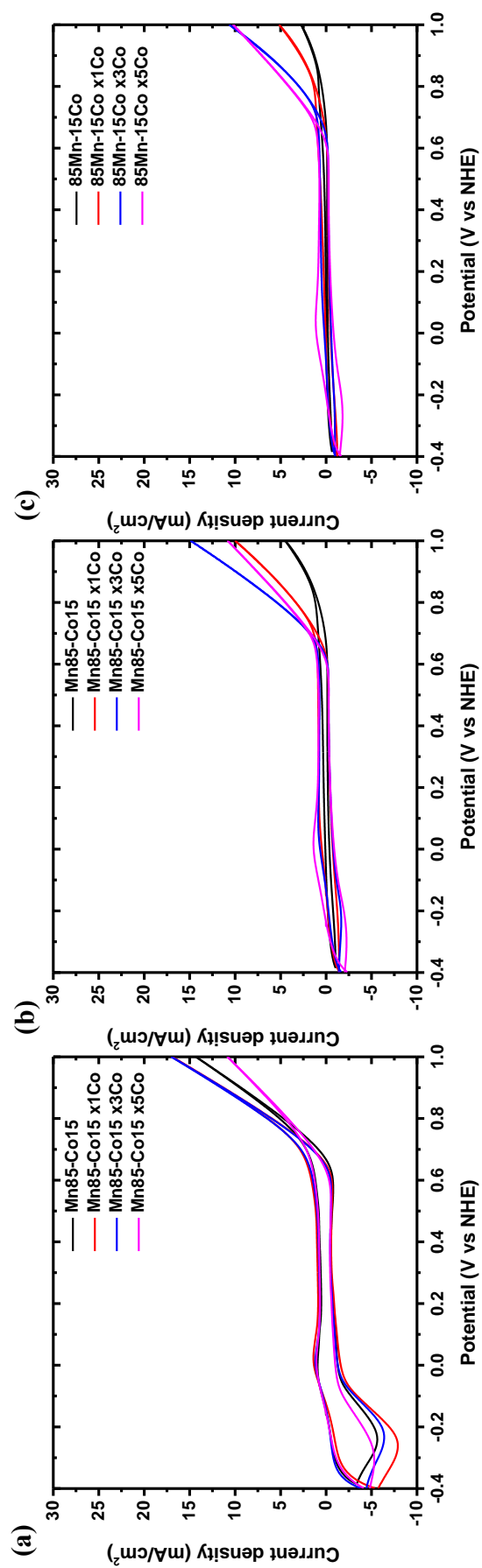


**Figure 3.35.** CVs of Mn85-Co15 WEs and modified WEs (a) 1<sup>st</sup> CV curves, (b) CV curves after CP at 1 mA cm<sup>-2</sup> for 12 hrs, and (c) CV curves after CP at 10 mA cm<sup>-2</sup> for 6hrs.

### 3.7 Summary

LMO Mn%-Co% xCo	Tafel Slope (mV dec <sup>-1</sup> )	$\eta$ at 1 mA (mV)	$\eta$ at 10 mA (mV)	Reference
Mn100-Co0 300°C	130	491	1354	This work
Mn100-Co0 400°C	128	351	1601	This work
Mn100-Co0 500°C	123	582	1327	This work
Mn95-Co5 300°C	117	704	1601	This work
Mn90-Co10 300°C	72	441	1327	This work
Mn85-Co15 300°C	68	361	1123	This work
Mn80-Co20 300°C	64	304	826	This work
Mn75-Co25 300°C	68	294	750	This work
Mn50-Co50 300°C	64	304	521	This work
Mn25-Co75 300°C	66	297	-	This work
Mn0-Co100 300°C	64	282	-	This work
Mn100-Co0 x1Co 300°C	80	363	-	This work
Mn100-Co0 x3Co 300°C	86	377	-	This work
Mn100-Co0 x5Co 300°C	85	333	-	This work
Mn100-Co0 x7Co 300°C	108	413	-	This work
Mn85-Co15 x1Co 300°C	59	290	837	This work
Mn85-Co15 x3Co 300°C	52	283	596	This work
Mn85-Co15 x5Co 300°C	47	270	636	This work
Mn80-Co20 x1Co 300°C	56	325	657	This work
Mn80-Co20 x3Co 300°C	51	279	576	This work
Mn80-Co20 x5Co 300°C	46	265	546	This work
Co <sub>3</sub> O <sub>4</sub> (Co100*) 300°C	56	311	621	This work
Mn <sub>3</sub> O <sub>4</sub> (Mn100*) 300°C	192	1056	1441	This work
Materials	Tafel Slope (mV dec <sup>-1</sup> )	$\eta$ at 1 mA (mV)	$\eta$ at 10 mA (mV)	Reference
LiMn <sub>2</sub> O <sub>4</sub>	140	550	-	[104]
LiMn <sub>1.5</sub> Co <sub>0.5</sub> O <sub>4</sub>	150	420	-	[104]
LiMnCoO <sub>4</sub>	120	410	530	[104]
LiMn <sub>0.5</sub> Co <sub>1.5</sub> O <sub>4</sub>	60	370	440	[104]
LiCoO <sub>2</sub>	50	370	410	[104]
Co <sub>3</sub> O <sub>4</sub>	47	-	363	[120]
RuO <sub>x</sub>	32			[121]
IrO <sub>x</sub>	35			[121]

**Table 3.13.** General table of the mesoporous metal oxide and lithiated metal oxides with Tafel slope and overpotential values at 1 mA cm<sup>-2</sup> and 10 mA cm<sup>-2</sup>

# Chapter 4

## Conclusion

In this thesis, mesoporous  $\text{LiMn}_{2-x}\text{Co}_x\text{O}_4$  thin films have been synthesized by MASA approach. The materials have been characterized and employed as anode electrodes for water oxidation reaction.

It has been shown that increasing the synthesis temperature increases the  $\text{LiMn}_2\text{O}_4$  nanocrystallite size, making the pore-walls. Also, the surface area subsequently decreases from 98 to 90, 69, 33  $\text{m}^2 \text{g}^{-1}$  by increasing the synthesis temperature from 300 to 600 °C. The temperature dependent OER catalytic performance shows that the Tafel slopes of  $\text{LiMn}_2\text{O}_4$  thin films synthesized at 300, 400 and 500 °C are very similar and they are around 130  $\text{mV dec}^{-1}$  with high overpotential values, consequently 491, 351 and 582 mV at 1  $\text{mA cm}^{-2}$  and 1354, 1601 and 1327 mV at 10  $\text{mA cm}^{-2}$

The mesoporous  $\text{LiMn}_{2-x}\text{Co}_x\text{O}_4$  (calcined at 300 °C) thin films have been characterized by XRD and it was identified that found that the synthesized materials with different manganese and cobalt content forms as solid solutions. Also adding 25 % cobalt species into pure  $\text{LiMn}_2\text{O}_4$  caused an increase on the surface area from 98 to 144  $\text{m}^2\text{g}^{-1}$ . Further increasing cobalt (x) to 50 and 75 % in the material caused slight decrease on the surface area from 144 to 124, 103  $\text{m}^2 \text{g}^{-1}$ . In their electrocatalytic performance, the pure  $\text{LiMn}_2\text{O}_4$  has a poor efficiency with a Tafel slope of 124  $\text{mV dec}^{-1}$ . However, the addition of 25% cobalt into  $\text{LiMn}_2\text{O}_4$  caused a drastic decrease in Tafel slope to 66  $\text{mV dec}^{-1}$  and further addition of cobalt didn't provide more decrease in the Tafel slopes. Also, the Tafel slope values of  $\text{LiMn}_{2-x}\text{Co}_x\text{O}_4$  WEs were correlated

with overpotentials at  $1 \text{ mA cm}^{-2}$  and shown that with increasing amount of cobalt in the  $\text{LiMn}_{2-x}\text{Co}_x\text{O}_4$  provides overpotential decrease from around 500 mV to 300 mV.

Instead of adding cobalt during the synthesis of  $\text{LiMn}_{2-x}\text{Co}_x\text{O}_4$ , the pure  $\text{LiMn}_2\text{O}_4$  electrode surface can be modified using the SILAR method using  $\text{Co(II)}$  solution with the aim of less use of cobalt salt. The  $\text{LiMn}_2\text{O}_4$  WEs can be modified 1-, 3-, 5- and 7-times by dipping, washing, and annealing steps in each times. The XRD characterization of the end products shows the formation of  $\text{Mn}_3\text{O}_4$  and proves that the cobalt species diffuse into the material surface and exchange with manganese to form cobalt rich  $\text{LiMn}_{2-x}\text{Co}_x\text{O}_4$  surface. This modification was also proven by XPS and elemental analysis using EDX spectroscopies. Their electrochemical activities in water oxidation reaction improved, compared to the unmodified form of  $\text{LiMn}_2\text{O}_4$ . The modification of WEs by dipping method, the Tafel slope decreases from 132 to  $80 \text{ mV dec}^{-1}$  in 1-time modification. Upon 3-, 5-, and 7-times dipping and calcination process, the Tafel slope of the WEs increase to 86, 85 and  $108 \text{ mV dec}^{-1}$ . The results were correlated with the overpotentials of these electrodes at  $1 \text{ mA cm}^{-2}$  current density. The stability tests of the modified WEs display low stability after applying  $1 \text{ mA cm}^{-2}$  for 6 hrs. The electrodes are not stable under alkaline conditions.

For the SILAR method also employed to improve the performance of the other compositions of  $\text{LiMn}_{2-x}\text{Co}_x\text{O}_4$ , in which the amount of cobalt was varied from 5 to 25 % by increasing cobalt amount in 5 % increments. The Tafel slope decreases from 117 to  $64 \text{ mV dec}^{-1}$  upon addition of 5 % cobalt as also correlated with the overpotential values at 1 and  $10 \text{ mA cm}^{-2}$ . However, this electrode is also not stable under our reaction conditions. It has been found that the  $\text{LiMn}_{2-x}\text{Co}_x\text{O}_4$  electrodes of 20 and 25% cobalt are stable under our conditions. Therefore, the modification processes were applied to those ratios.

The Tafel slope of the electrode of Mn80-Co20, upon dipping modification by 5-times, decreases from 64 to  $46 \text{ mV dec}^{-1}$  with a very low overpotential values of 265 and 543 mV at 1 and  $10 \text{ mA cm}^{-2}$  current densities. Also, the electrodes are stable under our reaction conditions. They show good performance without losing their efficiencies. The Mn85-Co15 electrode also shows a good catalytic performance after several times modification with an improved Tafel slope; it decreases from 68 to  $47 \text{ mV dec}^{-1}$  by 5-times dipping and annealing procedure with overpotentials of 270 mV

at  $1 \text{ mA cm}^{-2}$  and  $636 \text{ mV}$  at  $10 \text{ mA cm}^{-2}$ . The 5-times modification of the electrode makes this composition stable under tough electrochemical catalyst experiments.

As summary, the MASA process is effective method to synthesize mesoporous efficient catalysts of LMOs for OER and their post modification could further improve the performance of these materials and minimize the toxic but the essential component of the electrocatalyst.

## Future Recommendations

Up to now, the effect of SILAR method on Mn100-Co0 and  $\text{LiMn}_{2-x}\text{Co}_x\text{O}_4$  having maximum amount of manganese and minimum amount of cobalt species were investigated. In the modification process, the annealing temperature was always set to  $300 \text{ }^\circ\text{C}$ . Tafel slope and chronopotentiometry experiments of the modified pure  $\text{LiMn}_2\text{O}_4$  performed good with a low stability in long term OER processes. Therefore, the  $\text{LiMn}_{2-x}\text{Co}_x\text{O}_4$  electrodes with minimum amount of cobalt were targeted by considering the efficiency and stability. However, it still requires a fair amount of cobalt (15-20 %) and contrary to concept of using of minimum amount of cobalt species in the material.

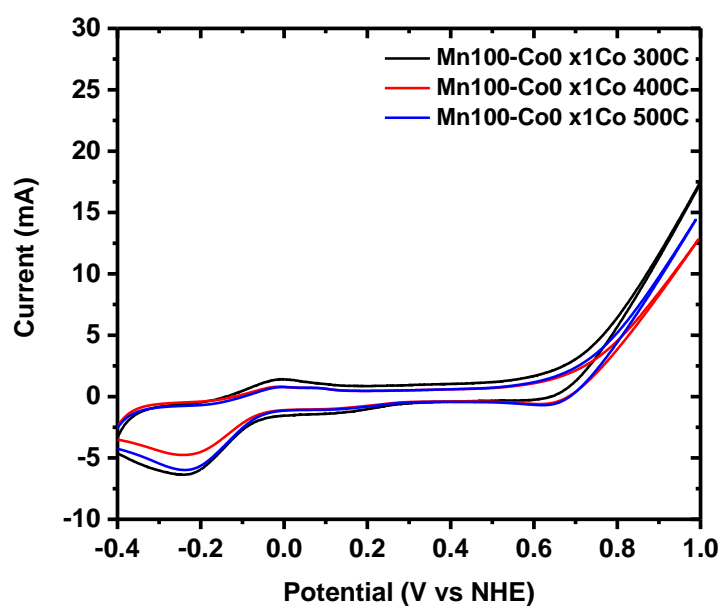


**Figure 4.1.** CV curves of modified  $\text{LiMn}_2\text{O}_4$  WEs by modification with annealing at 300, 400 and  $500 \text{ }^\circ\text{C}$ .

A preliminary electrochemical tests of the modified electrodes of Mn100-Co0 by dipping into cobalt solution annealing at 400 and 500 °C instead of 300 °C, were performed without any characterization. The electrochemical properties of these electrodes were compared to the modified electrode, annealed at 300 °C. In this test, mostly stabilities of electrodes by modification at 400 and 500 °C were investigated whether there is an effect of annealing temperature for modification. The CV curves of the electrodes were recorded, see Figure 4.1.

According to CVs of these electrodes, there is no significant difference among the CV curves. The current density increases in OER potential range are almost the same with an exception of current densities at 1 (V vs NHE). Also, the electrodes were used to determine their Tafel slopes and overpotential values, see Table 4.1. Increasing the annealing temperature from 300 to 400 and to 500 °C decreased the Tafel slopes from 80 to 61 mV dec<sup>-1</sup> with a slight decrease in the overpotential values. These results show that annealing temperature after dipping process has effect on the catalytic performances of the electrodes and needs to be investigated. To show whether the modified electrodes are stable, the CV of the electrodes were also recorded after 12 hrs CP experiments, see Figure 4.2.

<b>WE x1Co annealing temperature</b>	<b>Tafel Slope (mV dec<sup>-1</sup>)</b>	<b>Overpotential at 1mA (mV) 12 hrs</b>
<b>300 °C</b>	<b>80</b>	<b>363</b>
<b>400 °C</b>	<b>78</b>	<b>326</b>
<b>500 °C</b>	<b>61</b>	<b>343</b>

**Table 4.1.** Tafel slopes and overpotential values at 1 mA cm<sup>-2</sup> of the modified LiMn<sub>2</sub>O<sub>4</sub> WEs by modification and annealing at 300, 400 and 500 °C.

In previous experiments, it was shown that pure LiMn<sub>2</sub>O<sub>4</sub> (Mn100-Co0) and their modified forms by annealing at 300 °C, showed to be unstable by cyclic voltammetry after CP at 1 mA cm<sup>-2</sup>. However, the electrodes annealed at 400 and 500 °C are observed to be more stable than the one annealed at 300 °C after applying 1 mA for 12 hrs, see Figure 4.2. It could be concluded that increasing annealing temperature provides more crystalline materials and also by addition of cobalt into material, both catalytic performance and stability get better.

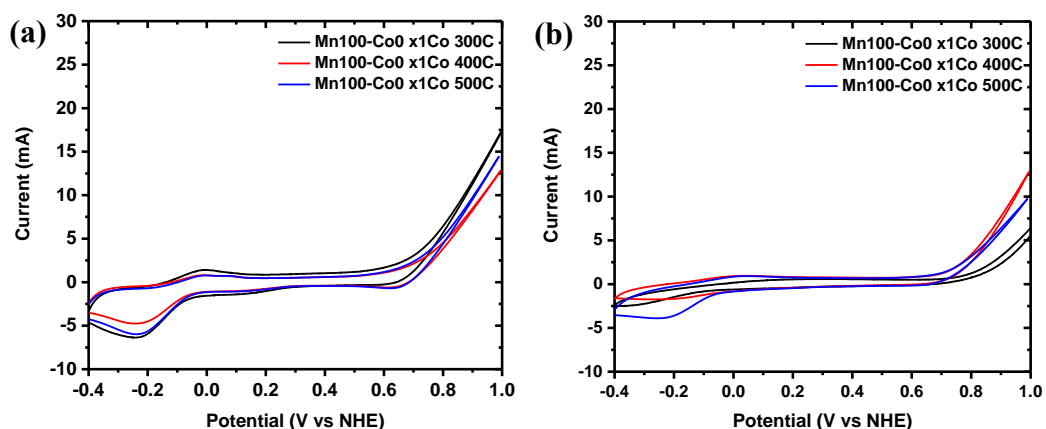


**Figure 4.2.** CVs of modified Mn100-Co0 by annealing at 300, 400 and 500 °C **(a)** 1<sup>st</sup> CV curves, **(b)** CV curves after CP at 1 mA cm<sup>2</sup> for 12 hrs.

Based on this experiment, the effect of annealing temperature needs to be investigated as an important parameter for the modified electrode performance. So, to investigate in details of this parameter, characterization of the modified electrodes by annealing at higher temperatures needs further experiments. Also, annealing time could be another parameter in the SILAR and annealing process and it could be investigated to see if there is a significant effect for stability or electrode performance. Furthermore, the investigations can be expanded to include other transition metals in the system, like, Fe and Ni.

# Bibliography

- [1] M. S. Park, J. Kim, K. J. Kim, J. W. Lee, J. H. Kim, and Y. Yamauchi, "Porous nanoarchitectures of spinel-type transition metal oxides for electrochemical energy storage systems," *Phys. Chem. Chem. Phys.*, vol. 17, pp. 30963–30977, 2015.
- [2] G. Wang *et al.*, "Hydrothermal synthesis and optical, magnetic, and supercapacitance properties of nanoporous cobalt oxide nanorods," *J. Phys. Chem. C*, vol. 113, pp. 4357–4361, 2009.
- [3] A. Walcarius, "Mesoporous materials and electrochemistry," *Chem. Soc. Rev.*, vol. 42, pp. 4098–4140, 2013.
- [4] W. Stöber, A. Fink, and E. Bohn, "Controlled growth of monodisperse silica spheres in the micron size range," *J. Colloid Interface Sci.*, vol. 26, pp. 62–69, 1968.
- [5] V. Chiola, J. E. Ritsko, and C. D. Vanderpool, "Process for producing low-bulk density silica," 1971.
- [6] C. Liang, Z. Li, and S. Dai, "Mesoporous carbon materials: Synthesis and modification," *Angew. Chemie - Int. Ed.*, vol. 47, pp. 3696–3717, 2008.
- [7] C. T. Kresge, M. E. Leonowicz, W. J. Roth, J. C. Vartuli, and J. S. Beck, "Ordered mesoporous molecular sieves synthesized by a liquid-crystal template mechanism," *Nature*, vol. 359, pp. 710–712, 1992.
- [8] R. M. Rioux, H. Song, J. D. Hoefelmeyer, P. Yang, and G. A. Somorjai, "High-surface-area catalyst design: Synthesis, characterization, and reaction studies of platinum nanoparticles in mesoporous SBA-15 silica," *J. Phys. Chem. B*, vol. 109, pp. 2192–2202, 2004.
- [9] A. H. Khan *et al.*, "Two-dimensional (2D) nanomaterials towards electrochemical nanoarchitectonics in energy-related applications," *Bull. Chem. Soc. Jpn.*, vol. 90, pp. 627–648, 2017.
- [10] D. Zhao *et al.*, "Triblock copolymer syntheses of mesoporous silica with periodic 50 to 300 angstrom pores," *Science (80-. )*, vol. 279, pp. 548–552, 1998.
- [11] U. Ciesla, S. Schacht, G. D. Stucky, K. K. Unger, and F. Schüth, "Formation of

- a porous zirconium oxo phosphate with a high surface area by a surfactant-assisted synthesis,” *Angew. Chemie (International Ed. English)*, vol. 35, pp. 541–543, 1996.
- [12] Q. Huo *et al.*, “Generalized synthesis of periodic surfactant/inorganic composite materials,” *Nature*, vol. 368, pp. 317–321, 1994.
- [13] D. M. Antonelli and J. Y. Ying, “Synthesis of hexagonally packed mesoporous TiO<sub>2</sub> by a modified Sol–Gel method,” *Angew. Chemie Int. Ed. English*, vol. 34, pp. 2014–2017, 1995.
- [14] P. Behrens, “Voids in variable chemical surroundings: Mesoporous metal oxides,” *Angew. Chemie (International Ed. English)*, vol. 35, pp. 515–518, 1996.
- [15] Z. R. Tian, W. Tong, J. Y. Wang, N. G. Duan, V. V. Krishnan, and S. L. Suib, “Manganese oxide mesoporous structures: Mixed-valent semiconducting catalysts,” *Science (80-. )*, 1997.
- [16] P. Yang, D. Zhao, D. I. Margolese, B. F. Chmelka, and G. D. Stucky, “Generalized syntheses of large-pore mesoporous metal oxides with semicrystalline frameworks,” *Nature*, vol. 396, pp. 152–155, 1998.
- [17] K. Zhu, K. Egeblad, and C. H. Christensen, “Mesoporous carbon prepared from carbohydrate as hard template for hierarchical zeolites,” *Eur. J. Inorg. Chem.*, pp. 3955–3960, 2007.
- [18] H. Kim and J. Cho, “Hard templating synthesis of mesoporous and nanowire SnO<sub>2</sub> lithium battery anode materials,” *J. Mater. Chem.*, vol. 18, pp. 771–775, 2008.
- [19] Z. Zhang, F. Zuo, and P. Feng, “Hard template synthesis of crystalline mesoporous anatase TiO<sub>2</sub> for photocatalytic hydrogen evolution,” *J. Mater. Chem.*, vol. 20, pp. 2206–2212, 2010.
- [20] R. Ryoo, S. H. Joo, and S. Jun, “Synthesis of highly ordered carbon molecular sieves via template-mediated structural transformation,” *J. Phys. Chem. B*, vol. 103, pp. 7743–7746, 1999.
- [21] K. Zhu, B. Yue, W. Zhou, and H. He, “Preparation of three-dimensional chromium oxide porous single crystals templated by SBA-15,” *Chem. Commun.*, pp. 98–99, 2003.

- [22] W. Shen, X. Dong, Y. Zhu, H. Chen, and J. Shi, "Mesoporous CeO<sub>2</sub> and CuO-loaded mesoporous CeO<sub>2</sub>: Synthesis, characterization, and CO catalytic oxidation property," *Microporous Mesoporous Mater.*, vol. 85, pp. 157–162, 2005.
- [23] F. Jiao, K. M. Shaju, and P. G. Bruce, "Synthesis of nanowire and mesoporous low-temperature LiCoO<sub>2</sub> by a post-templating reaction," *Angew. Chemie - Int. Ed.*, vol. 44, pp. 6550–6553, 2005.
- [24] J. S. Beck *et al.*, "A new family of mesoporous molecular sieves prepared with liquid crystal templates," *J. Am. Chem. Soc.*, vol. 114, pp. 10834–10843, 1992.
- [25] T. Kijima *et al.*, "Noble-metal nanotubes (Pt, Pd, Ag) from lyotropic mixed-surfactant liquid-crystal templates," *Angew. Chemie - Int. Ed.*, vol. 43, pp. 228–232, 2003.
- [26] C. J. Brinker, Y. Lu, A. Sellinger, and H. Fan, "Evaporation-induced self-assembly: Nanostructures made easy," *Adv. Mater.*, vol. 11, pp. 579–585, 1999.
- [27] D. Grosso *et al.*, "Fundamentals of mesostructuring through evaporation-induced self-assembly," *Adv. Funct. Mater.*, vol. 14, pp. 309–322, 2004.
- [28] J. Fan, S. W. Boettcher, C. K. Tsung, Q. Shi, M. Schierhorn, and G. D. Stucky, "Field-directed and confined molecular assembly of mesostructured materials: Basic principles and new opportunities," *Chem. Mater.*, vol. 20, pp. 909–921, 2008.
- [29] K. Liu, M. Zhang, K. Shi, and H. Fu, "Large-pore mesoporous nanocrystalline titania thin films synthesized through evaporation-induced self-assembly," *Mater. Lett.*, vol. 59, pp. 3308–3310, 2005.
- [30] T. Brezesinski, M. Antonietti, M. Groenewolt, N. Pinna, and B. Smarsly, "The generation of mesostructured crystalline CeO<sub>2</sub>, ZrO<sub>2</sub> and CeO<sub>2</sub>-ZrO<sub>2</sub> films using evaporation-induced self-assembly," *New J. Chem.*, vol. 29, pp. 237–242, 2005.
- [31] T. Brezesinski *et al.*, "The generation of mesoporous CeO<sub>2</sub> with crystalline pore walls using novel block copolymer templates," *Stud. Surf. Sci. Catal.*, vol. 156, pp. 243–248, 2005.
- [32] C. Karakaya, Y. Türker, C. Albayrak, and Ö. Dag, "Assembly of molten transition metal salt-surfactant in a confined space for the synthesis of

- mesoporous metal oxide-rich metal oxide-silica thin films,” *Chem. Mater.*, vol. 23, pp. 3062–3071, 2011.
- [33] C. Avci *et al.*, “Molten salt assisted self assembly (MASA): Synthesis of mesoporous metal titanate (CoTiO<sub>3</sub>, MnTiO<sub>3</sub>, and Li<sub>4</sub>Ti<sub>5</sub>O<sub>12</sub>) thin films and monoliths,” *Chem. Mater.*, vol. 26, pp. 6050–6057, 2014.
- [34] F. M. Balci *et al.*, “Synthesis of mesoporous LiMn<sub>2</sub>O<sub>4</sub> and LiMn<sub>(2-x)</sub>Co<sub>(x)</sub>O<sub>4</sub> thin films using the MASA approach as efficient water oxidation electrocatalysts,” *J. Mater. Chem. A*, vol. 6, pp. 13925–13933, 2018.
- [35] C. Karakaya, Y. Türker, and Ö. Dag, “Molten-salt-assisted self-assembly (MASA)-synthesis of mesoporous metal titanate-titania, metal sulfide-titania, and metal selenide-titania thin films,” *Adv. Funct. Mater.*, vol. 23, pp. 4002–4010, 2013.
- [36] D. Andrienko, “Introduction to liquid crystals,” *J. Mol. Liq.*, vol. 267, pp. 520–541, 2018.
- [37] G. Vertogen and W. H. de Jeu, *Thermotropic liquid crystals, fundamentals*, 1st ed. 1988.
- [38] G. J. T. Tiddy, “Surfactant-water liquid crystal phases,” *Phys. Rep.*, vol. 57, pp. 1–46, 1980.
- [39] Ö. Çelik and Ö. Dag, “A new lyotropic liquid crystalline system: Oligo(ethylene oxide) surfactants with [M(H<sub>2</sub>O)<sub>n</sub>]<sub>m</sub> transition metal complexes,” *Angew. Chemie Int. Ed.*, vol. 40, pp. 3799–3803, 2001.
- [40] P. Alexandridis, U. Olsson, and B. Lindman, “Structural polymorphism of amphiphilic copolymers: Six lyotropic liquid crystalline and two solution phases in a poly(oxybutylene)- b -poly(oxyethylene)-water-xylene system,” *Langmuir*, vol. 13, pp. 23–24, 1997.
- [41] P. Alexandridis, U. Olsson, and B. Lindman, “A record nine different phases (four cubic, two hexagonal, and one lamellar lyotropic liquid crystalline and two micellar solutions) in a ternary isothermal system of an amphiphilic block copolymer and selective solvents (water and oil),” *Langmuir*, vol. 14, pp. 2627–2638, 1998.
- [42] P. Alexandridis, D. Zhou, and A. Khan, “Lyotropic liquid crystallinity in amphiphilic block copolymers: Temperature effects on phase behavior and

- structure for poly(ethylene oxide)- b -poly(propylene oxide)- b -poly(ethylene oxide) copolymers of different composition,” *Langmuir*, vol. 12, pp. 2690–2700, 1996.
- [43] Ö. Dag, S. Alayoğlu, and I. Uysal, “Effects of ions on the liquid crystalline mesophase of transition-metal salt: Surfactant (CnEOm),” *J. Phys. Chem. B*, vol. 108, pp. 8439–8446, 2004.
- [44] A. Faik Demirörs, B. E. Eser, and Ö. Dag, “Liquid crystalline mesophases of pluronics (L64, P65, and P123) and transition metal nitrate salts ([M(H<sub>2</sub>O)<sub>6</sub>](NO<sub>3</sub>)<sub>2</sub>),” *Langmuir*, pp. 4156–4162, 21AD.
- [45] C. Albayrak, A. M. Soylu, and Ö. Dag, “Lyotropic liquid crystalline mesophases of [Zn(H<sub>2</sub>O)<sub>6</sub>](NO<sub>3</sub>)<sub>2</sub>-C<sub>12</sub>EO<sub>10</sub>-CTAB-H<sub>2</sub>O and [Zn(H<sub>2</sub>O)<sub>6</sub>](NO<sub>3</sub>)<sub>2</sub>-C<sub>12</sub>EO<sub>10</sub>-SDS-H<sub>2</sub>O systems,” *Langmuir*, vol. 24, pp. 10592–10595, 2008.
- [46] C. Albayrak, A. Cihaner, and Ö. Dag, “A new, highly conductive, lithium salt/nonionic surfactant, lyotropic liquid-crystalline mesophase and its application,” *Chem. - A Eur. J.*, vol. 18, pp. 4190–4194, 2012.
- [47] Y. F. Nicolau, “Solution deposition of thin solid compound films by a successive ionic-layer adsorption and reaction process,” *Appl. Surf. Sci.*, vol. 22–23, pp. 1061–1074, 1985.
- [48] Y. F. Nicolau and J. C. Menard, “Solution growth of ZnS, CdS and Zn(1-x)Cd(x)S thin films by the successive ionic-layer adsorption and reaction process; growth mechanism,” *J. Cryst. Growth*, vol. 92, pp. 128–142, 1988.
- [49] Y. F. Nicolau, M. Brunel, and M. Dupuy, “ZnS, CdS, and Zn(1-x)Cd(x)S thin films deposited by the successive ionic layer adsorption and reaction process,” *J. Electrochem. Soc.*, vol. 137, pp. 2915–2924, 1990.
- [50] P. K. Nair and A. E. Jimenez, “Photosensitive ZnO thin films prepared by the chemical depositiox method SILAR,” *Semicond. Sci. Technol.*, vol. 10, pp. 1277–1281, 1995.
- [51] X. D. Gao, X. M. Li, and W. D. Yu, “Synthesis and optical properties of ZnO nanocluster porous films deposited by modified SILAR method,” *Appl. Surf. Sci.*, vol. 229, pp. 275–281, 2004.
- [52] K. Mageshwari and R. Sathyamoorthy, “Physical properties of nanocrystalline

- CuO thin films prepared by the SILAR method,” *Mater. Sci. Semicond. Process.*, vol. 16, pp. 337–343, 2013.
- [53] S. D. Sartale and C. D. Lokhande, “Preparation and characterization of nickel sulphide thin films using successive ionic layer adsorption and reaction (SILAR) method,” *Mater. Chem. Phys.*, vol. 72, pp. 101–104, 2001.
- [54] S. S. Mali, P. S. Shinde, C. A. Betty, P. N. Bhosale, Y. W. Oh, and P. S. Patil, “Synthesis and characterization of Cu<sub>2</sub>ZnSnS<sub>4</sub> thin films by SILAR method,” *J. Phys. Chem. Solids*, vol. 73, pp. 735–740, 2012.
- [55] B. Ghosh, M. Das, P. Banerjee, and S. Das, “Fabrication and optical properties of SnS thin films by SILAR method,” *Appl. Surf. Sci.*, vol. 254, pp. 6436–6440, 2008.
- [56] Y. Ren, Z. Ma, and P. G. Bruce, “Ordered mesoporous metal oxides: Synthesis and applications,” *Chem. Soc. Rev.*, vol. 41, pp. 4909–4927, 2012.
- [57] B. O’Regan and M. Grätzel, “A low-cost, high-efficiency solar cell based on dye-sensitized colloidal TiO<sub>2</sub> films,” *Nature*, vol. 353, pp. 737–740, 1991.
- [58] A. Corma, P. Atienzar, H. García, and J. Y. Chane-Ching, “Hierarchically mesostructured doped CeO<sub>2</sub> with potential for solar-cell use,” *Nat. Mater.*, vol. 3, pp. 394–397, 2004.
- [59] C. Li *et al.*, “Cathode materials modified by surface coating for lithium ion batteries,” *Electrochim. Acta*, vol. 51, pp. 3872–3883, 2006.
- [60] J. R. Dahn, U. von Sacken, M. W. Juskow, and H. Al-Janaby, “Rechargeable LiNiO<sub>2</sub>/carbon cells,” *J. Electrochem. Soc.*, vol. 138, pp. 2207–2211, 1991.
- [61] K. M. Shaju, F. Jiao, A. Débart, and P. G. Bruce, “Mesoporous and nanowire Co<sub>3</sub>O<sub>4</sub> as negative electrodes for rechargeable lithium batteries,” *Phys. Chem. Chem. Phys.*, vol. 9, pp. 1837–1842, 2007.
- [62] F. Jiao, J. Bao, and P. G. Bruce, “Factors influencing the rate of Fe<sub>2</sub>O<sub>3</sub> conversion reaction,” *Electrochem. Solid-State Lett.*, vol. 10, pp. 264–266, 2007.
- [63] F. Jiao, J. Bao, A. H. Hill, and P. G. Bruce, “Synthesis of ordered mesoporous Li-Mn-O spinel as a positive electrode for rechargeable lithium batteries,” *Angew. Chemie - Int. Ed.*, vol. 47, pp. 9711–9716, 2008.
- [64] M. Vettraiño, M. Trudeau, and D. M. Antonelli, “Synthesis and characterization

- of a new family of electroactive alkali metal doped mesoporous Nb, Ta, and Ti oxides and evidence for an Anderson transition in reduced mesoporous titanium oxide,” *Inorg. Chem.*, vol. 40, pp. 2088–2095, 2001.
- [65] P. A. Nelson and J. R. Owen, “A high-performance supercapacitor/battery hybrid incorporating templated mesoporous electrodes,” *J. Electrochem. Soc.*, vol. 150, pp. 1313–1317, 2003.
- [66] J. N. Kondo and K. Domen, “Crystallization of mesoporous metal oxides,” *Chem. Mater.*, vol. 20, pp. 835–847, 2007.
- [67] Y. Noda, B. Lee, K. Domen, and J. N. Kondo, “Synthesis of crystallized mesoporous tantalum oxide and its photocatalytic activity for overall water splitting under ultraviolet light irradiation,” *Chem. Mater.*, vol. 20, pp. 5361–5367, 2008.
- [68] Y. Ren, Z. Ma, L. Qian, S. Dai, H. He, and P. G. Bruce, “Ordered crystalline mesoporous oxides as catalysts for CO oxidation,” *Catal. Letters*, vol. 131, pp. 146–154, 2009.
- [69] H. Tüysüz, M. Comotti, and F. Schüth, “Ordered mesoporous Co<sub>3</sub>O<sub>4</sub> as highly active catalyst for low temperature CO-oxidation,” *Chem. Commun.*, pp. 4022–4024, 2008.
- [70] B. M. Hunter, H. B. Gray, and A. M. Müller, “Earth-abundant heterogeneous water oxidation catalysts,” *Chem. Rev.*, vol. 116, pp. 14120–14136, 2016.
- [71] M. Gong *et al.*, “An advanced Ni-Fe layered double hydroxide electrocatalyst for water oxidation,” *J. Am. Chem. Soc.*, vol. 135, pp. 8452–8455, 2013.
- [72] M. W. Kanan and D. G. Nocera, “In situ formation of an oxygen-evolving catalyst in neutral water containing phosphate and Co<sup>2+</sup>,” *Science (80-. )*, vol. 321, pp. 1072–1075, 2008.
- [73] C. Iwakura, K. Hirao, and H. Tamura, “Preparation of ruthenium dioxide electrodes and their anodic polarization characteristics in acidic solutions,” *Electrochim. Acta*, vol. 22, pp. 335–340, 1977.
- [74] R. L. Doyle, I. J. Godwin, M. P. Brandon, and M. E. G. Lyons, “Redox and electrochemical water splitting catalytic properties of hydrated metal oxide modified electrodes,” *Phys. Chem. Chem. Phys.*, vol. 15, pp. 13737–13783, 2013.

- [75] G. Lodi, E. Sivieri, A. De Battisti, and S. Trasatti, "Ruthenium dioxide-based film electrodes," *J. Appl. Electrochem.*, vol. 8, pp. 135–143, 1978.
- [76] D. Galizzioli, F. Tantardini, and S. Trasatti, "Ruthenium dioxide: A new electrode material. I. Behaviour in acid solutions of inert electrolytes," *J. Appl. Electrochem.*, vol. 4, pp. 57–67, 1974.
- [77] D. Galizzioli, F. Tantardini, and S. Trasatti, "Ruthenium dioxide: A new electrode material. II. Non-stoichiometry and energetics of electrode reactions in acid solutions," *J. Appl. Electrochem.*, vol. 5, pp. 203–214, 1975.
- [78] N. T. Suen, S. F. Hung, Q. Quan, N. Zhang, Y. J. Xu, and H. M. Chen, "Electrocatalysis for the oxygen evolution reaction: Recent development and future perspectives," *Chem. Soc. Rev.*, vol. 46, pp. 337–365, 2017.
- [79] R. Kötz and S. Stucki, "Stabilization of RuO<sub>2</sub> by IrO<sub>2</sub> for anodic oxygen evolution in acid media," *Electrochim. Acta*, vol. 31, pp. 1311–1316, 1986.
- [80] Y. Matsumoto, "New types of anodes for the oxygen evolution reaction in acidic solution," *J. Electrochem. Soc.*, vol. 133, pp. 2257–2262, 1986.
- [81] J. Mohammed-Ibrahim and S. Xiaoming, "Recent progress on earth abundant electrocatalysts for hydrogen evolution reaction (HER) in alkaline medium to achieve efficient water splitting – A review," *J. Energy Chem.*, vol. 400, pp. 31–68, 2018.
- [82] D. Chandra, N. Abe, D. Takama, K. Saito, T. Yui, and M. Yagi, "Open pore architecture of an ordered mesoporous IrO<sub>2</sub> thin film for highly efficient electrocatalytic water oxidation," *ChemSusChem*, vol. 8, pp. 795–799, 2015.
- [83] J. Kibsgaard, T. R. Hellstern, S. J. Choi, B. N. Reinecke, and T. F. Jaramillo, "Mesoporous ruthenium/ruthenium oxide thin films: Active electrocatalysts for the oxygen evolution reaction," *ChemElectroChem*, vol. 4, pp. 2480–2485, 2017.
- [84] M. Humphries, *Rare Earth Elements: The Global Supply Chain*. 2010.
- [85] A. Fujishima and K. Honda, "Electrochemical photolysis of water at a semiconductor electrode," *Nature*, vol. 238, pp. 37–38, 1972.
- [86] M. Morita, C. Iwakura, and H. Tamura, "The anodic characteristics of manganese dioxide electrodes prepared by thermal decomposition of manganese nitrate," *Electrochim. Acta*, vol. 22, pp. 325–328, 1977.

- [87] A. Harriman, I. J. Pickering, J. M. Thomas, and P. A. Christensen, "Metal oxides as heterogeneous catalysts for oxygen evolution under photochemical conditions," *J. Chem. Soc. Faraday Trans. 1 Phys. Chem. Condens. Phases*, vol. 84, pp. 2795–2806, 1988.
- [88] F. Jiao and H. Frei, "Nanostructured manganese oxide clusters supported on mesoporous silica as efficient oxygen-evolving catalysts," *Chem. Commun.*, vol. 46, pp. 2920–2922, 2010.
- [89] Y. Gorlin and T. F. Jaramillo, "A bifunctional nonprecious metal catalyst for oxygen reduction and water oxidation," *J. Am. Chem. Soc.*, vol. 132, pp. 13612–13614, 2010.
- [90] J. E. Turner, "The characterization of doped iron oxide electrodes for the photodissociation of water," *J. Electrochem. Soc.*, vol. 131, pp. 1777–1783, 1986.
- [91] C. P. Berlinguette *et al.*, "Photochemical route for accessing amorphous metal oxide materials for water oxidation catalysis," *Science (80-. )*, vol. 340, pp. 60–63, 2013.
- [92] I. Cesar, A. Kay, J. A. G. Martinez, and M. Grätzel, "Translucent thin film Fe<sub>2</sub>O<sub>3</sub> photoanodes for efficient water splitting by sunlight: Nanostructure-directing effect of Si-doping," *J. Am. Chem. Soc.*, vol. 128, pp. 4582–4583, 2006.
- [93] C. Iwakura, A. Honji, and H. Tamura, "The anodic evolution of oxygen on Co<sub>3</sub>O<sub>4</sub> film electrodes in alkaline solutions," *Electrochim. Acta*, vol. 26, pp. 1319–1326, 1981.
- [94] P. Rasiyah and A. C. C. Tseung, "A Mechanistic study of oxygen evolution on NiCo<sub>2</sub>O<sub>4</sub>. II. Electrochemical kinetics," *J. Electrochem. Soc.*, vol. 130, pp. 2384–2386, 1983.
- [95] R. N. Singh, M. Hamdani, J. F. Koenig, G. Poillerat, J. L. Gautier, and P. Chartier, "Thin films of Co<sub>3</sub>O<sub>4</sub> and NiCo<sub>2</sub>O<sub>4</sub> obtained by the method of chemical spray pyrolysis for electrocatalysis III. The electrocatalysis of oxygen evolution," *J. Appl. Electrochem.*, vol. 20, pp. 442–446, 1990.
- [96] L. M. Da Silva, J. F. C. Boodts, and L. A. De Faria, "Oxygen evolution at RuO<sub>2</sub>(x)+Co<sub>3</sub>O<sub>4</sub>(1-x) electrodes from acid solution," *Electrochim. Acta*, vol.

- 46, pp. 1369–1375, 2001.
- [97] H. Tüysüz, Y. J. Hwang, S. B. Khan, A. M. Asiri, and P. Yang, “Mesoporous Co<sub>3</sub>O<sub>4</sub> as an electrocatalyst for water oxidation,” *Nano Res.*, vol. 6, pp. 47–54, 2013.
- [98] H. Bode, K. Dehmelt, and J. Witte, “Zur kenntnis der nickelhydroxidelektrode. II. Über die oxydationsprodukte von nickel(II)-hydroxiden,” *ZAAC - J. Inorg. Gen. Chem.*, vol. 366, pp. 1–21, 1969.
- [99] G. Młynarek, M. Paszkiewicz, and A. Radniecka, “The effect of ferric ions on the behaviour of a nickelous hydroxide electrode,” *J. Appl. Electrochem.*, vol. 14, pp. 145–149, 1984.
- [100] D. A. Corrigan, “Catalysis of the oxygen evolution reaction by iron impurities in thin film nickel oxide electrodes,” *J. Electrochem. Soc.*, vol. 134, pp. 377–384, 1987.
- [101] Y. Zhao *et al.*, “Ultrafine NiO nanosheets stabilized by TiO<sub>2</sub> from monolayer NiTi-LDH precursors: An active water oxidation electrocatalyst,” *J. Am. Chem. Soc.*, vol. 138, pp. 6517–6524, 2016.
- [102] X. Yu *et al.*, “Multi-walled carbon nanotubes supported porous nickel oxide as noble metal-free electrocatalysts for efficient water oxidation,” *Int. J. Hydrogen Energy*, vol. 39, pp. 10467–10475, 2014.
- [103] G. Liu, X. Gao, K. Wang, D. He, and J. Li, “Uniformly mesoporous NiO/NiFe<sub>2</sub>O<sub>4</sub> biphasic nanorods as efficient oxygen evolving catalyst for water splitting,” *Int. J. Hydrogen Energy*, vol. 41, pp. 17976–17986, 2016.
- [104] C. W. Cady *et al.*, “Tuning the electrocatalytic water oxidation properties of AB<sub>2</sub>O<sub>4</sub> spinel nanocrystals: A (Li, Mg, Zn) and B (Mn, Co) site variants of LiMn<sub>2</sub>O<sub>4</sub>,” *ACS Catal.*, vol. 5, pp. 3403–3410, 2015.
- [105] J. Wang, L. Li, H. Tian, Y. Zhang, X. Che, and G. Li, “Ultrathin LiCoO<sub>2</sub> nanosheets: An efficient water-oxidation catalyst,” *ACS Appl. Mater. Interfaces*, vol. 9, pp. 7100–7107, 2017.
- [106] G. Saat, F. M. Balci, E. P. Alsaç, F. Karadas, and Ö. Dag, “Molten salt assisted self-assembly: Synthesis of mesoporous LiCoO<sub>2</sub> and LiMn<sub>2</sub>O<sub>4</sub> thin films and investigation of electrocatalytic water oxidation performance of lithium cobaltate,” *Small*, vol. 14, p. 1701913, 2018.

- [107] A. J. Bard and L. R. Faulkner, *Electrochemical methods: Fundamentals and applications*, 2nd ed. 2001.
- [108] N. Elgrishi, K. J. Rountree, B. D. McCarthy, E. S. Rountree, T. T. Eisenhart, and J. L. Dempsey, “A practical beginner’s guide to cyclic voltammetry,” *J. Chem. Educ.*, vol. 95, pp. 197–206, 2018.
- [109] P. Kissinger and W. Heineman, “Cyclic voltammetry,” *J. Chem. Educ.*, vol. 60, p. 702, 1983.
- [110] P. Zanello, *Inorganic electrochemistry: Theory, practice and applications*. 2003.
- [111] E. E. Kalu, T. T. Nwoga, V. Srinivasan, and J. W. Weidner, “Cyclic voltammetric studies of the effects of time and temperature on the capacitance of electrochemically deposited nickel hydroxide,” *J. Power Sources*, vol. 92, pp. 163–167, 2001.
- [112] H. Wang and L. Pilon, “Physical interpretation of cyclic voltammetry for measuring electric double layer capacitances,” *Electrochim. Acta*, vol. 64, pp. 130–139, 2012.
- [113] O. A. Petrii, R. R. Nazmutdinov, M. D. Bronshtein, and G. A. Tsirlina, “Life of the Tafel equation: Current understanding and prospects for the second century,” *Electrochim. Acta*, vol. 52, pp. 3493–3504, 2007.
- [114] T. Shinagawa, A. T. Garcia-Esparza, and K. Takanabe, “Insight on Tafel slopes from a microkinetic analysis of aqueous electrocatalysis for energy conversion,” *Sci. Rep.*, vol. 5, p. 13801, 2015.
- [115] K. Kodama, R. Jinnouchi, T. Suzuki, T. Hatanaka, and Y. Morimoto, “Extraordinarily small Tafel slope for oxide formation reaction on Pt (1 1 1) surface,” *Electrochim. Acta*, vol. 78, pp. 592–596, 2012.
- [116] T. Takashima, K. Hashimoto, and R. Nakamura, “Mechanisms of pH-dependent activity for water oxidation to molecular oxygen by MnO<sub>2</sub> electrocatalysts,” *J. Am. Chem. Soc.*, vol. 134, pp. 1519–1527, 2012.
- [117] J. B. Gerken *et al.*, “Electrochemical water oxidation with cobalt-based electrocatalysts from pH 0–14: The thermodynamic basis for catalyst structure, stability, and activity,” *J. Am. Chem. Soc.*, vol. 133, pp. 14431–14442, 2011.
- [118] T. Nakazono, A. R. Parent, and K. Sakai, “Cobalt porphyrins as homogeneous

- catalysts for water oxidation,” *Chem. Commun.*, vol. 49, pp. 6325–6327, 2013.
- [119] M. C. Biesinger, B. P. Payne, A. P. Grosvenor, L. W. M. Lau, A. R. Gerson, and R. S. C. Smart, “Resolving surface chemical states in XPS analysis of first row transition metals, oxides and hydroxides: Cr, Mn, Fe, Co and Ni,” *Appl. Surf. Sci.*, vol. 257, pp. 2717–2730, 2011.
- [120] A. J. Esswein, M. J. Mcmurdo, P. N. Ross, A. T. Bell, and T. D. Tilley, “Size-dependent activity of Co<sub>3</sub>O<sub>4</sub> nanoparticle anodes for alkaline water electrolysis,” *J. Phys. Chem. C*, vol. 113, pp. 15068–15072, 2009.
- [121] S. Yeo, R. S. Orehotsky, J. Visscher, W. Srinivasan, “Ruthenium-based mixed oxides as electrocatalysts for oxygen evolution in acid electrolytes,” *J. Electrochem. Soc.*, vol. 128, p. 1900, 1981.